GRADUATION PROJECT
60 ECTS
within
Applied Physics - Plasma track (3MA60)
Science and Technology of Nuclear Fusion (3NFA60)

Investigating the Composition of Tin Vapor

D.J. Engels
0957841

This thesis is confidential until 08-07-2023
and
is in accordance with the Code of Scientific Integrity of the Eindhoven University of Technology

Graded by:

For Applied Physics:

prof.dr. N.J. Lopes Cardozo
dr.ir. J. van Dijk
dr. T.W. Morgan
dr. O.O Versolato

For Nuclear Fusion:

prof.dr. R.J.E. Jaspers
prof.dr. N.J. Lopes Cardozo
dr. G. Finotello
dr. R.A. Meijer

Supervised by:

prof.dr. N.J. Lopes Cardozo
Science and Technology of Nuclear Fusion
Department of Applied Physics
Eindhoven University of Technology
The Netherlands

dr. O.O. Versolato &
dr. R.A. Meijer
EUV Plasma Processes
Advanced Research Center for Nanolithography
The Netherlands

24/6/2022

This page has intentionally been left blank.

Contents

Abstract

Tin vapor is used in the EUV source of lithography machines and the liquid-tin divertor of fusion devices. However, in both cases, this tin vapor's composition is unknown, whether it be atoms, clusters of atoms, or (a size distribution of) nanodroplets. Measuring and understanding the composition of the tin vapor would allow for future improvements in both these fields. For EUV lithography, it could help in the quest for a more efficient EUV generation method. It could also help to create a more reliable heat exhaust in the field of fusion. Thus, in this thesis, the following question will be answered: "What is the composition of tin vapor targets used in the EUV light creation process, and which factors influence this composition?"

An existing experimental setup is improved with multi-wavelength absorption imaging in the UV range, *UV shadowgraphy*. A model is created to predict and explain experimentally measured spectra. This model incorporates atomic absorption and Mie scattering on nanodroplets. Code is written to automate the measurements and find the extinction from the captured images.

Detailed extinction spectra between 225 to 405 nm are presented. These spectra show a background extinction level caused by Mie scattering, with narrow peaks in extinction on top. These narrow peaks are atomic resonances. One such spectrum is matched to the model to find its density, atomic mass ratio, temperature, and nanodroplet size. The model matches the general trend in the experimental data. However, there are some aspects where the model differs from the data. The substantial decrease in the background extinction as the wavelength becomes longer, caused by Mie scattering, and the width and strength of the atomic resonances cannot be matched perfectly by the model. The mismatch in the resonances is expected to be caused by unmodeled density-related broadening effects. Further research into the refractive index is proposed to match the decay in the extinction due to Mie scattering. The influence of some parameters, such as spatial position and timing, on the observed spectra are also presented. All spectra show similar profiles.

To conclude, the novel *UV shadowgraphy* metrology has been implemented with success. The research question has been partly answered using this metrology by proving the presence of atoms and nanodroplets in tin vapor for the first time. Future work to find the cause of the model mismatch is proposed to allow for the final determination of the composition of tin vapor.

This page has intentionally been left blank.

1 Introduction

To someone living in the 21st century, 100 years sounds like a very long time. One hundred years ago, the world was recovering from the 'Great War,' the telephone was a novelty, and refrigeration had not been invented yet. Just 100 years later, people would look weird at you if you have a *wired* telephone. The rate of technological advancement in the modern world is just astonishing. Even though we have grown accustomed to it, it was not always like this. For someone living in medieval Europe of the eighth century, not much would have changed in 100 years. Most readers probably cannot name a single invention from the eighth century. Again, nowadays, technology improving year-on-year is a commonly known fact. We have even started using scaling laws that pose that some technology will improve or double every few years. Most readers can name at least one such scaling law.

For example, the deployment of renewable energy sources, such as photovoltaics or nuclear fusion, follows scaling laws. Photovoltaics are still growing exponentially, while nuclear fusion has failed to follow this trend in recent years.[1,2] This shows that following scaling laws does not come automatically; it requires hard work. Moore's law is probably the most famous example of a scaling law for technology; computers in this case. Stated initially in 1965 and revised in 1975, Gordon Moore, founder of Intel, stated that the number of transistors on a microchip would double every two years.[3] Moore's law has been in place for over 50 years and still holds to this day.[4]

In short, scaling laws are everywhere around us in the modern world, from energy sources to computers and industrial processes; their impact cannot be understated. To express this is in a simple experiment: Ask someone younger than ten what the 'save' icon is based upon; they will probably not know. That is how fast computers are progressing.

1.1 Lithography

The challenge of keeping up with Moore's law is immense, as the transistors have to keep shrinking year-by-year to allow for the continued doubling of Moore's law. A lot of technological development goes into shrinking the transistors. An essential process here is photolithography, a photochemical process.[6] In this process, a coated silicon wafer covered with photoresist is exposed to light through a mask with a specific structure. This structure corresponds to the design of a semiconductor chip.[7] In other steps, the photoresist is etched, bombarded with ions, and more before the cycle starts again to create another layer of the chip.[8] The full cycle can be seen in Fig. 1. Of these steps, photolithography is critical as it determines the size of the nanoscale structure, the transistor in this case.[9]

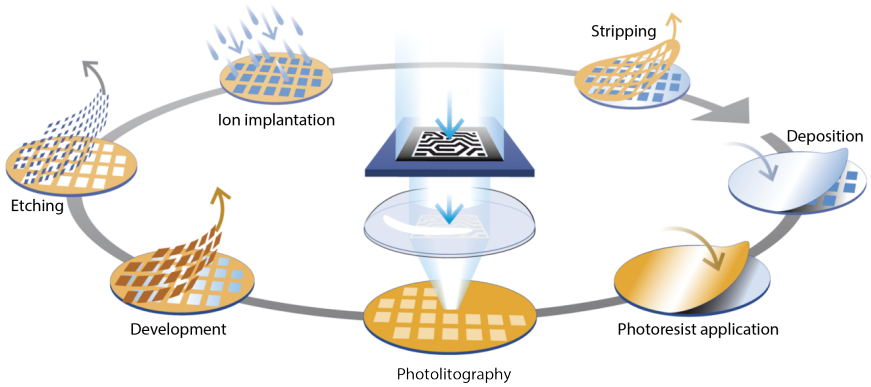

Figure 1: The different steps to create one layer of a microchip. Obtained from [5].

The Critical Dimension (CD) is the smallest feature size that can be printed using photolithography. It can be written as

$$\mathrm{CD} = k_1 \frac{\lambda}{\mathrm{NA}}, \tag{1}$$

where k_1 is a parameter, typically between 0.3 and 0.4, λ is the wavelength, and NA is the numerical aperture. The k_1 parameter encapsulates all process-related factors that can be done to optimize CD.

Lithography with Extreme Ultraviolet (EUV) light is the current pinnacle of technology, enabling the smallest possible transistors. A step from 193 nm light to 13.5 nm EUV light was taken, allowing the transistors to become even smaller for even faster computing.[10]

Creating EUV light is not an easy task. In current lithography machines, EUV light is created by shooting a tin droplet with a series of laser pulses. The final laser pulse generates a plasma with temperatures of roughly 30 eV. This temperature is required to produce the highly charged Sn^{8+} to Sn^{14+} tin ions that generate the EUV light around 13.5 nm.[11] A view into a modern EUV light generation module can be seen in Fig. 2.

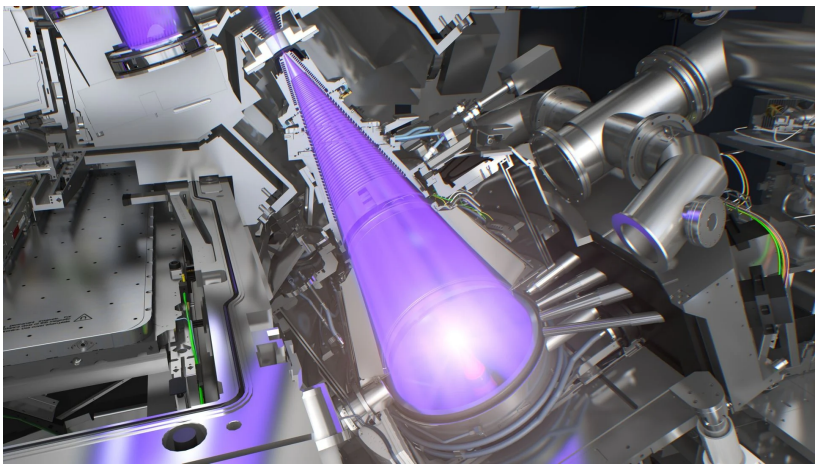

Figure 2: The inside of a EUV light generation module. This is during the final stage where the light is generated and collected to be put to use. Image courtesy of ASML.

The mass distribution of tin that the final pulse interacts with is called the *target*. Without any additional laser pulses, this would be a droplet. However, the additional laser pulses allow this to be different shapes. This process, making a different shape for the final pulse to interact with, is called *target shaping*. Extensive research has been done on creating the optimal target, where two aspects are essential: conversion efficiency (CE), which is the amount of usable EUV light generated for a specific input laser energy, and debris mitigation, as it is vital to ensure that the tin does not fly everywhere in the machine. It has been found that pre-deforming the droplets using a pre-pulse is desired. Extensive research has been done on different types of pre-pulse. Generally, the focus has been on *short* pulses (femto- or picoseconds)[12–19] or *long* pulses (nanoseconds).[18,20–23] Short pulses cause an expanding cavity in the droplet, resulting in a dome-like structure, while long pulses deform the droplet into a thin curved sheet with a thickness of several tens of nanometers. Both methods are used in industry; however, the long pre-pulse will be used throughout this thesis.

As mentioned, the long pre-pulse has been studied in detail. The droplet is propelled in the laser's direction when hit with a long pre-pulse. It also starts to expand radially into a sheet. The propulsion velocity of the sheet has been found to depend only on the laser energy deposited on the droplet,[18,22] while there are two critical parameters for the radial expansion of the sheet. The

first is the capillary time, the characteristic time scale for droplet expansion and retraction. The second is the Weber number, a dimensionless number that measures the relative importance of a droplet's kinetic energy compared to its initial surface energy. Together, these determine how the droplet expands and eventually retracts again.[22] The partition of the laser energy into the propulsion and expansion depends mainly on the ratio between the droplet size and laser beam size but it also exhibits a minor laser energy dependence.[23,24] Typical propulsion and expansion speeds are in the order of 100 m/s.[25] The sheet thickness and volume evolution over time have also been investigated.[25,26]

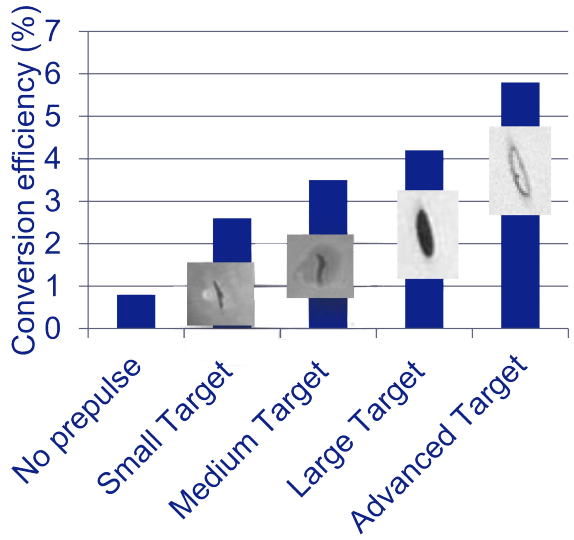

Figure 3: This figure shows how the CE (output EUV light for a specific input laser energy) increased over target shape generations. No target shaping gives the lowest CE, while different target shaping techniques increased CE. Finally, advanced target shaping is proposed as the next step. Example images of the targets are imposed on the bar chart. Obtained from: [27].

Advanced target shaping could be the next step to increase the efficiency of EUV light generation.[27] The concept of advanced target shaping is to add another target preparation step (another pre-pulse) to increase the efficiency of EUV light generation. As can be seen in Fig. 3, such advanced target shaping may bring increased CE.[27] It is not yet known what exact implementation of an *advanced target* should optimally be used in the next generation of lithography machines.

One possibility for advanced target shaping is to create a tin vapor from the tin sheet before creating the EUV light using the main pulse. The concept is that this may create a better target for the interaction with the main pulse, thus increasing the CE. It is possible to vaporize the tin sheets;[25] however, it is currently unknown what the composition of such a created vapor is. Obtaining more information about the vapor composition is essential as many phases can coexist within a vapor. The composition can include atoms fully vaporized in a gaseous state, or it can have clusters of molecules or atoms, from nanometers to micrometers in size. Another option is that ions are created, which will form a plasma when the ion density gets high enough. The exact composition could significantly affect the effectivity of absorbing the main pulse and creating EUV light. For example, the absorption efficiency of the main pulse can differ significantly depending on the phase. In short, a desire exists to measure and understand the composition of the vaporized tin sheet. This knowledge could allow advanced target shaping by vaporization to create a better target for EUV light generation.

1.2 Nuclear Fusion

The vapor in the EUV photolithography machines has a connection to fusion research. Fusion can become the ultimate energy source of humankind as it runs on one of the most abundant things on earth: water.[28] In short, nuclear fusion works by merging two light nuclei, a process that releases a large amount of energy. It is the opposite of nuclear fission, where heavy nuclei are split to release energy. Several combinations of nuclei can be used for fusion; however, deuterium and tritium (two hydrogen isotopes) are the most likely to be used in commercial fusion.[29] Several challenges must be tackled before this becomes a reality. One of these challenges is: how to handle the energy generated in a fusion reactor?[30]

Scientists worldwide are working hard to create the technology suited to the plasma exhaust of a fusion reactor. Even though a large percentage of the energy is carried away by neutrons and thus does not end in the exhaust, creating a plasma exhaust that can withstand the high heat loads of a fusion reactor remains challenging. The *divertor* has been the standard plasma exhaust for decades. A divertor is created by using additional coils, shaping the magnetic field so that all the heat of the *scrape-off-layer* (SOL), the part of the plasma that has left the bulk, is funneled into the divertor area. This divertor area and coils are shaped to ensure that the heat load on the wall is spread out.[31] A visualization of this can be seen in Fig. 4. Even with a divertor setup, where the heat load is spread out, the load can still reach values above $10\,\mathrm{MW/m^2}$. This heat load can increase even more during bursts, known as Edge Localized Modes (ELMs).[32] Such heat loads are not sustainable for the long-term operation of a reactor. This remains a challenge to be solved.

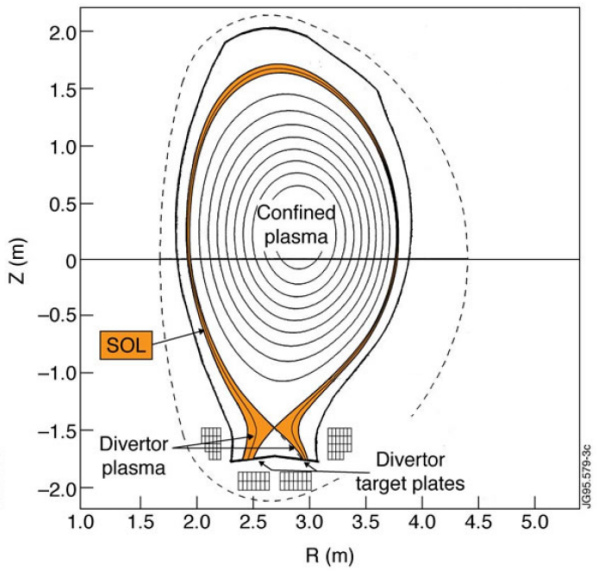

Figure 4: A visualization of a divertor. Note the scrape-off-layer (SOL), which is separated from the bulk of the plasma. The plasma in the SOL is steered into the divertor using additional coils. Image courtesy of EFDA-JET.

One option is using a liquid metal divertor.[33] In a liquid metal divertor, the divertor is covered in a thin layer of liquid metal. One advantage of this is already evident in steady-state operation. The advantage is that the liquid metal layer is self-healing, continuously replacing itself, ensuring that little to no erosion can happen. Another advantage is that it also performs better during pulsed bursts, the ELMs.[34] In that case, the metal will evaporate and form a radiating cloud, absorbing energy from the ELM in the process. As the radiation from the cloud is spread over a larger area, the heat load on the wall during bursts will be lower. Thus, covering the divertor with a thin layer would protect the underlying divertor from the heat pulses.[34] Its self-healing property extends the divertors' lifetime and increases the up-time of the fusion reactor. Liquid tin is considered an option for the liquid metal divertor due to several factors, such as its low melting temperature. It also does not have a too high atomic number (which would make the plasma unstable) nor has issues with tritium retention from the plasma.[35] Extensive research has been done on the liquid-tin divertor concept at TU Eindhoven; a concept design for DEMO has been created,[35] see Fig. 5. However, in the field of liquid-tin divertors, the same questions exist: "What is this tin vapor exactly? What states exist in it and in what ratio?" This question is vital for the same reasons as it is crucial to EUV lithography. The energy that can be absorbed differs between atoms and micro- or nanodroplets. The same is true for the absorption efficiency of the vapor; it can strongly depend on its composition. Additionally, a fusion reactor is also vulnerable to tin reaching the plasma core, as too much of any impurity can quench the reaction. Characterizing the tin vapor can help quantify the liquid-tin divertor's impact on the plasma purity and stability. In short, developing a method to measure the composition may help advance liquid-tin divertor efficiency by increasing understanding of its workings.

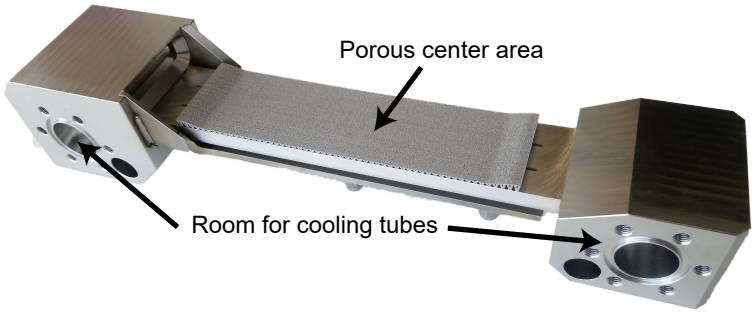

Figure 5: A concept design of a liquid-tin divertor block. The porous center area is where the liquid tin would be present, while the edges have room for cooling tubes. Many of these would be combined for one divertor module. Image courtesy of Jos Scholte of TU Eindhoven.

1.3 Problem statement

In short, the EUV sources for lithography and liquid tin divertors in fusion reactors both deal with tin vapor. However, it is currently unknown what the composition of this vapor exactly is for both these cases. This thesis will focus on EUV light generation, the application that the Advanced Research Center for Nanolithography (ARCNL) studies. In summary, the research question is:

What is the composition of tin vapor targets used in the EUV light creation process, and which factors influence this composition?

This question is part of a larger question in the EUV lithography field: "How to increase the efficiency of the EUV source?"

In more detail, "How to absorb the main pulse efficiently and generate as much EUV light as possible while extending life- and uptime?" The more specific research question is being tackled in this thesis; the larger scope questions are years-long projects for a large corporation. The knowledge gathered in this thesis will contribute to realizing the larger objective by providing a tool to measure the composition and a first guideline in shaping the composition. This tool to measure the composition can also be applied to fusion devices to increase liquid tin divertor knowledge and efficiency.

1.4 Thesis outline

Multiple steps will have to be taken to answer the research question and find the composition of the tin vapor. This section will present these steps and where these steps will be discussed in this thesis.

A setup called *Dalek-II* was already present at ARCNL at the start of this project. Dalek-II had recently been completed, starting operation at the beginning of 2021. Research has been ongoing on 'big brother' *Dalek-I* for several years. This research has contributed to state-of-the-art knowledge about EUV light generation. The existing *shadowgraphy* diagnostic will be extended by implementing *UV shadowgraphy* to tackle the research question at hand. UV shadowgraphy will be multi-wavelength shadowgraphy in the ultraviolet range instead of the fixed wavelength of 560 nm. One can create an absorption spectrum by capturing shadowgram images of the vapor at different wavelengths and tracking how the absorption changes. This absorption spectrum can give information about the composition. At the start of this project, a new laser that can create a wide range of wavelengths had just been set up at Dalek-II, ready to be integrated within the setup. Realizing the implementation of UV shadowgraphy is the first subgoal. It, and the rest of the experimental setup, will be presented in Section 4.

The second subgoal is to create a model to predict and explain the measured absorption spectra. Creating a model to predict these spectra will help running efficient measurements once the setup is completed. It will also give insight into what can be expected. The theory underlying this model and the expected components will be shown in Section 2. The model itself will be presented in Section 3.

A third subgoal is to gather sufficient experimental data using the improved Dalek-II setup. The goal will be to create well-defined targets and create absorption spectra for these targets. Doing this for multiple targets will allow the investigation of the influence of the target parameters on the composition of the tin vapor. The obtained results will be presented in Section 5.

The final subgoal of this thesis will be to match the created model to the experimental results. Matching the model will allow for the extraction of physical properties of the tin vapor, such as its composition and density. Any differences between the model and the data can also be investigated in an effort to fully understand the mechanism that sets the composition of the tin. The result of matching the model will be shown in Section 6. The results and the model will be discussed in Section 7.

A team of three worked on the Dalek-II setup during this graduation project. This team was Randy Meijer (postdoc, daily supervisor), Karl Schubert (1st year Ph.D.), and Dion Engels (the author of this thesis). Most work on the setup was done in cooperation (subgoals 1 & 3). In contrast, all modeling, coding (both capturing and analysis), and analysis work was done by Dion alone (subgoals 2 & 4). It will also be noted which parts of the setup were implemented by the author in the setup section.

Finally, this thesis will end with a conclusion in Section 8.

2 Theory

In this section, the theoretical background needed for this thesis is introduced. Absorption by atoms is described, and Mie theory, applicable to nanodroplets, is treated to find the absorption of the total vapor. Atoms and ions are characterized by a narrow-peaked absorption profile in the spectral domain. This profile depends on several factors, such as the atomic line strength, density, and temperature. In contrast, Mie theory predicts significantly broader profiles, where the nanodroplet size is a crucial parameter. Any contribution by electrons can be discarded as their density is low since no plasma is formed during the vaporization. Clusters of atoms can also cause broad absorption profiles with increasing absorption as the wavelength is shortened.[36–40] They are considered out of scope for the model. This decision will be reflected upon in the discussion.

2.1 Atomic absorption

It will be essential to understand atomic absorption to prepare for the case of atoms or ions being present in the vapor. Atomic absorption of light is described by the Beer-Lambert law, which states the absorption or transmission of light depends on the medium that it is traversing through[41–43]

$$A = \frac{I}{I_0} = 1 - \exp(-n \cdot \sigma \cdot L), \tag{2}$$

where A is the absorption fraction and I and I_0 are the final and initial intensities, respectively ($\mathrm{W/m^2}$). The exponent is determined by the atom density n ($\mathrm{m^{-3}}$), the cross-section σ ($\mathrm{m^2}$), and the path length L (m).

One can adapt the law to include the wavelength spectrum. This adaptation is made by taking into account the profile of the incoming light and the profile of the cross-section[44,45]

$$A = 1 - \int_{-\infty}^{\infty} \frac{I(\nu)}{I_0} \exp(-n \cdot \sigma(\nu) \cdot L) d\nu. \tag{3}$$

An integral over frequency (ν) is introduced and a frequency dependence is added to the cross-section. The exponent is weighted using the ratio of light with that selected frequency to the full light intensity I_0, as shown by $\frac{I(\nu)}{I_0}$.

The incoming light spectrum can have many shapes. However, in this thesis, this incoming light will be laser light, which is generally (or can be approximated as) a Gaussian shape in the frequency domain. A Gaussian is defined as follows[46]

$$g(x, \mu, \sigma) = \frac{1}{\sigma\sqrt{2\pi}} \exp\left(-\frac{1}{2}\frac{(x-\mu)^2}{\sigma^2}\right). \tag{4}$$

The mean is μ, and the width of the Gaussian is σ.

Atomic absorption is characterized by atomic resonances, discrete transitions from one atomic state to another. For tin in the relevant regime, all transitions originate from the $5s^2 5p^2$ state of tin. During the transition, one electron moves to a higher state, such as 5d, 7s, or 8d. More information on atomic transitions in tin in the UV, including a Grotian diagram and an overview table, can be found in Appendix A. The cross-section of these transitions can be related to the Einstein coefficient for spontaneous emission (A_{ki}) of that transition.[44–47] The relation between the cross-section and the Einstein coefficient for spontaneous emission (A_{ki}) can be written as follows[44,47]

$$\sigma(\nu) = \sigma_0 \chi(\nu) \text{ with } \sigma_0 = \frac{1}{4}\frac{g_2}{g_1}\lambda_{21}^2 A_{21}. \tag{5}$$

This equation shows that the cross-section can be split into σ_0, which determines the total strength, and the line shape function, which determines the broadening. σ_0 ($\mathrm{m^2\,s^{-1}}$) is determined by the central wavelength of the atomic line λ_{21} (m), and the Einstein coefficient A_{ki} ($\mathrm{s^{-1}}$) of the transition. The degeneracy of the initial and final atomic state, g_1 and g_2, are also part of σ_0. The frequency dependency of the cross-section is given by the line-shape function $\chi(\nu)$. $\chi(\nu)$ is normalized and thus determines both the width and the height, as widening causes a decrease in peak strength.

As mentioned, the line shape function determines the broadening and peak strength of the atomic lines. Several mechanisms can broaden the lines beyond the minimum *natural* width. Section 3 will go into detail on broadening mechanisms and determine which are relevant to this application. Broadening mechanisms can be *homogeneous* or *imhomogenous*, where homogeneous means the mechanism impacts all atoms in the same way. In general, imhomogenous mechanisms cause a Gaussian shape, as shown in Eq. (4). Homogeneous broadening effects cause a Lorentzian shape, which is defined as[46,47]

$$L(x, x_0, \gamma) = \frac{\frac{\gamma}{2\pi}}{(x - x_0)^2 + \left(\frac{\gamma}{2}\right)^2}, \tag{6}$$

where γ is the full-width-at-half-maximum (FWHM) and x_0 the center location.

A Voigt profile can describe a final broadened line profile. A Voigt profile combines a Gaussian and a Lorentzian shape. It is needed when two broadening mechanisms that cause a different profile are similar in size. A Voigt profile is defined as[46]

$$V(x, \sigma, \gamma) = \int_{-\infty}^{\infty} G\left(x'; \sigma\right) L\left(x - x'; \gamma\right) dx', \tag{7}$$

with G and L being the Gaussian and Lorentzian distributions respectively. This integral can be evaluated to yield[48]

$$V(x, \sigma, \gamma) = \frac{\mathrm{Re}[w(z)]}{\sigma\sqrt{2\pi}} \text{ with } z = \frac{x + i\gamma}{\sigma\sqrt{2}}. \tag{8}$$

Here, $\mathrm{Re}[w(z)]$ is the real part of the Faddeeva function, which can be computed numerically.

One can use the found line broadening profile to evaluate Eq. (5). If the spectral shape of the laser is known, everything required to evaluate Eq. (3) is known, and the absorption due to atomic absorption can be calculated.

2.2 Mie scattering on nanodroplets

Mie scattering can predict absorption spectra when nanodroplets are present in the vapor. This will be the case if the vapor has not fully atomized. Mie scattering is also known as the Mie solution to Maxwell's equation or Mie theory. It describes the scattering of an electromagnetic wave by a sphere in the absence of charges and currents. Mie scattering is most applicable if the sphere's radius is between a single wavelength and a tenth of the wavelength.[49,50] For larger spheres, optical scattering calculations are more relevant.

The Mie scattering theory is well described in the available literature. Because of this, most of the theory will be skipped for this thesis. Readers are directed to Bohren et al.[50] for more details.

Mie theory results in *efficiency coefficients* for scattering and extinction (defined as scattering + absorption). Physically, these efficiency coefficients show how well a nanodroplet converts incoming energy to scattering or absorption. The coefficients are also needed to calculate the cross-section of

a nanodroplet. The coefficients are defined as[50]

$$\begin{aligned} Q_s &= \frac{2}{k^2a^2}\sum_{m=1}^{\infty}(2m+1)\left(|b_m|^2+|c_m|^2\right), \\ Q_e &= \frac{2}{k^2a^2}\sum_{m=1}^{\infty}(2m+1)\Re\left(b_m+c_m\right). \end{aligned} \tag{9}$$

Here, a is the radius of the sphere that the light is hitting. m, b, and c are separation variables. k is the wave vector, defined by $k^2 = \omega^2\varepsilon\mu = \frac{\omega^2 n^2}{c^2}$, where n is the complex refractive index and ω the angular frequency. To show the physics behind and relevant scaling of the coefficients, the definitions of k and ω can be used

$$\begin{aligned} Q_s &= \frac{2}{\left(\frac{2\pi a}{\lambda}\right)^2 n^2}\sum_{m=1}^{\infty}(2m+1)\left(|b_m|^2+|c_m|^2\right), \\ Q_e &= \frac{2}{\left(\frac{2\pi a}{\lambda}\right)^2 n^2}\sum_{m=1}^{\infty}(2m+1)\Re\left(b_m+c_m\right). \end{aligned} \tag{10}$$

The coefficients depend only on the refractive index of the material and the ratio of its radius to the wavelength of the probing light. Finally, the efficiency coefficient can be related to the cross-section[50]

$$\sigma_e \equiv Q_e \pi a^2. \tag{11}$$

Thus, just like the efficiency coefficients, the cross-section depends solely on the refractive index, the sphere's radius, and the probing light's wavelength. The cross-section of Mie scattering can be used to evaluate Eq. (3), resulting in the absorption due to Mie scattering.

In this thesis, it is assumed that there is no interference between atomic resonances and Mie scattering. Thus, if both atomic absorption and Mie scattering are present, one can add their cross-sections. Adding multiple absorption effects gives the final form of the Beer-Lambert law as used in this thesis

$$A = 1 - \int_{-\infty}^{\infty} \frac{I(\nu)}{I_0} \exp(-L \cdot \sum_i n_i \cdot \sigma_i(\nu)) d\nu. \tag{12}$$

2.3 Absorption versus extinction

The extinction cross-section is used instead of the absorption cross-section as absorption spectroscopy is often, in reality, extinction spectroscopy. Extinction is the total loss of intensity due to scattering and absorption. To illustrate, an observer looking straight at a light source through a vapor cloud cannot know whether or not the missing light has been absorbed or scattered.

The ratio of scattered light collected by the imaging setup is essential to determine whether or not absorption or extinction is the relevant parameter. This ratio is determined by the numerical aperture (NA). For example, a two-inch collection lens placed 0.1 m from a scattering point source will have a NA of 0.25 and only collect 1.6 % of the scattered light. Since the setup used in this thesis has a lower NA, the scattered light can be considered lost, just like any absorbed light. The low NA also means that any (re-)emission is irrelevant, as this will also not be captured by the imaging setup. Hence, extinction is the critical parameter, not absorption. Therefore, this thesis will present extinction spectra and not absorption spectra.

3 Modeling extinction spectra

The numerical model created to predict and explain extinction spectra is introduced in this section. First, relevant aspects of atomic absorption for numerical modeling will be discussed. The same will be done for Mie scattering. Next, the resulting model will be summarized and discussed. This summary will include an overview of the critical assumptions taken. Finally, the result of the model will be shown: predicted extinction spectra. It will also be discussed how to interpret the extinction spectra.

3.1 Modeling atomic absorption

As shown in Eq. (5), line broadening will determine both the peak strength and width of the atomic lines. In this section, several broadening mechanisms, their origin, and their impact will be discussed. For each mechanism, a conclusion will be drawn on whether or not they are relevant to the numerical model. First, homogeneous broadening mechanisms will be discussed, followed by inhomogeneous mechanisms. Other effects impacting line shape will follow last.

The impact of all broadening mechanisms will be given in wavenumbers (cm^{-1}). $1\,\mathrm{cm}^{-1}$ is $30{\cdot}10^9$ Hz. The effect of the mechanism on the $5p^2\,{}^3P_1 - 5p6s\,{}^1P_1$ 266.20 nm atomic resonance will be used as an example whenever needed. The Einstein coefficient of the 266.20 nm resonance is $1.1 \cdot 10^7\,\mathrm{s}^{-1}$.

Homogeneous: natural broadening

Atomic resonances can never be perfectly narrow as it is impossible to define the energy levels with exact precision. This effect is called natural broadening and is directly linked to the Einstein coefficient of spontaneous emission[46]

$$\delta\nu = \frac{A_i}{2\pi}, \tag{13}$$

where $\delta\nu$ is the FWHM of a line broadened by natural broadening (Hz) and A_i is the Einstein coefficient for spontaneous emission (s^{-1}). Natural broadening causes a Lorentzian line shape, like all homogeneous broadening mechanisms. Since Einstein coefficients for tin are never much higher than $1{\cdot}10^8\,\mathrm{s}^{-1}$, the natural broadening is limited to $\sim 0.003\,\mathrm{cm}^{-1}$. Therefore, natural line broadening is usually negligible. Regardless, it has been implemented in the model.

Homogeneous: collisional broadening

Atomic lines can also shift and broaden if collisions impact their lifetimes. This effect is collisional broadening. Collisional broadening can occur with other atoms but also with electrons. In this work, pressure broadening will refer to collisional broadening with atoms. Stark broadening will refer to broadening due to electrons. Collisional broadening has two contributions: elastic and inelastic collisions. Inelastic collisions shorten the lifetime of the upper state. This effect causes a broadening with a FWHM defined as[46]

$$\delta\nu = 2\sigma_{ik} n \sqrt{\frac{2k_B T}{\pi\mu}}. \tag{14}$$

Here, n is the density of the colliding particles, and μ is the reduced mass of the colliding particles, given by $\frac{m_1 m_2}{m_1+m_2}$; σ_{ik} is the cross-section of the collision between the two particles. As can be seen, this equation can be applied to both electrons colliding with atoms to give Stark broadening or atoms with other atoms for pressure broadening. Elastic collisions cause a change in the distribution of energy levels as the nucleus interacts with a nearby one. The shift in energy levels is positive when

the interaction with the other species is repulsive. The opposite is true for an attractive interaction. Elastic collisions can lead to an overall broadening in energy levels and a shift in the most probable energy level. This shift in the most probable level will also change the wavelength of light required for the resonance, resulting in a line shift.[46] The broadening and shift caused by the elastic collisions is defined as[46]

$$\delta\nu = n \cdot \vec{v} \cdot \sigma, \tag{15}$$

where the σ is different for broadening and shift effects. $\vec{v}$ is the mean relative velocity between the species. Elastic collisions can also cause asymmetry in the resonance as the transition probability can have extrema since it depends on the inter-nuclear distance.[46] The asymmetry effects are not modeled as they are considered out of scope; however, they could be present in the experiments and thus will be discussed when applicable.

Stark broadening can be as large as $1\,\mathrm{cm}^{-1}$ with an accompanying shift caused by elastic collisions in the order of 0.005 nm.[51] Stark broadening can also cause asymmetric effects. However, this is for a high temperature of around 1 eV or 11 000 K. Stark broadening can be effectively ignored in this application, as the expected temperature in the vapor and thus the density of electrons is significantly lower.

The effect of pressure broadening can be estimated by taking a typical cross-section of $1 \cdot 10^{-16}\,\mathrm{m}^{-2}$ and a typical density of $1 \cdot 10^{24}\,\mathrm{m}^{-3}$ at a temperature of 2875 K. In this case, Equation 14 results in a $\delta\nu$ of $0.54\,\mathrm{cm}^{-1}$. Pressure broadening has also been studied in literature where broadening between 0.22 and $0.24\,\mathrm{cm}^{-1}$ per $1 \cdot 10^{25}\,\mathrm{m}^{-3}$ has been shown at 353 K.[52] Thus, pressure broadening can have a significant contribution to the broadening. However, the cross-section is challenging to estimate as this differs depending on the interaction between the two colliding elements. To conclude, both the elastic and inelastic components of pressure broadening are turned off in the model until accurate values for σ are found.

Homogeneous: saturation broadening

Saturation broadening occurs when the excitation rate due to incoming light outpaces decay back to the ground state. This leads to a depletion of the initial ground state, causing additional line broadening.[46] The broadening is quantified by the *saturation parameter* (S)

$$\gamma_s = \gamma\sqrt{1+S}, \tag{16}$$

where γ_s is the width after broadening. The saturation parameter can be related to the cross-section with[46]

$$S = \frac{\sigma_a I}{h\nu\gamma} \quad \text{with } \sigma_a = \frac{\pi^2}{4}\lambda^2, \tag{17}$$

where λ (m) is the wavelength of the atomic line and ν its frequency (Hz). h is Planck's constant and γ (Hz) the line width of the Lorentzian line shape. Filling in $S = 1$ and rewriting for I, the intensity of the incoming laser light, one can find the saturation intensity

$$I = \frac{4\gamma hc}{\pi^2\lambda^3}, \tag{18}$$

where c is the speed of light. The saturation intensity is $7.5\,\mathrm{W/m}^2$ for the example atomic line at 266.20 nm when assuming that the only broadening is natural broadening. Any additional broadening would increase the saturation intensity by increasing γ. This saturation intensity translates to a pulse energy of $\sim 2 \cdot 10^{-12}$ J for a laser with a radius of 5 mm and a pulse length of 4 ns. The probing laser in the experiments is expected to have a pulse energy of around 500 nJ and a bandwidth of $5\,\mathrm{cm}^{-1}$. The difference in bandwidth between the laser and the narrow (only naturally broadened)

resonance will cause only 0.0026 % of the energy to fall within the bandwidth of the resonance. This low spectral overlap results in $1.3 \cdot 10^{-11}$ J in-band pulse energy, equivalent to $S = 6$. This S would cause a 2.6x increase in γ. To conclude, saturation broadening can have an effect. However, the scale of the effect depends on the other broadening mechanisms and the bandwidth of the probing laser. It has not been added to the model for these reasons but will be checked experimentally.

Imhomogeneous: Doppler broadening

Doppler broadening is caused by the thermal motion of particles in random directions, Doppler broadening creates a Gaussian line shape, of which is he standard deviation is given by[46]

$$\delta\nu = \nu_0 \frac{v_{th}}{c} \tag{19}$$

where ν_0 is the central frequency (Hz). v_{th} is the thermal velocity, given by

$$v_{th} = \sqrt{\frac{2k_B T}{m}}, \tag{20}$$

where m is the mass of the particle and T is the temperature. The constants used are the Boltzmann constant (k_B) and the speed of light (c). Doppler broadening is significantly larger than natural broadening in this application. For example, Doppler broadening is $0.08\,\mathrm{cm}^{-1}$ for the atomic resonance at 266.20 nm at 2875 K (boiling point of tin at ambient pressure[53]). Doppler broadening is implemented in the model.

Doppler effects can also cause a shift, called the Doppler shift. The equation for the Doppler shift is similar to the equation for Doppler broadening[46]

$$\Delta\nu_0 = \nu_0 \frac{v}{c}. \tag{21}$$

This equation assumes that the speeds are non-relativistic, which is a good approximation for this application. A shift can only be caused by collective motion in the direction of the observer or, in this case, in the direction of the laser. The Doppler shift can be ignored in this system since there is no such collective motion.

Other: hyperfine structure effects

The hyperfine structure of the atom can also cause a shift or broadening of atomic lines. This effect is caused by the different hyperfine levels having slightly different energies and thus different transition wavelengths. These shifts are often small and thus can also be seen as (asymmetric) broadening if one's resolution is not high enough to distinguish the different peaks. The effect has been studied for the tin atom.[54–56] The main isotopes of tin are Sn^{116} to Sn^{120}, with the even isotopes being the most prevalent.[57] It has been shown that the odd isotopes cause the most significant broadening effect, with a broadening of around $0.2\,\mathrm{cm}^{-1}$.[54] This effect is expected to be obscured by the laser bandwidth. The odd isotopes are also not very common. Therefore, it is not added to the model.

Other: laser line shape

As alluded to, the line shape of the probing laser also affects the observed line shape. If the laser has a non-zero width, the observed line width will be some combination of the bandwidth of the laser and the width of the line (a quadratic sum in the case of two Gaussians). Therefore, the laser bandwidth puts a lower limit on the visible line width. Any asymmetry in the laser spectrum will

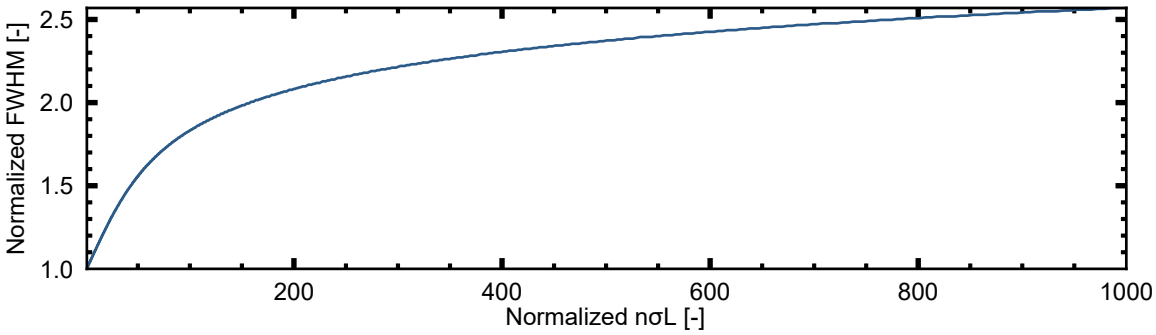

Figure 6: A visualization on how the observed FWHM of an atomic line increases as $n\sigma L$ is increased orders of magnitudes. The underlying cross-section shape is kept constant.

also be visible in the observed extinction spectrum, assuming that the laser bandwidth is not much smaller than the line width. Asymmetry effects are not modeled, as all probing light sources are assumed to be perfect Gaussians.

Other: optical depth broadening

One final and critical line shape effect is optical depth or opacity broadening. In this thesis, it will be referred to as optical depth broadening. Optical depth broadening is not a *real* broadening mechanism as it does not increase the width of the cross-section. Optical depth broadening originates from the exponent in Eq. (3), which causes the peak absorption to increase slower than lower absorption values, effectively increasing the FWHM. This effect is already visible at relatively low extinction values such as 10 %. Figure 6 shows how this effect can more than double the observed FWHM while the underlying cross-section is unchanged. Optical depth broadening and the effects of laser bandwidth ensure that the width of the observed resonance does not directly translate to a specific width of the underlying cross-section.

With the line broadening obtained, one can use Eq. (5) combined with a Voigt profile (Eq. (7)) as a line shape function to find the cross-section for a single atomic line. Repeating this for every line gives the full atomic absorption spectrum.

3.2 Modeling Mie scattering

In this work, the `miepython`[58] package will be used to calculate the scattering and extinction coefficients of Eq. (10). Another package, `pymiescatt`[59] was also tested, but `miepython` was found to be the quickest. Both packages require two inputs: the *size parameter* and the complex refractive index of the scattering medium. Both codes result in the same parameters, such as the scattering and extinction coefficients.

Using `miepython` leaves only three steps: First, one should know the complex refractive index for tin for every wavelength. The refractive index is obtained by taking the data from a literature source, Cisneros et al.,[60] who provide tin refractive index data for multiple temperatures between 310 nm and 12 µm. A fit is done to ensure that a value is available for every wavelength (including below 310 nm). Second, one should supply a *size parameter*. This size parameter is defined as $\frac{2\pi r}{\lambda}$ where λ is the wavelength, and r is the radius of the nanodroplet. Finally, the obtained coefficients can be converted to a cross-section using Eq. (11).

Checks have been done to ensure that the results of `miepython` are accurate. `miepython` and `pymiescatt` have been cross-checked and obtained the same results. `pymiescatt` also has been used in publications by its author successfully.[61–63] Thus, the output of `miepython` is considered valid as well and thus can be used to calculate the Mie scattering cross-section spectra.

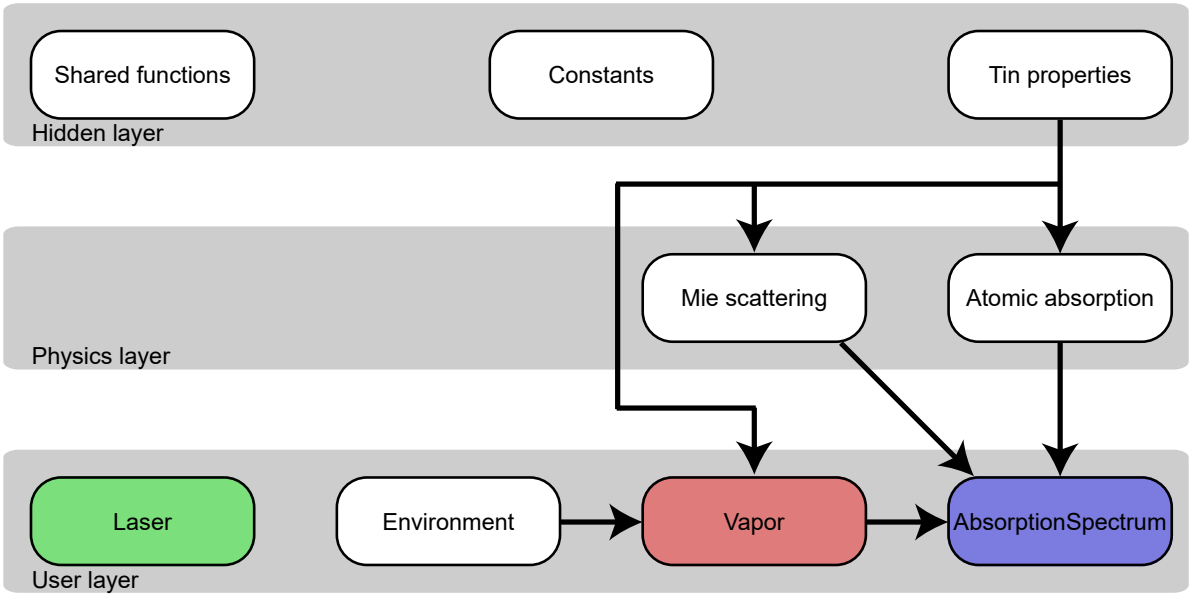

$$T = \frac{I}{I_0} = \int_{-\infty}^{\infty} \frac{I(\nu)}{I_{total}} exp(-L \sum_i n_i \sigma_i(\nu)) d\nu$$

Figure 7: The structure of the model. The top two layers are hidden to the user, while most of the calculations are done in the *physics layer*. The *user layer* are the four *classes* that the user interacts with to create an extinction spectrum. The colors indicate which class is responsible for solving which part of the Beer-Lambert law.

3.3 Overview & assumptions

In this section, an overview of the resulting model will be given. The critical assumptions taken in the model will also be summarized.

The model is implemented in Python and separated into parts, each with a clear purpose. This separation is done using an object-oriented structure, which means that there is a `Laser` *class* that holds all the code and properties relating to the laser. The same is done for other parts. This *class*-based structure allows for intuitive structuring of the code. Any further coding details will be omitted. For details, see Appendix B. An overview of the structure of the model can be seen in Fig. 7.

The model consists of three *layers*. The top layer is the *hidden layer*, which holds information that is used everywhere, such as essential functions, NIST data,[64] and physical constants. Most of the calculation work is done in the *physics layer*, which consists of two parts: Mie scattering and atomic absorption. These two parts are responsible for calculating Mie scattering and atomic absorption information, implementing everything discussed earlier.

The final layer is the *user layer*. Each part in this layer depends on user input of some type. The user must specify info about the laser used, specifically its bandwidth (and wavelength if it is a fixed wavelength laser). The user must also give an environment where the extinction measurements are performed. This environment sets the temperature. Finally, the user must specify the properties of the vapor, the absorbing medium. This includes the path length, density, and atomized ratio. The atomized ratio is the mass percentage in atoms; the remaining mass will be in nanodroplets. These three parts are given to the `AbsorptionSpectrum` class, which then uses the parts in the

physics layer to calculate the extinction for that case. This can be done for a single wavelength or a wavelength scan.

The model has some key assumptions, which will be listed below with a summary of their motivation.

- No asymmetry is modeled, neither in the atomic resonance due to collisional broadening nor the laser line shape. This means that only Gaussian laser line shapes are used. This is done for simplicity. Asymmetry will be checked experimentally.
- The system is in Local Thermodynamic Equilibrium (LTE); hence Boltzmann and Saha-Boltzmann apply. This can be expected to be true for the predicted high-density, low-temperature vapor.
- The system is modeled to have no spatial or temporal dimensions. This means that a static and uniform vapor is modeled with a single path length through the vapor. This is done for simplicity and can be done as none of the modeled effects have any spatial or temporal dependency (except for the Doppler shift, which is irrelevant, as discussed).
- All the mass in the vapor is either in nanodroplets or atomic, as these cause the extinction effects expected.
- The only broadening mechanisms are natural, Doppler, and collisional broadening. There is no atomic line shift. The choice for these mechanisms has been described in Section 3.1. As mentioned, no asymmetric effects are included.
- Only atomic lines between 190 nm and 600 nm with defined Einstein coefficients according to NIST[64] are included. This is the relevant regime for the model. The lines cannot be modeled without an Einstein coefficient, although many more lines without defined Einstein coefficients exist. An overview of the lines in the UV can be seen in Appendix A.
- An unpolarized medium is assumed. This means that all atomic transitions are allowed. This unpolarized state of the vapor is the case as the dipole moments are not controlled. Thus, the dipole moments will not align to create an overall polarization of the vapor.
- There is no interaction between individual nanodroplets or between the nanodroplets and the atoms. This lack of interaction can be assumed to be valid as the nanodroplets are not closer to each other than the penetration depth of their evanescent fields. The model checks this by calculating the mean inter-droplet distance. The nearby atoms are also not expected to be dense enough to change the refractive index significantly, which is checked by calculating the absorption coefficient over the relevant length scales in the system.

3.4 Resulting spectra

With the assumptions & structure of the model specified, the information the model can give will be discussed in this section. The model can produce two outputs: the resulting extinction for a fixed wavelength laser and the extinction over a wavelength range such as obtainable with a tunable wavelength laser.

The fixed wavelength calculation results in an extinction value but also gives a plot such as in Fig. 8. This plot shows three key components. The first is the laser profile before and after going through the vapor. The laser profile before the vapor is normalized to one. The third and fourth components are atomic absorption and Mie scattering cross-sections. The plot lets the user see which process is the dominant extinction process and which (spectral) part of the laser is absorbed. For example, Fig. 8 shows that Mie scattering is dominant everywhere except for a narrow part in the center where the atomic resonance is dominant.

Examples of the result of the tunable wavelength method can be seen in Fig. 9. The plot shows the extinction over wavenumber, with the corresponding wavelengths added for clarity. The user can set the scanned range. These plots can be used for two things: First, they can be used to predict and prepare the experiments to follow. For example, the model can show what kind of behavior can be expected from the Mie scattering background. Second, it can also show which atomic peaks

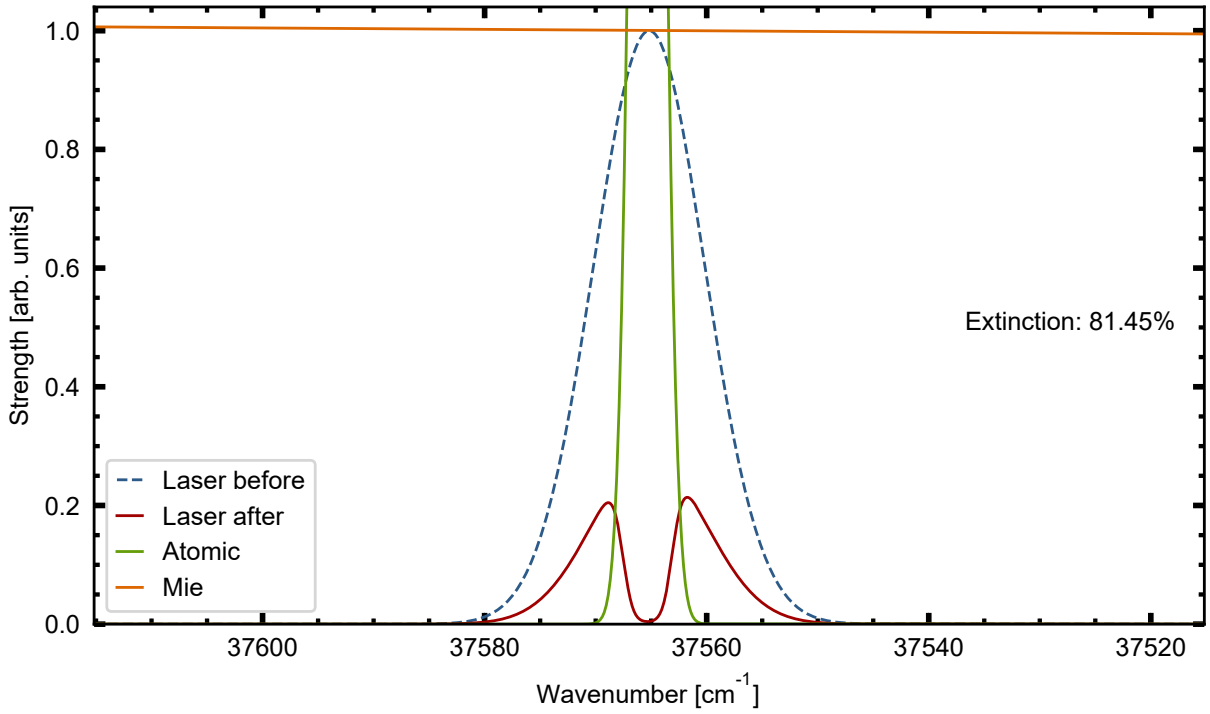

Figure 8: An example of a plot resulting from a fixed wavelength calculation. In this case, a laser hits the atomic line at 266.20 nm. The plot shows three aspects. First, the laser intensity over frequency before and after passing through the vapor. The laser strength is normalized to one. It also shows the cross-sections of Mie scattering and atomic absorption. The cross-sections are normalized to be one at $37\,570\,\mathrm{cm}^{-1}$. The cross-sections show that the extinction on the edges of the line width of the laser is due to Mie scattering, not the atomic line. This can be seen as its cross-section is higher than the cross-section of atomic absorption in those areas. Finally, the actual extinction value is also shown.

are expected to be strong and easily measurable for a particular vapor. In short, the model is used to select atomic lines to measure and get a feeling for the impact of other experimental parameters such as density and temperature.

The second function of the model is to relate the measured spectrum to the physical properties that cause this spectrum. Figure 9 shows several spectra. In all cases, the column density is $7 \cdot 10^{20}\,\mathrm{m}^{-2}$ and the bandwidth of the scanning laser is $5\,\mathrm{cm}^{-1}$. The varied parameters are mentioned in the legend. Figure 9a shows the behavior of the atomic resonances. The temperature dependence is shown. A different temperate will change the occupation of ground states and thus change the strength of the resonances. For example, the 286 nm resonance is stronger at 1500 K as it originates from the ground state of neutral tin. On the other hand, some resonances, such as the 326 nm are significantly stronger at 3000 K since they originate from a more energetic state. The model also has the option to add *additional* broadening to the resonances. The additional broadening feature could be used to better match an experimental spectrum where the model cannot explain the observed broadening and is shown in Fig. 9a. Broadening the cross-section of the resonances increases the overall extinction as a large spectral part of the incoming light is absorbed.

Figure 9b shows how the Mie scattering background can change when changing the nanodroplet size. For these spectra, both cases have a temperature of 3000 K. The only differences are the ratio between atoms and nanodroplets and the nanodroplet size, which significantly impacts the appearance of the spectra.

The model shows three key factors to look out for in the to-be-measured experimental extinction spectra. The first is the total density and path length. The total column density will increase or decrease the total extinction over all wavelengths. The second is the ratio between nanodroplets and atoms. As the model shows clearly, the relative strength of the atomic absorption and Mie scattering components can give information about this. Last is the slope of the Mie scattering background. As mentioned in the theory section and shown in Eq. (10), the cross-section of Mie scattering depends on the size parameter $x = \frac{2\pi r}{\lambda}$. As the model shows, as soon as the probing wavelength is 7 to 10 times larger than the radius of the nanodroplet, the size parameter becomes small, and the cross-section starts to decrease. The exact wavelength of the decay onset also depends on the refractive index. This decay onset or lack thereof can indicate the nanodroplet size in an extinction spectrum. A flat background due to Mie scattering indicates a nanodroplet size beyond ten times larger than the measured wavelength. In contrast, a strongly decreasing background indicates a small nanodroplet size. Suppose a *kink*, as seen at ∼250 nm in the blue curve of Fig. 9b can be found. In that case, the nanodroplet size can be determined even more accurately. Case-in-point, the position of the kink at 250 nm is a clear hint of the 30 nm nanodroplet size used in that calculation by the model.

To conclude, a model was developed to predict extinction spectra caused by Mie scattering and atomic absorption. The model is used to predict spectra and thus optimize the experimental measurement. It can also be used to explain any measured spectrum by comparing the modeled spectrum to the experimental spectrum. Three key features that impact spectra are identified. The first is the height of the entire curve (indicating column density). The second is the ratio between the atomic peaks and the Mie scattering background (atomized ratio). Last is the slope of the background curve (nanodroplet size).

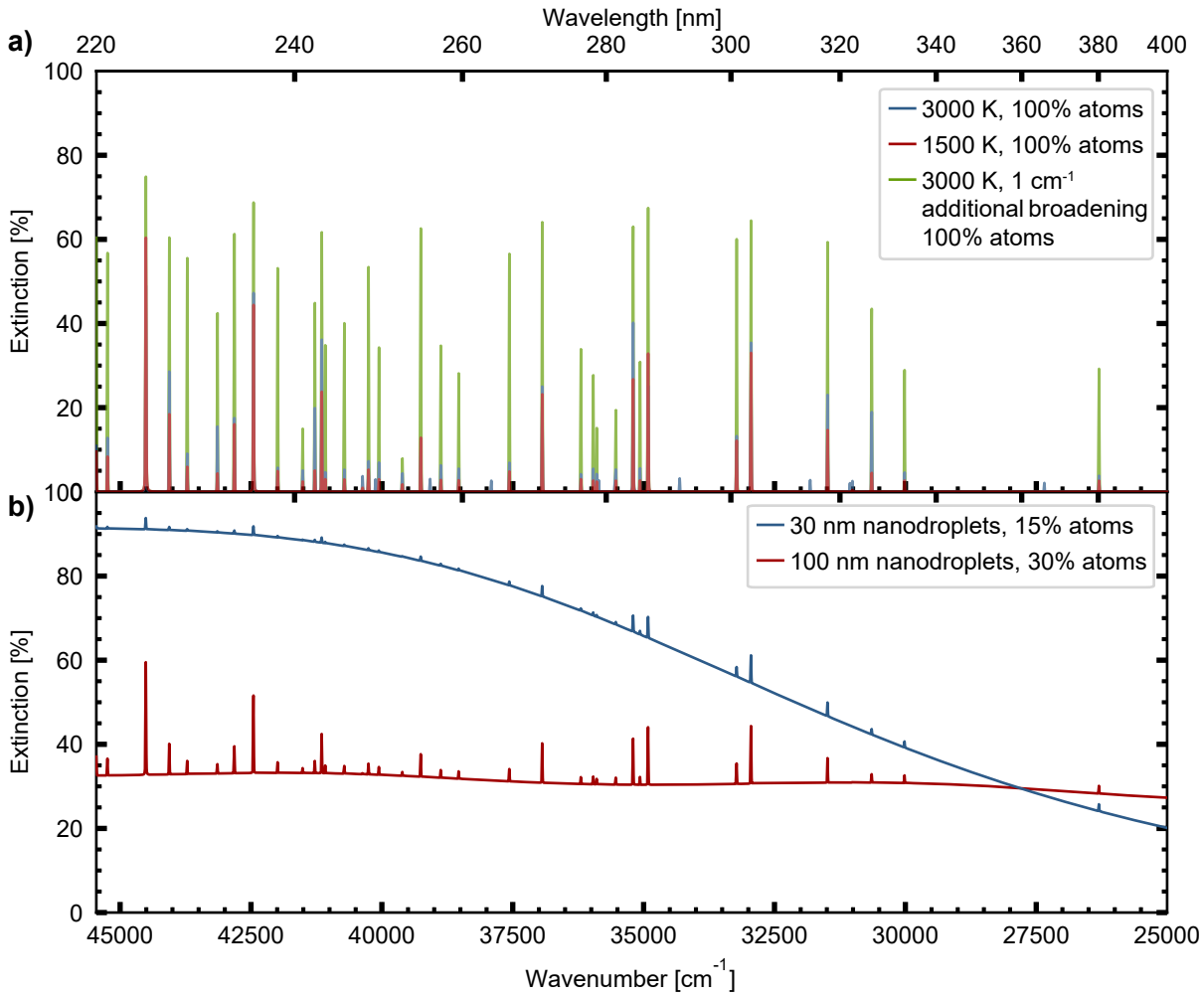

Figure 9: Examples spectra resulting from a tunable wavelength laser calculation. The primary x-axis is wavenumber (cm^{-1}). A second x-axis in wavelengths (nm) is added for clarity. Panel a) shows three cases with only atomic absorption enabled. The difference between the spectra is the temperature. For the green curve, *additional* broadening is added, which can be used when the model cannot explain the experimentally observed widths. Panel b) shows two spectra with both atomic absorption and Mie scattering. Two clear components in the extinction can be seen: a background of Mie scattering with atomic peaks on top. The blue line shows a high density of smaller nanodroplets. In contrast, the red line shows a lower density of nanodroplets, but they have a larger size.

4 Experiment and Methods

The experimental setup and methods used to create extinction spectra that allow for the determination of the composition of the tin targets will be described in this section. The experiments are conducted on a specialized setup commonly referred to as *Dalek-II*[1], shortened to *DII*. The data generated is captured by an in-house developed program called *Sonic Screwdriver*[1] and the data analysis is done by an in-house developed Python package `dropy`. The setup and the surrounding data analysis codes existed before the start of this graduation project. New parts, both hardware and software, have been added throughout this project. Below, the entire setup will be discussed for clarity; however, the new parts will be presented in extra detail. It will also be explicitly mentioned which parts the author worked on by labeling the sections "Existing," "Improved," or "New." When the parts are improved or new, it will also be mentioned whether or not the author did this alone or as part of the Dalek-II team.

The generation of tin droplets will be discussed first, followed by the lasers used to generate the tin targets (pre-pulse and vaporization pulse). The metrology used to capture information about these targets will follow next. This metrology includes the new UV shadowgraphy. The methods used to capture data are explained. The automation of data capturing is also presented. This section ends with a discussion of the data analysis methods and a summary.

4.1 Existing: droplet generation

The experiment starts with the droplet generator. A train of liquid tin microdroplets (temperature T = 260 °C, density $\rho = 6968\,\mathrm{kg/m^3}$) is dispensed into the Dalek-II chamber by the droplet generator. Often, the droplets do not leave the droplet generator orifice entirely straight down. The droplet generator is mounted on bellows to compensate for this, allowing a tilt to align the resulting droplet stream to the center of the vessel. A vacuum ($\sim 1 \cdot 10^{-7}$ mbar) is created within the chamber.

The tin tank is pressurized with argon leading to a stream of tin. A waveform generator drives a piezo element incorporated in the nozzle of the droplet generator. As a result, the tin stream is broken up into droplets. The spacing between and the size of the droplets in this stream is well defined. Three critical parameters impact the resulting droplet size: the pressure in the tank, the nozzle's size, and the modulating signal's frequency. Following Kurilovich et al.,[65] who investigated these droplet generators in more detail, one can write the droplet diameter as

$$D_0 = B f^{-\frac{1}{3}} p_{\mathrm{Ar}}^{\beta}, \tag{22}$$

where D_0 is the diameter in µm and p_{Ar} the argon gas pressure in bar. f is the frequency of the modulating signal in kHz, which typically ranges between 10 to 40 kHz. B and β are semi-empirical parameters. The -1/3 power law can be derived using mass conservation.[65] The uncertainty in the droplet size is ± 0.5 µm.[26]

The droplet passes through a horizontal sheet of light created by a helium-neon laser to ensure proper pre-pulse (PP) to droplet alignment. The sheet is placed a few millimeters above the vessel's center to ensure that the PP arrives at the right time to hit the droplet in the vessel's center. The exact location of the sheet has to be tuned depending on the stream velocity and other parameters. The droplet scatters the light of the helium-neon sheet, and this light is collected and detected by a photo-multiplier tube. The photo-multiplier tube picks up a burst of scatter for each droplet, resulting in a repeating signal with a kHz frequency. This kHz signal is downsampled to 5 Hz, the desired frequency of the experiment (the cameras limit this). This 5 Hz signal is the starting trigger for the experimental setup, as it triggers the flashlamp of the pre-pulse. All other timings are defined relative to this moment.

[1] The EUV Plasma Processes lab has a Doctor Who naming theme.

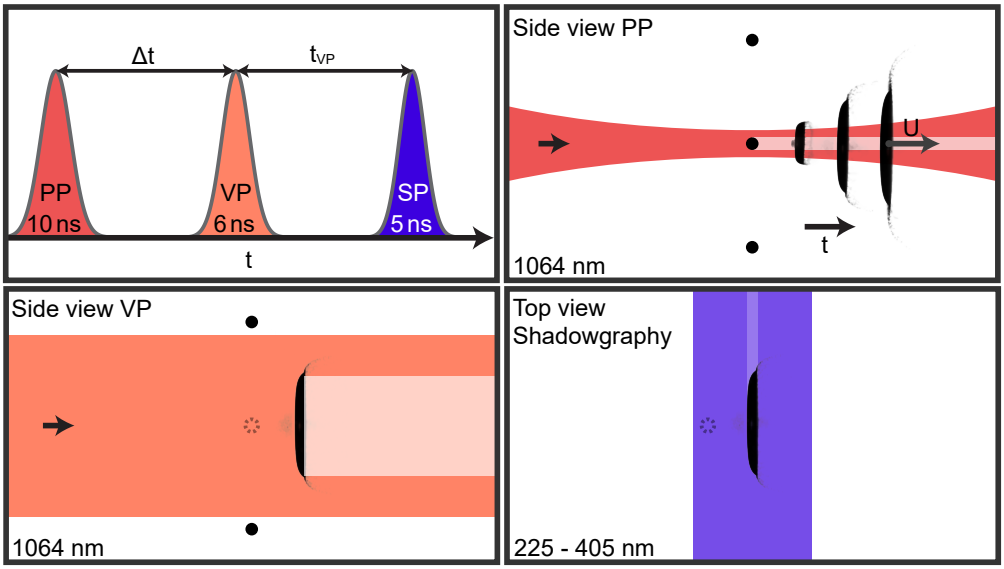

Figure 10: A schematic overview of the laser pulse sequence. The top left shows the order of the pulses. The pre-pulse (PP) starts, followed by the vaporization pulse (VP). The UV shadowgraphy pulse (SP) is last. The three other frames schematically show the laser beam profiles as they interact with the target. The PP is focused and propels the droplet with a velocity U, while the VP is larger than the target. The same is true for the UV shadowgraphy. Figure modified from [26].

4.2 Existing: target creation

A pre-pulse (PP) and vaporization pulse (VP) are needed to create the desired targets. Both laser beams are circularly polarized with a wavelength of 1064 nm and originate from Nd:YAG systems. A schematic outlining the timing and sequence of these laser beams is visible in Fig. 10.

The PP is the first laser to hit the droplet. The helium-neon trigger signal ensures its timing. The PP is a Continuum Surelite 3 laser that outputs linearly polarized pulses. The pulses have a 10 ns Gaussian FWHM temporal profile and are focused down to a Gaussian spot with a size of 105 by 96 µm. The laser is seeded, where a single mode is encouraged by starting lasing using a smaller 'seed' laser. The beam profile can be seen in Fig. 11. The energy of the PP can be set to up to 150 mJ. The energy can be changed using a tunable waveplate plus a thin film polarizer combination. This combination lets a certain fraction of the pulse pass based on the waveplate orientation. The polarization is changed to circular just before entering the Dalek-II vessel. The focal spot position is stabilized using an MRC Compact laser stabilization system. Better pointing stability leads to better repeatability of the target formation.

The VP is a Litron Nano T 250-10 laser. The laser has a 6 ns Gaussian FWHM temporal profile and is unseeded. Thus, this temporal profile is *spiky*. The beam is a Gaussian spot with a size between 1.0 and 1.1 mm. This large size is chosen to create a uniform fluence for the entire target. The beam profile can be seen in Fig. 11. The energy of the VP can be set to up to 35 mJ and is tunable in a similar manner to the PP. The VP is not stabilized as the pointing stability is satisfactory, especially considering the large focal spot.

The temporal shape of the VP can be adapted using a *delay line*. This delay line splits off a fraction of the pulse and sends it through a longer path, delaying this fraction of the pulse in time. The result is a 13 ns FWHM temporal profile, consisting of two successive pulses. The delay line can reduce the intensity of the VP without reducing the fluence. A reduced intensity is desired as too high intensities cause plasma formation, ruining the extinction measurements by emitting light.

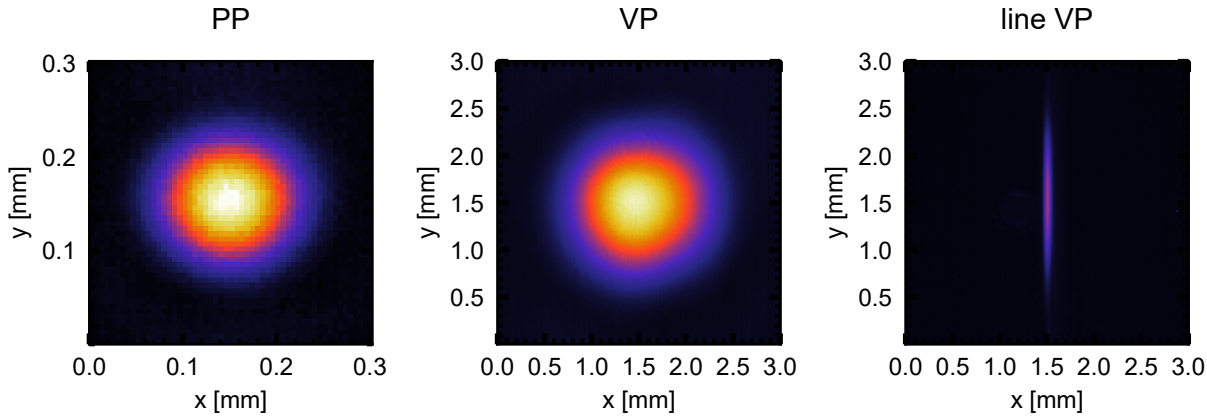

Figure 11: The beam profiles of the PP and the two configurations on the VP. Note the tenfold difference in scale for the PP and the VP, the PP is significantly smaller.

Due to the longer path length of one of the beams, this beam has expanded more, as the beam is slightly divergent. This slightly different size means that the energy in the two branches is not equal but tuned to ensure equal peak fluence in the chamber.

An alternative configuration of the VP is also used, called the *line VP*. This configuration can be operated both with and without the delay line. One axis of VP is focused using a set of cylindrical lenses. The short axis has an FWHM of ∼65 µm, while the long axis has an FWHM of approximately a millimeter. The beam profile can also be seen in Fig. 11. The non-line VP is referred to as the *full VP*.

A schematic of the PP and VP in the vessel can be seen in Fig. 12.

4.3 Improved: metrology

Existing: overview & green shadowgraphy

Three systems are in place to capture information about the target. First is the green shadowgraphy. This system was in place before the start of this project. The second is the UV shadowgraphy. This system was added during this project and is the primary tool for this thesis. Last, several Keysight oscilloscopes are part of the setup. These can measure analog signals, such as photodiodes for timing, target information, or exposure times of cameras. The configuration of these oscilloscopes changes per experiment and will not be discussed further. The oscilloscopes are generally a secondary tool in this thesis; the primary tool is the UV shadowgraphy.

The light for the green shadowgraphy is broadband fluorescence from pumped dye cells with a wavelength of 560 nm (12 nm FWHM). The pulses are 5 ns long. They are made partially spatially incoherent by transporting the light through a hollow-core fiber. This incoherency reduces speckle and diffraction in the images.[25] The target is imaged using two Infinity K2 Distamax long-distance microscopes combined with AVT Manta G-145B NIR PoE CCD cameras. The imaging system has a spatial resolution of approximately 5 µm.[25] The long-distance microscopes are placed at a 90° angle for a side view and a 30° angle for a rear view. The top view of Fig. 12 also shows the green shadowgraphy.

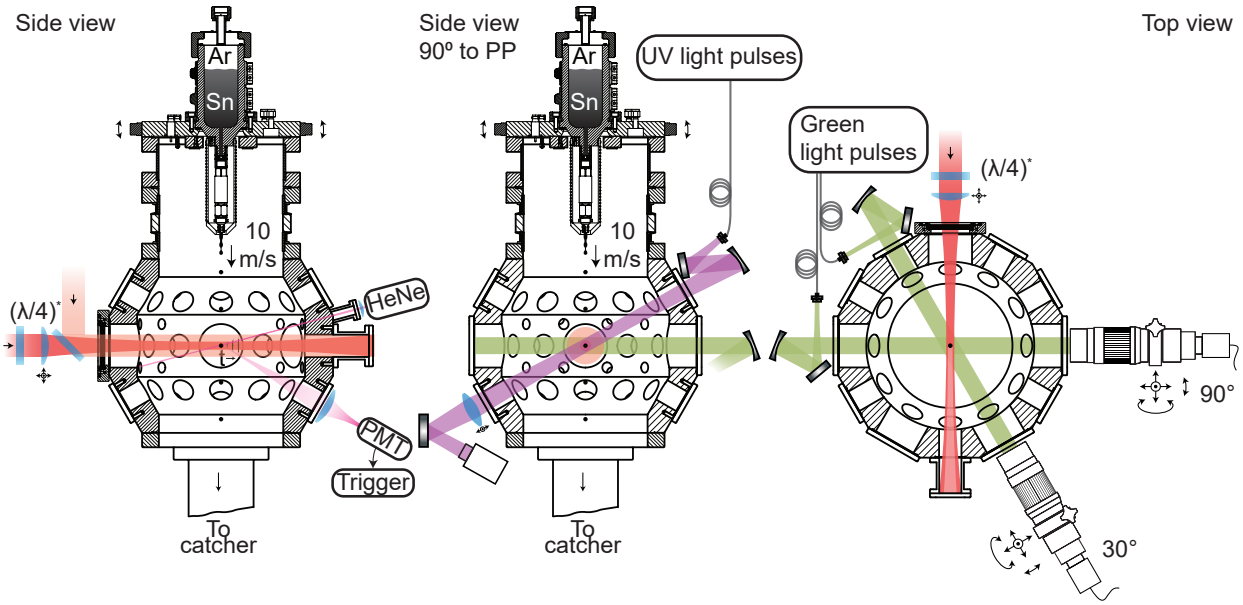

Figure 12: A schematic of the *Dalek-II* chamber. The left shows a side view, showing the PP and VP path through the chamber. It also shows the triggering system. The middle shows a side view, but at a 90° angle to the PP. This view shows the side view UV and green shadowgraphy paths. The collinear path of the PP and VP can also be seen again. Some optics are omitted from the UV shadowgraphy entry and exit for simplicity. The camera of the green shadowgraphy is also omitted to save space. The important optics such as the movable collection lens just after the vessel are pictured. The right image shows a top view, showing the setup of the green shadowgraphy. From the top view, the UV shadowgraphy is collinear with the 90° green shadowgraphy path. It is omitted for clarity. Adapted from [66].

Group effort: UV shadowgraphy

The novel UV shadowgraphy system starts with a Continuum Surelite-EX Nd:YAG laser that outputs hundreds of mJ of 355, 532 and 1064 nm light (the Nd:YAG harmonics). The ratio of these harmonics can (and must) be tuned to ensure optimal UV output. The UV output is generated by a Continuum Horizon II optical parametric oscillator (OPO). Briefly, this laser uses the Nd:YAG harmonics from the Surelite-EX to generate light with any wavelength between 190 and 2100 nm. It does this by mixing and doubling different wavelengths until the desired wavelength is obtained. The light between 190 and 400 nm is used for this thesis.

The UV light is transported to the Dalek-II vessel using a Laser Components FV-High-OH hollow-core fiber. The fiber is the limiting factor regarding the wavelengths used for the UV shadowgraphy. Its attenuation quickly triples below 240 nm, causing a significant transmission drop. The fiber fixes the UV shadowgraphy wavelength range between ∼225 and 400 nm. The light from the fiber enters the chamber at a 90° angle to the target. The light is also on a 30° incline relative to the table. A pco.ultraviolet CCD camera captures the UV shadowgraphy image. This camera is placed under this same 30° angle to ensure a right-up image. After passing through the target, the UV light is imaged by a single movable biconvex lens. This lens has to move as the wavelength changes, as its refractive index changes with wavelength. The image magnification changes with wavelength as the camera is not moved. This effect has been calibrated and is compensated for in the analysis. The path of the shadowgraphy (UV and green) through the vessel can also be seen in Fig. 12.

Author: spectrometer & UV shadowgraphy calibration

A part of the UV beam is scattered when coupling into the fiber. This light is collected by fiber connected to a Princeton Instruments SCT320 spectrometer. This spectrometer is used to accurately obtain the OPO laser's output wavelength. The output wavelength is desired to measure as it can be used to determine any atomic line shifts and easily place the UV shadowgraphy on an atomic resonance. The spectrometer uses a 1200 l/mm reflection grating, with efficiency optimized for UV light. The spectrometer is calibrated using a Princeton Instruments USB-Hg-NeAr HeNe + Hg calibration lamp between 220 and 410 nm. First, the peaks of the calibration lamp are fitted by a Gaussian. Then, their pixel position is linked to the peak position (vacuum wavelength) according to NIST.[64] A third-order polynomial is fitted to the pixel-vs-wavelength relation of all the found peaks to finalize the calibration. The resolution of the 1200 l/mm grating is 0.06 nm and the estimated precision of the overall technique is 0.01 - 0.02 nm. In reality, this calibration consists of several independent calibrations for different grating positions, as the chosen 1200 l/mm grating causes dispersion of ∼0.03 nm/pixel, limiting the visible range to ∼59 nm. Thus, the grating angle has to change as the OPO laser's wavelength changes to image the entire range. Fixed grating positions are chosen and calibration individually while being cross-checked. These positions span the 220 to 410 nm range desired. A detailed overview of this can be seen in Appendix C including an overview figure.

The output wavelength of the OPO laser is calibrated using the SCT320 spectrometer and a self-developed procedure. The OPO laser does not output the exact wavelength requested in its software. A significant difference exists between the requested and output wavelength of ∼3 nm, which varies with wavelength. The calibration ensures that the wavelength can be set accurately, with a precision of ∼0.03 nm. More detail about this procedure can be found in Appendix D.

The energy output has also been quantified using a Gentec QE50LP-H-MB-QED-D0 energy meter. The temporal shape of the laser pulse has been measured using photodiodes and has a (3.4 ± 0.2) ns FWHM. The spectral bandwidth of the OPO laser is quantified a 3600 l/mm grating in the SCT320 spectrometer. This spectral bandwidth has a significant on the measured atomic line shapes. More detail on this can be found in Appendix E.

To conclude, green and UV shadowgraphy are two main metrology tools in the Dalek-II setup. The green shadowgraphy was already present at the start of this project. The UV shadowgraphy was added (a joint effort from the whole Dalek-II team), produced by the OPO laser. A spectrometer is in place to check the OPO output. The author implemented this spectrometer and automatized its operation.

4.4 Improved: data capturing

Existing: overview

An in-house developed program called *Sonic Screwdriver* (SSD) is used to capture and synchronize all the data coming from the different cameras, scopes, and other devices. This program is developed by the AMOLF/ARCNL software department and hooks into many of the devices on the Dalek-II setup. The main functionality of SSD is to synchronize all the data capturing and provide a live view of the experiment for debugging and testing purposes.

SSD has three measurements: Run, Power, and Delay. The Run measurement is the default, where a certain number of samples are captured with the current settings. The user can select which data is stored, such as the Keysight scopes, Manta cameras, the pco.ultraviolet camera, or others. The Power measurement is similar but specific to power meters, allowing the user to measure the different lasers' pulse energy. The most complex measurement type is the Delay measurement. Here,

the timing of a single or set of devices is slowly changed. This timing change is done using SRS DG645 Delay Generators, which control the timing of the setup, such as the lasers and cameras. This measurement is a series of Run measurements with changing timings. For example, this measurement allows one to make a 'video' of an evolving target by taking a certain number of samples with a specific timing and then changing the timing slightly before repeating. Thus, the video is really a stroboscopic series of photos.

Author: Python scripting

The functionality of SSD is extended using Python scripting. SSD has the option to run Python scripts that hook into the program and allow the user to automate repetitive measurements and experiments. An extensive Python package called `OPOcontrol` was created during this project to this extent. `OPOcontrol` has a wide range of features as it has grown over time. For example, the code to calibrate the spectrometer is also part of `OPOcontrol`. However, its primary function is to automate scanning the wavelength of the OPO. A scan or extinction spectrum consists of many Run measurements at different UV shadowgraphy wavelengths. To speed this up, `OPOcontrol` automates these series of measurements using the Python scripting function in SSD. For example, one atomic line scan consists of 60 Run measurements and one Run measurement to measure the background illumination. Instead of running these manually, it can be done using `OPOcontrol`. The automation of `OPOcontrol` enabled a full atomic line scan with 60 measurements and 50 frames per measurement to happen within 20 minutes with only one person supervising. Without the

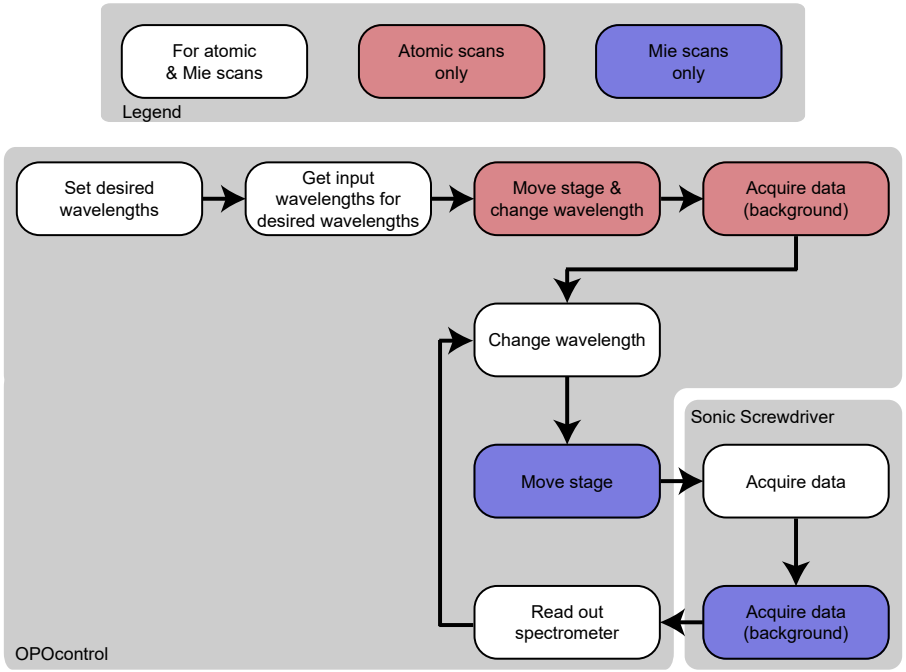

Figure 13: A flow chart of the `OPOcontrol` loop for atomic line scans and Mie scans. In both cases, the scan starts with input from the user (desired wavelengths) and getting the input wavelengths for those output wavelengths. This output wavelength refers to the OPO output wavelength calibration mentioned in the main text. The single background is made for an atomic scan, and then the main loop is entered for both scans. This main loop entails changing the wavelength (and the stage for Mie scans), doing a Run measurement (doing another Run for a background for Mie scans), taking a spectrometer readout, and repeating. This loop is continued until all the desired wavelengths have been measured.

automation, this would have taken at least twice as long and two people. Using `OPOcontrol` is also less error-prone, as one does not have to do repetitive tasks such as changing the wavelength or the name of the measurement. Additionally, it automates additional features, such as taking a spectrometer measurement every time the OPO output wavelength is changed. This ensures that the output wavelength can be checked.

`OPOcontrol` also has the option to communicate with motorized stages. This is used to move the imaging lens as the wavelength changes. This movement is necessary to keep the target in focus. In short, automation saves a lot of manual labor and time. `OPOcontrol` has two main automated loops: an atomic line scan and a Mie scan. A critical difference between the two is that the stage of the imaging lens is not moved to preserve the magnification during an atomic line scan. This lack of movement is acceptable as the wavelength change is small. Therefore, only one background is made per atomic line scan, as a background is made per stage position. For a Mie curve, the stage continuously moves as the wavelength changes, as the steps are larger than for an atomic line scan. Thus, backgrounds are made more often. A flow chart describing the steps taken during data acquisition (both by SSD and by `OPOcontrol`) can be seen in Fig. 13. For more details, see Appendix F.

To conclude, Sonic Screwdriver (SSD) is used to synchronize the data acquisition. The Python scripting function within SSD is used to run `OPOcontrol`, which automates many of the measurements by communicating with the OPO and spectrometer. It also controls the motorized stage of the imaging lens, ensuring that the target remains in focus during any scan. `OPOcontrol` is also used for the calibration of the spectrometer, the OPO wavelength output, and the imaging lens position for the desired wavelength (including the related magnification change).

4.5 Improved: data analysis

Existing: dropy

A Python package `dropy` developed at ARCNL is used to analyze all the obtained data. At the core, `dropy` is an image processing library specially tuned to the ARCNL data capturing environment and Sonic Screwdriver (SSD). It can read in Run, Power, and Delay measurements, obtain the scope, image, and power meter data for these measurements, and process them. While it can work with power meter data and the scopes, its primary focus is images. Extensive cropping, thresholding, and correction functions have been developed for these images. Properties like the center of mass position, tilt, propulsion, and radial size can be tracked. Most of these tracking functions work in two steps. The first step is to apply a threshold. The user can set the exact method, but the result is a boolean image. The second step is to process the boolean image. This processing can be used to find the center of mass (which finds the mean location of the accepted pixels), expansion (the uppermost accepted pixel versus the lowest accepted pixel), or any other properties mentioned above.

In addition to analyzing single measurements, `dropy` also has the option to work with sets of measurements, known within ARCNL as *beamtimes*. This feature allows the pairing of similar or relevant data.

Author: extinction measurements

The `dropy` package has been extended during this project to perform extinction measurements. This extension meant adding additional tracking functions to track the extinction in an image. The extinction method's first step is compensating for the magnification change that occurs when changing the wavelength. This effect was mentioned before and is compensated for by scaling all

images to the same magnification. The images are only scaled up to prevent data loss. An example of two shadowgrams without any magnification change can be seen in Fig. 14, emphasizing the importance of compensating for the effect as the target looks smaller in the higher wavelength image.

The next step is thresholding. By thresholding, the remaining rim of the target can be found. The tilt and the center of mass of the rim are then obtained using pre-existing methods. The user must also specify *boxes* in which the extinction is to be calculated. These boxes move with the center of mass and tilt. This movement ensures that the same position in the vapor (relative to the sheet) is sampled for every frame. The extinction in the box is calculated by comparing the mean pixel value in the box to the mean background pixel value. This comparison to the background is more accurate when correcting the background illumination than without doing so. This background correction is done by comparing the image to an image without any target. This correction removes spots on the camera and any uneven illumination, resulting in a more accurate mean background value. Figure 15 shows an overview of the method; the raw image, the boolean image to find the center of mass and tilt, and the (background corrected) image with the boxes drawn on it. The speckle in the images, which changes over wavelength (see Fig. 14), puts a lower limit on the size of the box that can be used. The speckle pattern can influence the found extinction if a box does not include multiple speckles. The sufficiently large *box* size used in this thesis, at least 20x20 pixels, results in no significant effect of the observed speckle on the found extinction, as it averages over at least 25 speckles. The final extinction per area (*box*) in the vapor is found by averaging over all frames.

The *beamtime* functionality is also extended to make extinction spectra by linking the extinction results for the individual measurements. Making the extinction spectra requires that the extinction has been found for the individual images. This data is then loaded in by `dropy` to make extinction spectra. In addition to making extinction spectra, individual peaks can be highlighted and fitted. Atomic peaks can also be excluded to create Mie curves. These functionalities allow for all the spectra shown in the next section.

To conclude, an existing Python code `dropy` is used for the data analysis. `dropy` has many features to enable easy processing of images from the Manta and pco.ultraviolet cameras. `dropy` is extended to allow for extinction measurements. This includes a new tracking function added to find the

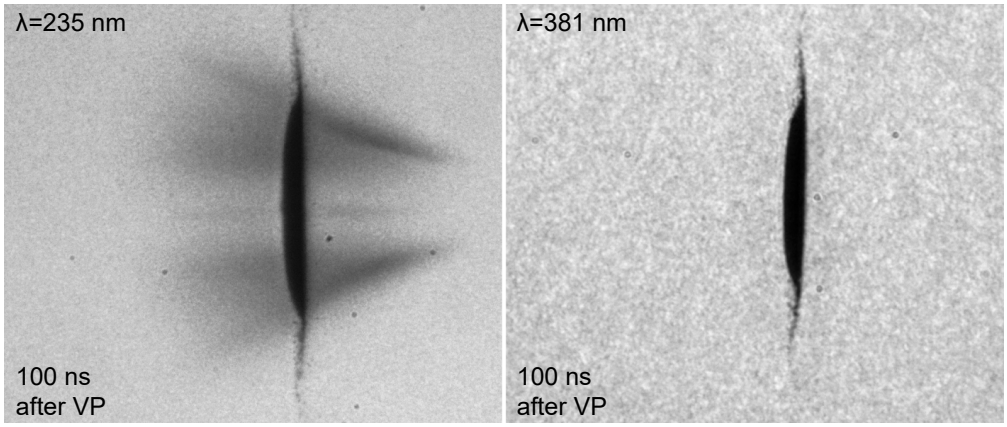

Figure 14: An example of two shadowgrams at two very different wavelengths, 235 and 381 nm. The target seems smaller in the 381 nm image due to the magnification change. Except for that, the different speckle sizes can also be noted. This speckle size sets a lower limit for the *box* size in the analysis.

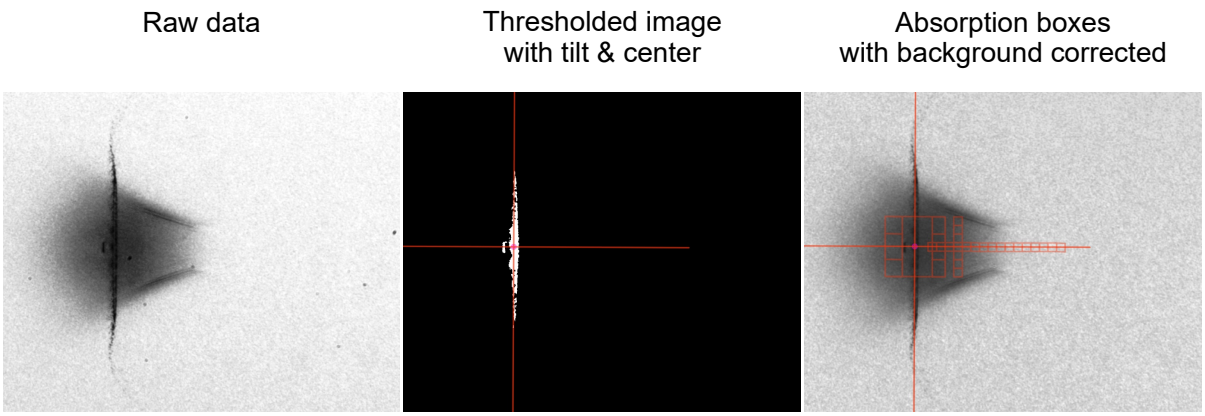

Figure 15: An illustration of the steps taken to get the extinction of a single image. On the left is the raw data without background correction. One can see spots on the camera and the uneven background. The middle shows the thresholded image, of which the tilt and the center are found. The right shows the *boxes* drawn relative to this tilt and center. The extinction is calculated for each of the boxes. Also, a background correction was applied.

extinction in measurements depending on the spatial location by defining *boxes*. The feature of `dropy` that allows for the grouping of measurements is extended to allow for the creation of extinction spectra and to analyze these spectra in greater detail.

4.6 Summary

This section introduced the setup and methods used for obtaining and analyzing the experimental results. The pre-existing *Dalek-II* setup is improved by adding UV shadowgraphy produced by an OPO laser. The UV light is guided to the vessel via a hollow-core fiber and enters at a 90° angle. The output of the OPO is quantified in detail by the author. The temporal and spatial laser-pulse profiles are checked, and the wavelength and bandwidth are calibrated. Data capturing is done via the software package *Sonic Screwdriver*, which is extended by the author's new Python code `OPOcontrol`, which automates the measurements done for this thesis. `OPOcontrol` also controls the readout of the SCT320 spectrometer and the movement of the stage on which the imaging lens is placed. Data analysis is done with a pre-existing Python code `dropy`. `dropy` is extended by the author to allow for extinction measurements. The extinction per spatial position is calculated using *boxes* that move with the target's center of mass and tilt. The extinction per wavelength is obtained by averaging over all frames captured with that wavelength backlighting of the OPO.

This page has intentionally been left blank.

5 Experimental results

The obtained experimental results will be shown in this section. First, the raw data will be shown to create an overview of the behavior of the tin vapor targets and show the versatility of the novel UV shadowgraphy. The extinction spectra created from these shadowgrams will be presented. Extinction spectra will also be presented for different targets, timings, and spatial locations.

5.1 Qualitative interpretation of UV shadowgraphy

Figure 16 shows the target evolution as seen with both the green and UV shadowgraphy. Figure 16a shows the deformation after the PP. The leftmost image is just before the PP, which is incident at 0 µs. In this thesis, all laser pulses propagate from left to right. In Fig. 16b, at 3.1 µs, the line-shaped VP illuminates and vaporizes a central slice of the sheet. Both subfigures in Fig. 16 also show a rear view. The rear view on the first row is recorded just before the VP, while the rear view on the second row is recorded just after the VP. This rear view is created using green shadowgraphy.

Figure 16 immediately shows the importance of the UV shadowgraphy. The UV shadowgraphy has significantly higher contrast than the green shadowgraphy; the vapor cloud is visible for the first time, as this is not the case for the green shadowgraphy. The visible structure shows that the vapor focuses or diverges depending on the side of the sheet. A diverging cloud is visible on the laser side (or rear side, left), while the front (right) converging behavior. A 'focus', i.e. point of convergence, can be seen at 3.40 µs, which is 300 ns after vaporization.

The white blob visible on the green shadowgraphy is the PP plasma emission. This plasma emission is visible on all green shadowgraphy images as the Mantas have µs trigger jitter and thus are forced to have long exposure times that always include plasma emission. The exposure of the pco.ultraviolet is more controlled than that of the Mantas as it has only 16 ns trigger jitter. Therefore, the PP plasma is not visible in those images.

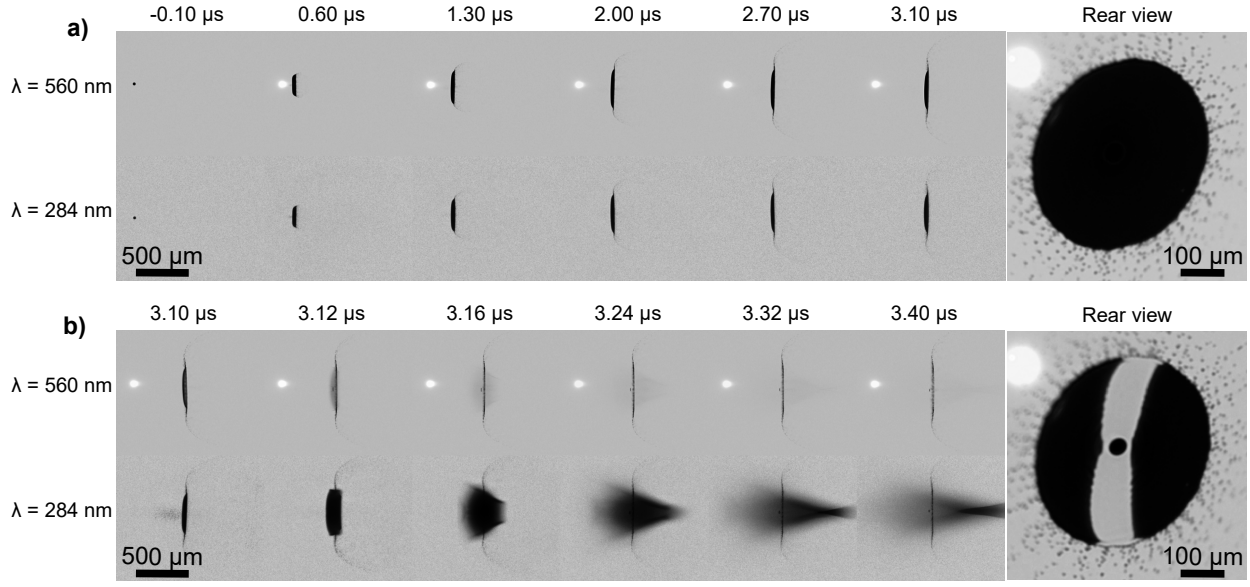

Figure 16: An overview figure showing the target evolution in a system with a pre-pulse (PP) and vaporization pulse (VP). The evolution after the PP is shown on the top row, in both green and UV shadowgraphy. A rear view after 3.1 µs is also shown. The second row shows the evolution after the VP. The rear view is recorded 10 ns after the VP, showing the vaporized slice using the line VP.

Figure 17 shows six UV shadowgraphy images of the same target at the same timing; the only difference is the wavelength of the UV shadowgraphy. Figure 17a shows three wavelengths around the 286.42 nm atomic resonance. Figure 17b shows three wavelengths away from any atomic resonance. For simplicity, these wavelengths are called *Mie wavelengths*. The magnification change is compensated for, and a background correction is applied as discussed in Section 4.

Figure 17a shows how the extinction increases significantly on an atomic resonance, proving the presence of atoms in the tin vapor for the first time. Figure 17b shows that the extinction due to Mie scattering also changes, decreasing as the wavelength becomes longer. Thus, UV shadowgraphy can prove the presence of both nanodroplets and atoms in tin vapor with only six images. This decrease in extinction means that the Mie scattering cross-section is also decreasing. As shown in Section 3, the onset of the decay in extinction occurs when the nanodroplet radius is 7-10 times smaller than the probing wavelength. Applying this to Fig. 17b and its apparent extinction decrease between the 381 and 303 nm puts an upper limit of ∼55 nm on the nanodroplet size. The last visible effect in Fig. 17 is best seen in the 235 nm image. This image best shows the spatial distribution of the nanodroplets. The same structures are visible when comparing this image to the 286.42 nm image. Both images show similar structures, such as the converging behavior and the higher extinction on the center line of the vapor. This similarity in structure indicates that nanodroplets and atoms occupy the same space and thus move together in the expansion following vaporization.

Figure 18 shows a comparison between a target vaporized using the full VP (a) and the line VP (b). Three wavelengths are shown. The rightmost is on the $5p^2\,{}^3P_0 - 5p6s\,{}^3P_1$ 286.42 nm resonance, while the other two are slightly off and far away from the resonance, respectively. It is immediately apparent that the overall extinction is higher with the full VP. This higher extinction is due to a higher column density caused by more mass being vaporized. Except for that, only minor differences can be seen. The line VP images and the full VP images show a similar structure that includes the converging behavior and a higher extinction area in the center. In short, both the line VP and the full VP will be used in this thesis. The line VP is preferred and will be used where possible. However, due to experimental time constraints, data with the line VP is not always available; in that case, the full VP will be used. The line VP is preferred as it is beneficial for matching the model as the path length is controlled and can be estimated by inspecting the rear view shadowgraph (as seen in Fig. 16).

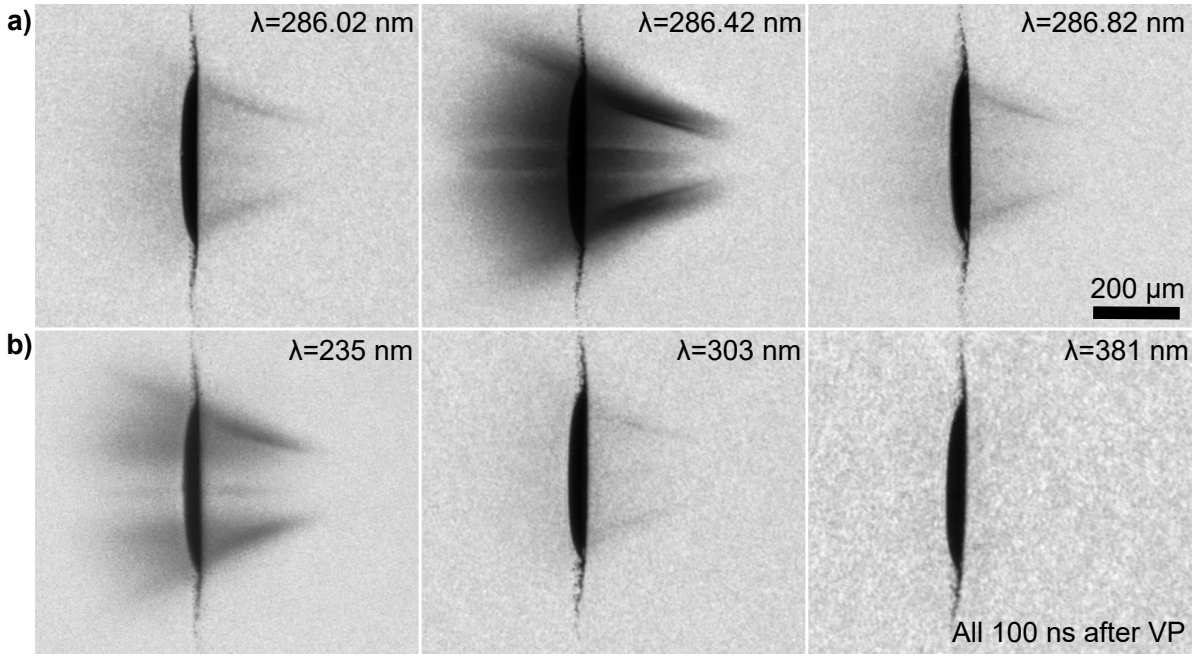

Figure 17: An overview of images of the same target with different wavelengths of UV shadowgraphy. Panel a) shows a narrow range around the $5p^2\,{}^3P_0 - 5p6s\,{}^3P_1$ 286.42 nm atomic resonance. This subfigure shows how the extinction significantly increases on the resonance. Panel b) shows a larger range, from 235 to 381 nm, to show the evolution of the extinction due to Mie scattering. The line VP is used in all cases. The time between VP and SP is 100 ns. The images are also scaled to constant magnification.

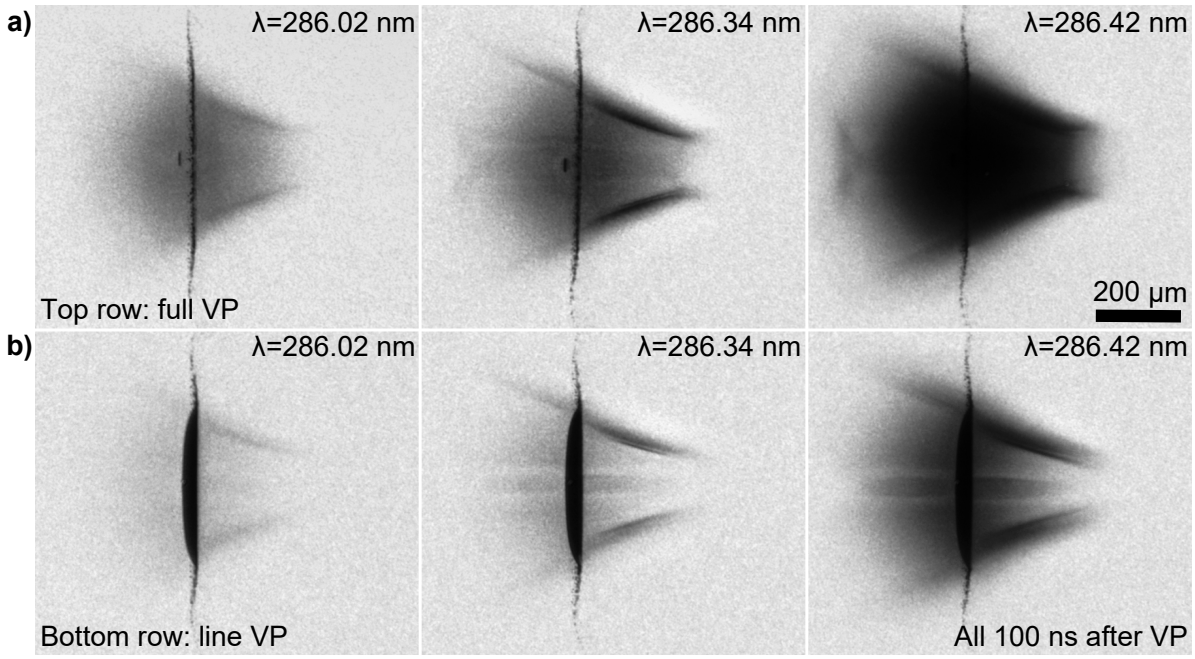

Figure 18: Overview images comparing the full VP to the line VP with different wavelengths of UV shadowgraphy. Panel a) shows three wavelengths, one off the $5p^2\,{}^3P_0 - 5p6s\,{}^3P_1$ 286.42 nm resonance, one on the resonance, and one in the tail of the resonance at 286.34 nm. Panel b) shows targets after being illuminated by the full VP. The bottom row shows the same target, except that the line VP is used to vaporize. The time between VP and SP is 100 ns.

5.2 Creating extinction spectra

The analysis method as explained in Section 4.5 can be applied to the raw data as shown in the previous section. As mentioned, the extinction can be spatially resolved by selecting a different *box*. In this section, the same box will be used every time. This box is located just in front of the sheet in the vapor center, as can be seen in Fig. 19d.

Figure 19a shows the full extinction spectrum of a tin vapor in the UV for the first time. The spectrum of Fig. 19a has the most data points in a single spectrum created during this project. The spectrum spans from 227 to 403 nm, showing multiple peaks on a decaying background. Each dot in the spectrum is a measurement consisting of 50 frames. This *target*, a vapor made with specific PP and VP settings, is made using the full VP and is called target A1. In this case, the whole settings are an initial droplet size of 27 µm, a PP energy of 28.8 mJ, a PP-VP delay of 3.1 µs, and a VP energy of 8.4 mJ. Hereafter, not all settings will be mentioned every time. A complete overview of the settings used to create all the targets mentioned in this thesis can be found in Appendix G.

Many atomic peaks can be seen on top of the decaying background extinction. Figure 19c shows a zoom-in on the $5p^2\,{}^3P_2 - 5p6s\,{}^3P_2$ 284.06 nm atomic line for both target A1 and target A2. Target A2 is nearly identical to target A1; the only difference is the use of the line VP instead of the full VP. The data shows that the atomic line is very broad. The FWHM of the peak is approximately $25\,\mathrm{cm}^{-1}$ for target A1 and $\sim 13\,\mathrm{cm}^{-1}$ for target A2. The atomic line is in a high-extinction area, so optical depth broadening should not be neglected. Thus, the found width does not directly indicate the width of the underlying cross-section. The measured peak location is very close to the expected location of the peak, the difference being only 0.01 nm. This difference is within the precision of the wavelength calibration as discussed in Section 4 and thus determined to be insignificant. Last, Fig. 19c also shows a Gaussian fit to the experimental data. This fit shows that the atomic line is not fully Gaussian. A Gaussian shape is expected if the line is much narrower than the OPO bandwidth or if an inhomogeneous broadening mechanism is dominant. Figure 19c also shows that the atomic line seems to have a *tail* on the long wavelength side (284.20 to 284.40 nm), not present on the short wavelength side. Possible causes for this asymmetry will be discussed in Section 7.

Figure 19b shows an extinction spectrum of target A2, created with the line VP. As can be seen, the spectrum is less detailed, with fewer lines measured and no additional Mie scattering data points gathered. Regardless, the spectrum shows the same trends observed in Fig. 19a — decaying background extinction with atomic resonances on top. The overall extinction is also lower, as the column density is lower due to a lower overall vaporized mass. The atomic resonances are more pronounced due to the lower background. The relative strength between the atomic resonances is similar in Fig. 19a and b, indicating that the temperature is similar as the same ground states are populated.

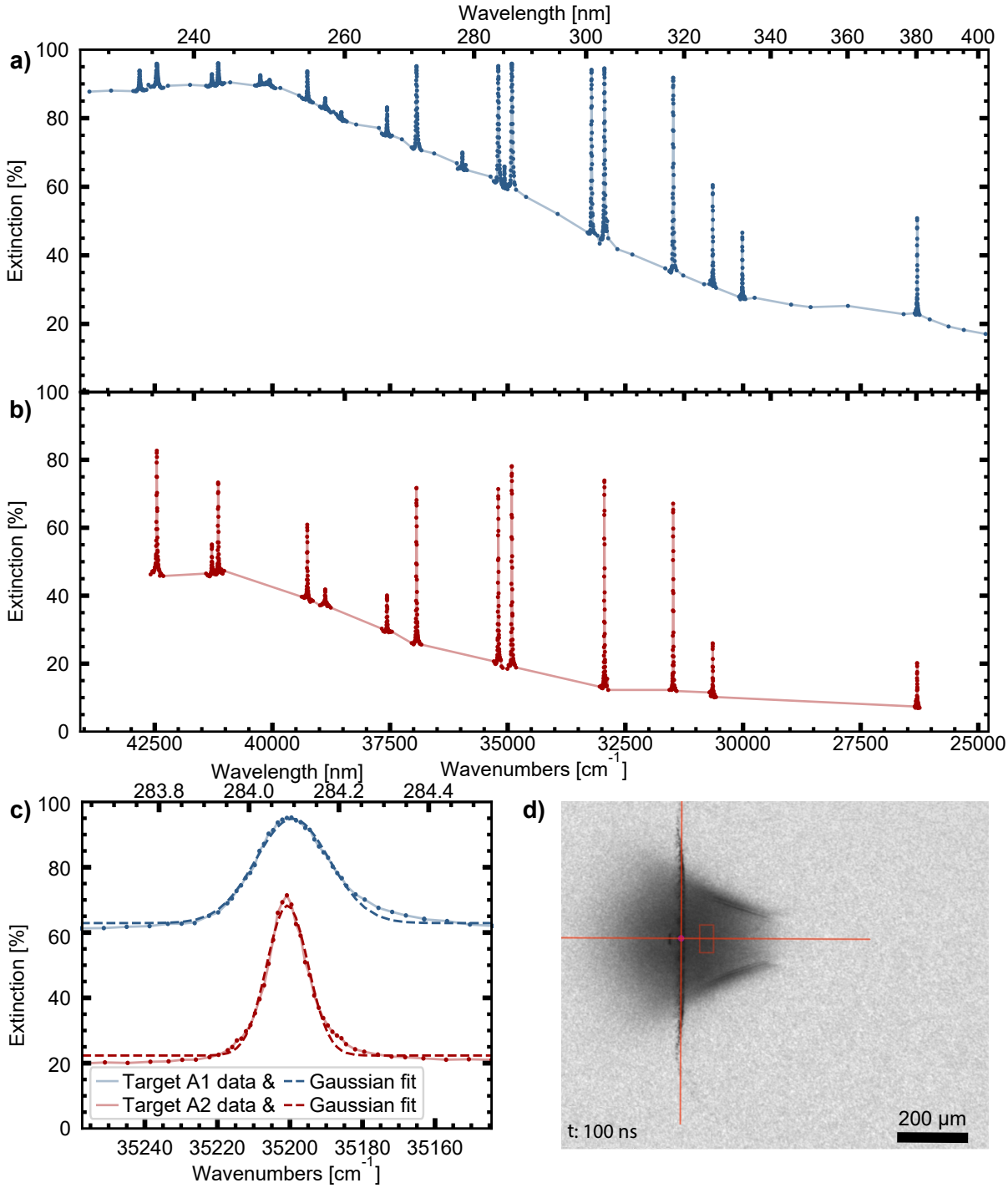

Figure 19: Panel a) shows the full experimental spectrum of target A1; the most detailed spectrum. See main text or Appendix G for target parameters. 21 atomic lines and extra Mie scattering data points between 227 and 403 nm. This target was created using the full VP and the images were taken 100 ns after the VP. Panel b) shows the experimental spectrum of target A2, which is identical except that the line VP is used instead of the full VP. Panel c) shows a zoom-in on the $5p^2\,{}^3P_0 - 5p6s\,{}^3P_1$ 284.06 nm atomic line for the data of target A1 (panel a) and target A2 (panel b). The atomic line is very broad and slightly asymmetric. Panel d) shows raw data of the vapor and the placement of the box used to make these spectra.

5.3 Extinction spectra for varying SP timing, spatial location, and targets

In this section, the fixed parameters in the spectra presented before will be varied. The parameters to be varied are the spatial location (*box*), the time between the VP and SP, and the target formation parameters (initial droplet size, PP energy, PP-VP delay). The influence of time on the found spectrum will be shown first. After, the spatial variation will be discussed by investigating different *boxes*. It will also be investigated how different targets (PP/VP settings) influence the spectra.

5.3.1 The influence of SP timing on the measured extinction

In this section, it will be shown what happens when the time between the VP and the SP is varied. The previously shown data was gathered 100 ns after the VP. Figure 20 shows the result of an atomic line scan with temporal resolution. A region of 0.6 nm around the $5p^2\,{}^3P_2 - 5p6s\,{}^3P_2$ 284.08 nm resonance is shown. This data was gathered for target A3, where the full VP was used. Target A1 and A3 are identical for all practical purposes (details in Appendix G).

Figure 20d shows the position of the two boxes of which extinction information is shown in the other subfigures. The left box is placed in front of the vapor. It will give information about the time evolution near the previously measured location. The right box is at the *focus* of the vapor, i.e., the point of maximum convergence, showing an extreme case.

Figure 20a shows a 'heat map' of time-resolved extinction in the left box (near the sheet). In these heat maps, the y-axis is a variable, in this case, the time between the VP and SP. The color indicates the found extinction, where darker is, intuitively, more extinction. The heat map shows that the extinction is initially low, as the vapor has not reached the box yet. The vapor enters the box at 60 ns, and the extinction increases quickly. After, a slow decline in extinction is visible. The peak also broadens; however, no other effects seem visible.

Figure 20b shows the same heat map, but now for the box at the focus created between 180 and 220 ns after the VP. The extinction is low until 140 ns after the VP when the vapor reaches the box. Then, the extinction increases massively, reaching higher values than obtained in the left box due to the focusing of the vapor. Afterward, the decay in extinction is visible again as the (column) density slowly decays as the vapor expands. The high density in the focus also causes an apparent density-related line shift, as visible by the peak location moving.

Figure 20c shows a 'line-out,' showing the evolution of the extinction at the peak center in time. Both the data from the left box and the right box are shown. The right box shows a near exponential decay, while the left shows a more complex decay profile.

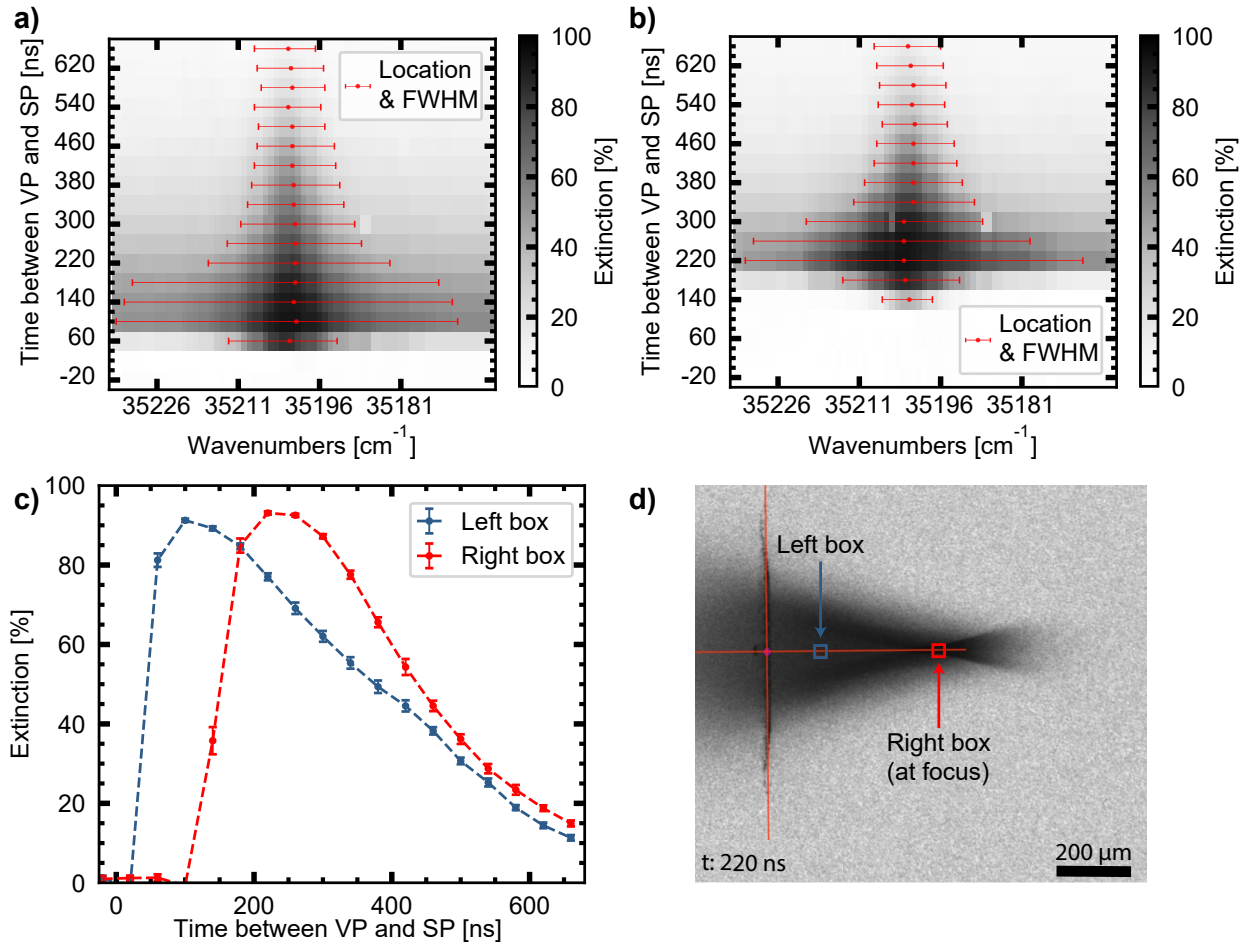

Figure 20: This image shows the influence of varying the time between VP and SP on the found extinction. This data is gathered for target A3, which is for all practical purposes identical to target A1. The scanned resonance is the $5p^2\,{}^3P_2 - 5p6s\,{}^3P_2$ 284.08 nm resonance. Panels a) and b) show a 'heat map,' where the time between VP and SP on the y-axis and the color indicates the extinction (darker is more extinction). The peak center and FWHM are also plotted. Panel a) shows the 'heat map' for the left box, and panel b) the 'heat map' for the right box. The placement of these boxes can be seen in d). Panel c) shows the found extinction at the center wavelength of the peak over time.

5.3.2 The influence of spatial location on the measured extinction

Target A1 will be used to show how the spatial location of a *box* influences the observed spectrum. Target A1 is also the target used to create the first spectrum shown in this thesis (see Fig. 19). A set of boxes, all with different spatial locations, are presented. Figure 21a shows the location of the presented *boxes*. The boxes are placed in a train on the horizontal centerline of the vapor. They are placed side by side and are 20 by 20 pixels. Thus, the only difference between the boxes is the distance to the sheet; the closest box is only ∼50 µm from the sheet, while the farthest is ∼700 µm away.

Figure 21c shows the full spectrum for a selected subset of the boxes. The boxes are indicated by their mean distance to the sheet. The image shows that the overall extinction decreases as the distance to the sheet increases. This decrease can be attributed to a lower overall (column) density further away from the sheet. Figure 21e shows all measured atomic resonances (more information about the resonances in Appendix A in more detail. This inset shows that denser regions with more overall extinction also have broader peaks.

Here, the *relative cross-section* is defined as

$$\sigma_{rel}(\nu) = -a \ln(1 - A(\nu)), \tag{23}$$

where A is the absorbed fraction and a is a scaling factor. The relative cross-section can be used to investigate the similarity of the spectra without being influenced by the different column densities. Comparing this definition to Eq. (2) shows that a is a scaling factor proportional to the column density in the vapor while σ_{rel} is proportional to σ. Both quantities do not have a unit since a is a fitting parameter, not the actual column density. The relative cross-section can show two things. First, it can show relative differences in the cross-section without having the difficult-to-interpret exponent of the Beer-Lambert law. Second, if the cross-section is similar, it can explain the relative difference in column density by comparing the scaling factor a. In practice, the scaling factors are calculated by picking one reference spectrum and fitting the other spectra to this spectrum. The a values of all other spectra are varied to produce the best fit. The resonances are not considered in the fitting procedure. This procedure means that the a values can give a relative column density of that spectrum compared to the reference spectrum. Finally, all spectra are divided by the maximum value in the reference spectrum for better visibility.

Figure 21d and f show the relative cross-section for the different spatial locations. Figure 21d is zoomed in on the y-axis to ensure visibility of the collapse of the Mie scattering background. Two things worth noting: First, the atomic peaks are stronger in low-density regions. Second, the Mie scattering background collapses to the same curve for all spatial locations. However, the low-density curves fluctuate more due to a lower overall extinction and thus higher noise influence.

Finally, Fig. 21b shows an extinction heat map, as shown before. A small range (0.5 nm) around the 317.60 nm resonance is shown. The y-axis shows different boxes, again indicated by their mean distance from the sheet. The color is the extinction found for that position from the sheet. The boxes close to the sheet show similar profiles around the resonance. This similar profile can be explained by looking at Fig. 21a; the vapor close to the sheet looks very similar around these boxes. The extinction spikes as the line of boxes reaches the focus, i.e., the point of convergence. The heat map shows this as higher overall extinction is found, and the peak also broadens. A shift in the peak is also observed as the center moves to the left. As the boxes pass over the focus and the vapor becomes divergent, the extinction drops quickly, and the line shift disappears.

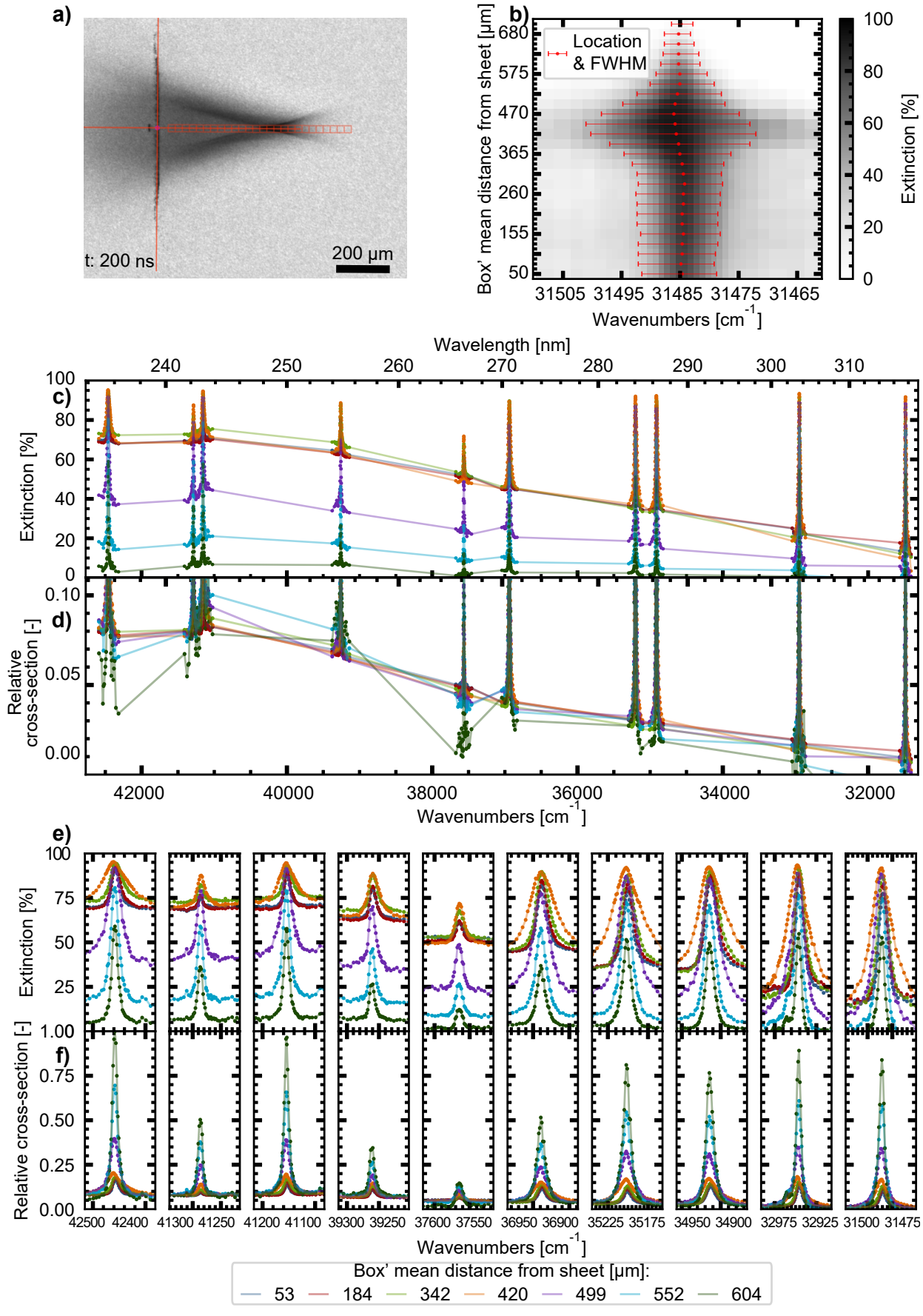

Figure 21: (Continued on the following page.)

Figure 21: This image shows the influence of varying the spatial location on the found extinction. Panel a) shows the location of the train of boxes used for this analysis. Panel b) shows a heat map of the extinction around the $5p^2\,{}^3P_2 - 5p6s\,{}^3P_1$ 317.60 nm resonance. The y-axis shows the distance to the sheet, while the color represents extinction. The FWHM and center positions of the peaks are also plotted. Panel c) shows the full extinction spectrum for some of these boxes. Panel d) shows a limited range of the relative cross-section to visualize the collapse of the Mie scattering background. The scaling factor a for the relative cross-section is found using a least-square fit. Only the Mie scattering data points are used in this fit, resulting in a collapse of the Mie scattering background. Panels e) and f) show all measured resonances in more detail, with panel e) showing the extinction and panel f) the relative cross-section. The resonances can be seen in more detail (including term symbols) in Appendix H.

5.3.3 The influence of the target settings on the measured extinction

In this section, it will be investigated how the extinction spectra differ between different targets. This will be done in two parts. First, two similar targets will be shown, and their extinction spectra will be compared. Second, three very different targets (for which only Mie scattering data points were gathered) will be shown and compared.

Figure 22 shows the extinction spectra of target A2 and target B. Target A2 has already been shown previously. Target B is created with the same initial droplet size and PP energy as target A2. The difference is that there is a shorter PP-VP delay. Regardless, the targets do have a similar radius. This relies on the fact that a sheet hit by the PP first expands, reaches an apex (maximum extension), and retracts. Thus, target B is timed to have a certain radius before the apex. Target A2 has a similar radius but after the apex. The target loses mass over time, causing target A2 to have a lower overall mass than target B due to its longer PP-VP delay.[26] This approach makes the mass, and thus the thickness, the main difference between the two targets. Figure 22a and b show target A2 and B imaged at the same wavelength and the box location used for the analysis. The VP energy is set to create a similarly sized vaporized slice as less energy is needed to vaporize the thinner sheet. This tweaking is done by checking the rear view green shadowgraphy. The vaporized slide of target B is around 75 µm, closely matching the vaporized slice of 80 µm of target A2.

The fact that target B has more mass in the sheet is immediately visible in Fig. 22c as the overall extinction of target B is higher than for target A2. Except for that, the extinction spectra of target A2 and target B look very similar. The inset Fig. 22d shows that the FWHM of the 317.60 nm resonance is slightly larger for target B. Except for that, only minor differences can be seen for the atomic resonances.

Figure 22e compares the relative cross-section of target A2 and target B as defined in Eq. (23). Like before, the relative cross-section is found by matching the Mie scattering component, not the atomic resonances. Figure 22e shows that the cross-section dependence on the wavelength of the two targets is very similar.

In most cases, the atomic peaks are slightly lower for target B, such as the 271, 284, 286, 303 and 317 nm resonances. This effect is visible in the inset Fig. 22f. In these cases, the FWHM of the peaks is also slightly larger, as mentioned, and can be seen in Fig. 22d.

The scaling factor, a, for target B is 0.53 times the scaling factor for target A2. This ratio indicates that target A's column density is just over half that of target B. This factor aligns very well with the results of Liu et al., who found that target B has twice the mass of target A2.[26]

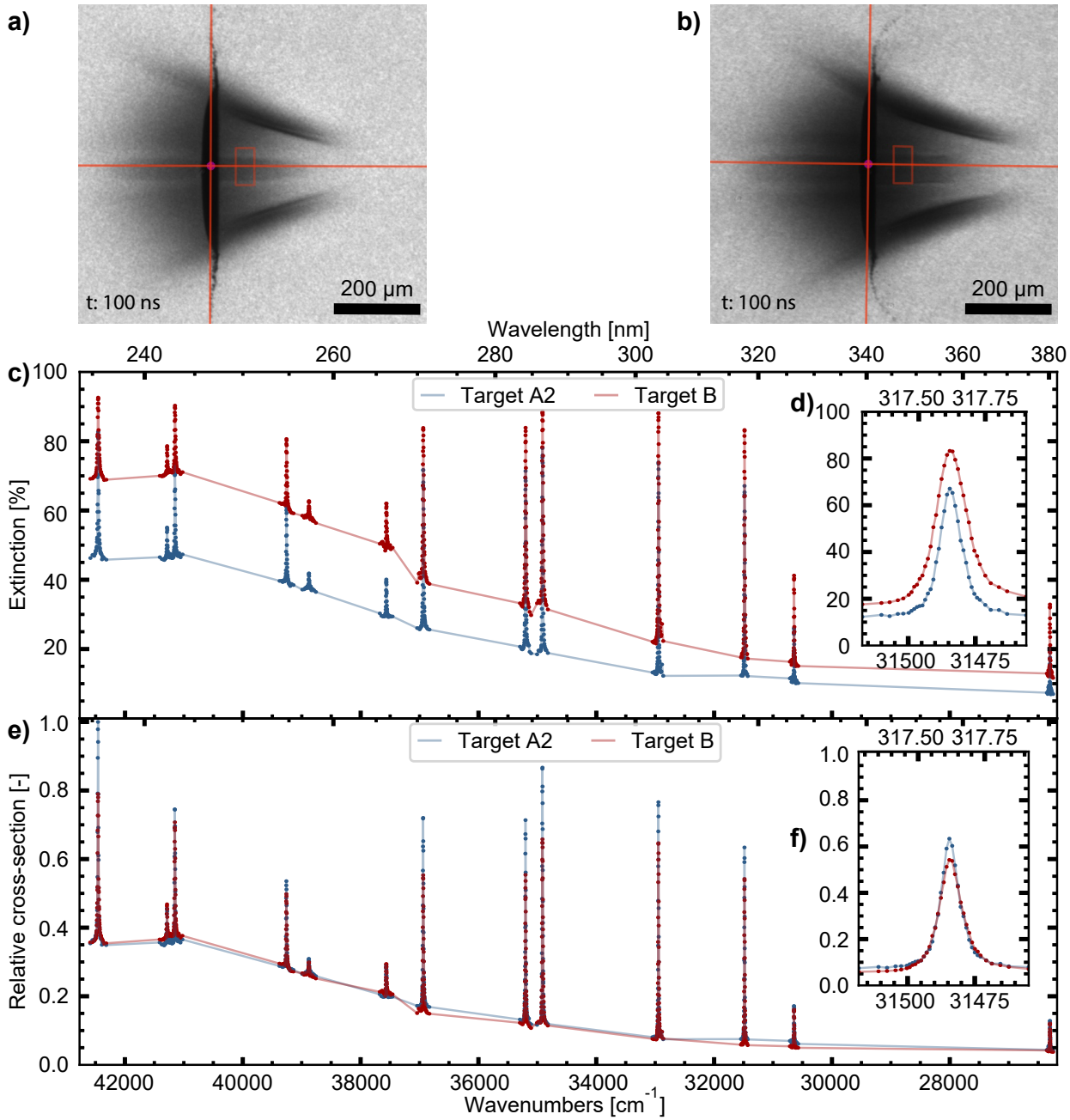

Figure 22: The spectra of two targets, target A2 (shown before) and target B. See the main text for the differences between the targets. No dedicated Mie scattering data points have been gathered. The decaying background is still visible by connecting the edges of the atomic lines. Panel a) shows target A2 imaged using UV shadowgraphy at 284.06 nm and the box location used in the analysis. Panel b) shows target B at the same conditions. Panel c) shows the extinction while the inset d) shows 0.6 nm around the $5p^2\,{}^3P_2 - 5p6s\,{}^3P_1$ 317.60 nm resonance. Panels e) and f) show the relative cross-section of targets A and B. The relative scaling factor to match B to A2 is 0.53. Panel f) shows that the relative cross-section for 0.6 nm around the 317.60 nm peak is lower for target B than for target A2.

Three more targets are also compared, for which only Mie scattering data points are gathered. The first of the three targets is target C. This target is made using a tiny initial droplet with a radius of only 17 µm (27 µm has been used until now for all targets). The PP and VP settings result in the thinnest target made during this thesis. The other two targets are targets D1 and D2; both made using the largest initial droplet radius possible of 36 µm. This results in the thickest target made during this thesis. A simple comparison of the initial radius shows that targets C and D have a tenfold difference in initial mass. The difference between target D1 and D2 is the VP energy. For target D1, the highest possible line VP energy is used. For target D2, the delay line is utilized, raising this VP energy limit. To recap Section 4, the delay line splits off a part of the pulse and lets the split-off part travel a longer path, effectively creating a double pulse and increasing the pulse length. Thus, the delay line allows higher VP energies to be used without creating plasma on the target, which would ruin the extinction measurements. A box in front of the sheet is used for all these targets. In short, target C is made using a tiny initial droplet and is very thin. Target D1 is made using a large initial droplet and is very thick. Target D2 has even more vaporized mass by utilizing the delay line. These targets, and the box location, can be seen in Fig. 23a to c. The extinction spectra of these targets can be seen in Fig. 23d.

The extinction spectra show the expected result: the more vaporized mass, the higher the overall extinction. To properly quantify the differences in the Mie scattering background, the *relative cross-section* is used again, shown in Fig. 23e. Figure 23e shows that targets D1 and D2 have the same relative cross-section, their curves matching closely. This can be explained by the fact that they have the same PP settings; D2 only has more vaporized mass. The scaling factor shows that target D1 has only 0.53 the column density of target D2. This scaling factor is expected as a larger slice of the sheet is vaporized; the VP energy for target D1 is 0.43 times the energy for target D2, showing a similar trend. Target C's relative cross-section looks different. The extinction decays quicker with wavelength than the target D counterparts. The onset of the decay in extinction is still in the same position for all targets, even in this case with extreme differences between the targets.

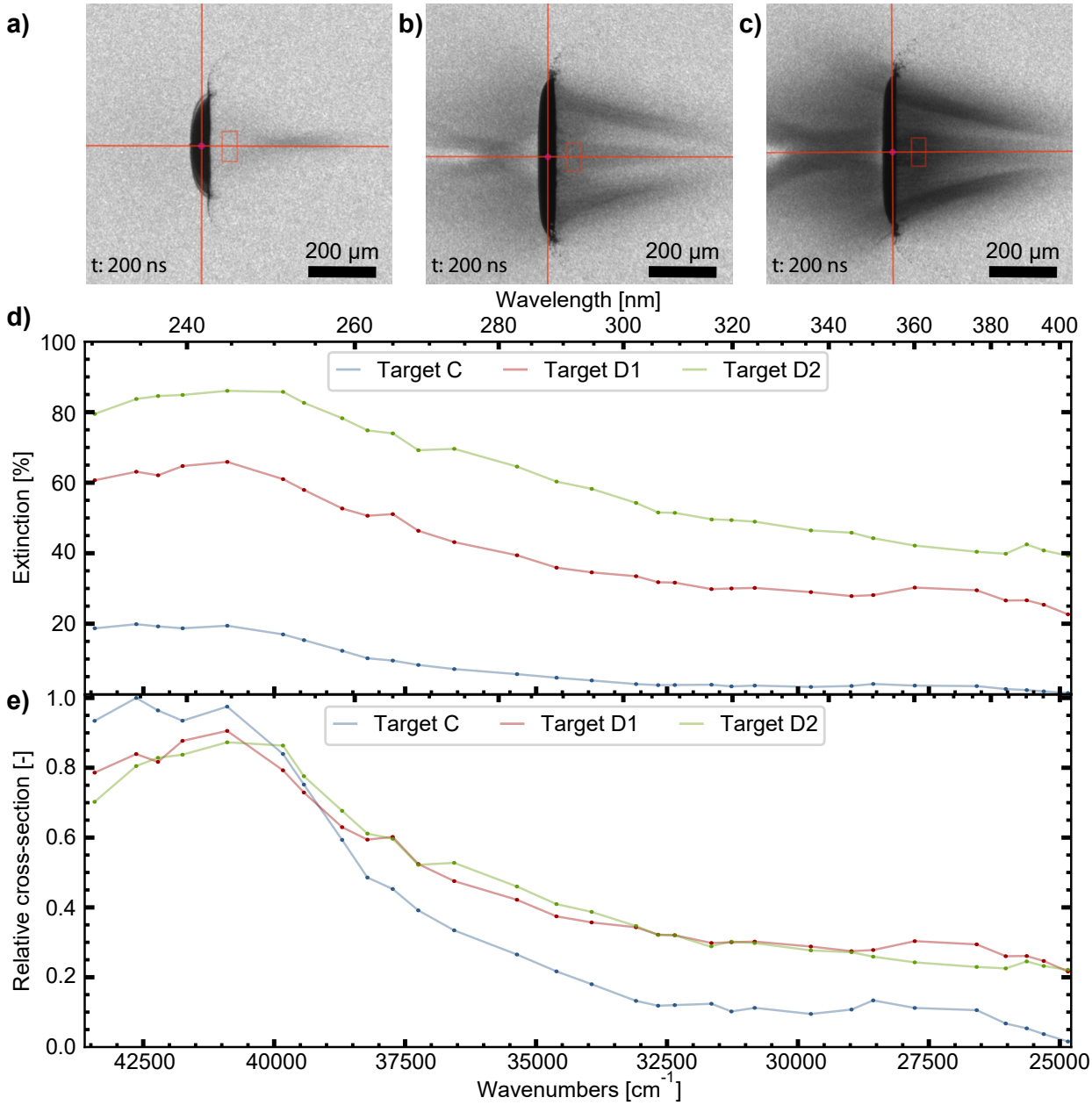

Figure 23: The extinction spectra of targets C, D1, and D2. See the main text for details about the targets. Target C can be seen in panel a), while targets D1 and D2 are in panels b) and c). These images are taken at 258 nm and also show the box location used. For these targets, only the Mie scattering spectrum is presented. Panel d) shows the extinction while e) shows the relative cross-section. The scaling factor for target C compared to target D1 is 5.36. The scaling factor for target D2 compared to target D1 is 0.53.

6 Matching the model to experimental data

In this section, the obtained experimental results will be combined with the created model to determine the physical properties of target A2. The extinction spectrum of target A2 can be seen in Fig. 19b. The matching is performed by least-squares fitting with the following free fit parameters: the nanodroplet size, the column density, the ratio between atoms and nanodroplets, and the temperature (the key parameters as introduced in Section 3). Matching the model to the experimental data is done in two steps, which are independent of each other. First, the Mie scattering background extinction is matched by changing the nanodroplet size and the column density. Second, the atomic resonances are matched by changing the atomic mass ratio (while keeping the column density for the nanodroplet constant) and the temperature. An additional free parameter for the atomic line matching is added: *additional broadening*. Introduced in Section 3, additional broadening adds a certain amount of Lorentzian broadening to the atomic resonances. The additional broadening is added to fit the impact of collisional broadening as this effect is not modeled. These two steps align with the first two subfigures of Fig. 24.

Target A2 is chosen as it is a line VP target. An advantage of the line VP is that the path length can be estimated using the rear view green shadowgraphy. From the rear view image, the vaporized slice of the sheet is visible to be approximately 80 µm wide. Thus, 80 µm is used as the path length. This path length has significant uncertainty, as the evolution of the width of the vaporized slice between the initial vaporization and when the images are made (100 ns after) is not yet known. This causes uncertainty in any estimated density.

Figure 24a shows the match of the Mie component of the spectrum. After removing the atomic resonances, the fit is obtained by matching the entire spectrum. The resonances are removed by ignoring data within 0.5 nm of the resonance. The found nanodroplet size is (25.6 ± 0.8) nm with a column density of $(1.9 \pm 0.1) \cdot 10^{18}\,\mathrm{m}^{-2}$. Assuming a path length of 80 nm (with no uncertainty) gives a density of $(2.3 \pm 0.1) \cdot 10^{24}\,\mathrm{m}^{-3}$. The obtained density is the density of atoms in liquid state; clustering $2.3 \cdot 10^{24}\,\mathrm{m}^{-3}$ atoms in 25.6 nm nanodroplets results in $9 \cdot 10^{17}$ nanodroplets/m^3. The found radius does not show a 'plateau' between 230 nm and 250 nm, where the extinction does not decrease yet. Except for that, the model can match the general trend of the extinction well. Two additional fits, where only the upper or lower half of the spectrum is used, are also shown to indicate a 'confidence bound.' The fit to the upper half finds a nanodroplet size of (9 ± 4) nm and a density of $(9 \pm 2) \cdot 10^{24}\,\mathrm{m}^{-3}$. The fit to the lower half results in a nanodroplet size of (21 ± 2) nm and a density of $(3.1 \pm 0.5) \cdot 10^{24}\,\mathrm{m}^{-3}$. None of the three fits are in good agreement with the experimental data, especially since none show the 'plateau.' The reduced chi-squared (χ^2_{red}) also indicates that the fit is poor, with a value of 5.54. The significant variance between the three fits shows that the actual uncertainty in the parameters related to Mie theory is quite significant. Still, it can be said that the nanodroplets are small (<35 nm), and the density is in the order of magnitude of $1 \cdot 10^{24}\,\mathrm{m}^{-3}$.

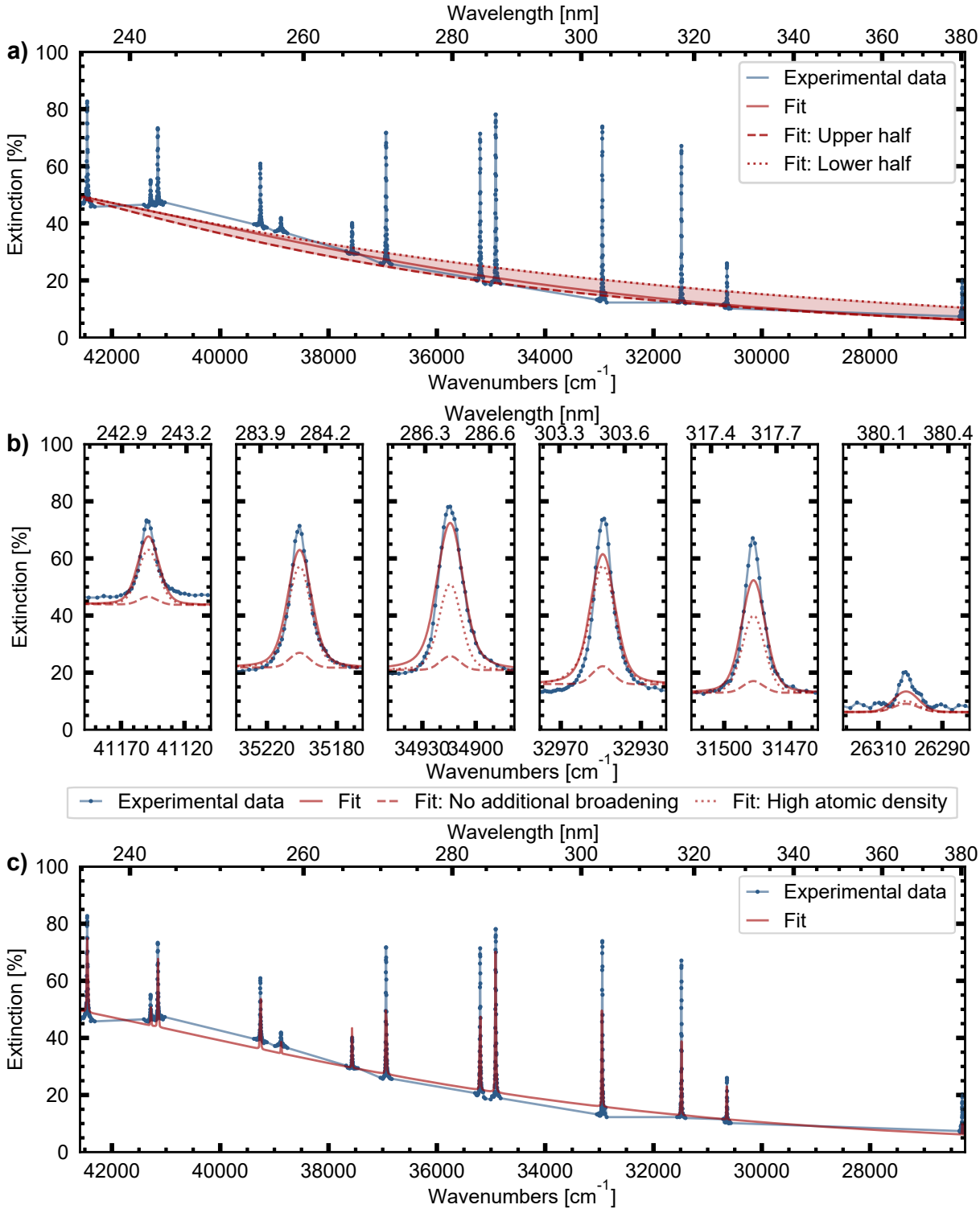

Figure 24: The procedure of matching the model to an experimental spectrum. Panel a) shows the first step: matching the Mie scattering background extinction. The upper and lower half fits are fitted to the spectrum's lower and upper half, respectively. The red area shows the uncertainty band caused by which part of the spectrum is used. Panel b) shows the matching procedure of the atomic resonances. The fit is obtained by fitting all atomic resonances in the spectrum. A fit without additional broadening is shown to visualize the requirement of additional broadening. A fit with extremely high atomic density is shown to visualize the interconnectedness of the parameters. Panel c) shows the final match. See main text for the resulting parameters.

Figure 24b shows the match of the atomic resonances in the spectrum. Only the 242, 284, 286, 303, 317 and 380 nm resonances are shown, but all resonances are used in the fit. The fit is obtained by removing the Mie scattering background and then matching the model to the data. In this case, the model is also used without Mie scattering, preventing any Mie scattering modeling errors from propagating into the atomic resonance match. The found parameters relating to the atomic resonances are: $(9 \pm 35)\,\%$ atomic mass ratio, a temperature of $(2140 \pm 75)\,\mathrm{K}$, and an additional broadening of $(0.1 \pm 0.5)\,\mathrm{cm}^{-1}$. While the model can predict the resonances' location and relative strength quite well, the overall fit is poor. The reduced chi-squared is 37.4, indicating a worse fit than for the Mie component. A fit without any additional broadening (keeping the other parameters constant) is also shown to visualize the impact of the additional broadening. It shows that the incorporated effects of natural and Doppler broadening cannot explain the full width of the experimental resonances. The lack of broadening leads to the model significantly underestimating the strength of the resonances as most of the laser light does not interact with the narrow resonance. The fitting procedure compensates for this by adding additional broadening. However, as the high atomic density fit shows in Fig. 24b, a 100x increase in the density of atoms can also increase the strength of the peaks. These two additional plots show that the uncertainty in the atomic mass ratio and additional broadening is significant due to their interconnectedness. Still, it can be said that the vapor has a low temperature (visible due to the limited strength of the $5p^2\,{}^1D_2 - 5p6s\,{}^3P_1$ 380 nm resonance) and that the density of the free atoms is $1 \cdot 10^{23}$ to $1 \cdot 10^{26}\,\mathrm{m}^{-3}$ depending on the actual broadening of the resonances.

Figure 24c shows the final match of the model to the experimental data of target A2. The model matches the overall trends in the measured spectra well. The Mie scattering component decays as the wavelength lengthens, and the atomic resonances of neutral tin can be measured as predicted. However, the slope in the background extinction decay is slower for the model than for the experimental data. Also, the strength of the atomic resonances is not matched for each resonance. These two factors lead to a reduced chi-squared of 22.7, indicating that the model does not currently capture the data correctly, even with additional broadening as an extra free parameter.

7 Summary & Discussion

The results from the experiments and the model match have been presented in the previous sections. A summary of these results will be given in this section. This summary will be followed by a more in-depth interpretation and explanation of the results. Suggestions for future work will follow next. A reflection on the goals of this thesis will be the final part of this section. The subgoals of the research question will also be discussed individually.

7.1 Summary

Raw images captured using the novel UV shadowgraphy were shown first in Section 5. The impact of the wavelength on the image and the line VP on the target was also shown. The extinction spectra of targets A1 and A2 were shown. These spectra showed a decrease in extinction due to Mie scattering for increasing wavelengths. The spectra also showed atomic resonances, proving the presence of both nanodroplets and atomic resonances in the vapor for the first time. A zoom-in on an atomic resonance was also shown, showing that the peaks are very broad and have some asymmetry. The novel metrology using UV shadowgraphy has not only been applied to one parameter set but also has been used to study the influences of varying the spatial location, the timing of the shadowgraphy, and the target formation. A decay of the extinction over time could be seen when varying the timing of the shadowgraphy. Investigating different spatial positions also showed variation in column density. An atomic line shift was observed in the high-density areas in the timing sweep and the spatial sweep. Two similar targets have been presented and matched each other well. A difference in column density of 0.53 was found between the two, aligning with the result of Liu et al.[26] Three different Mie scattering spectra have also been presented. These showed an onset in the decay of the background extinction at the same wavelength range (around 250 nm). However, the extinction decays quicker over wavelength for target C than for the other targets.

A model was also created to predict and explain the spectra. The model was matched to a spectrum of target A2, resulting in the physical properties of the vapor (at a specific location). First, the nanodroplet size of (25.6 ± 0.8) nm and the column density of $(1.9 \pm 0.1) \cdot 10^{18}$ m^{-2} atoms in a liquid state was obtained by matching the Mie component. The line VP allowed the conversion of the column density into a density, giving a value of $(2.3 \pm 0.1) \cdot 10^{24}$ m^{-3} or $\sim 9 \cdot 10^{17}$ nanodroplets/m^3. The model was also matched to the atomic resonances, resulting in an atomized mass ratio of (9 ± 35) % and a temperature of (2140 ± 75) K. An additional broadening value, broadening not predicted by the model, of (0.1 ± 0.5) cm^{-1} was required for this fit. While the model correctly predicts the general trends in the spectra, it cannot exactly match the width of the atomic resonances nor the slope of the background extinction decay due to Mie scattering.

7.2 Discussion of results related to Mie scattering

The discussion of the obtained results will be split into two parts. The Mie scattering component of the spectrum will be discussed in this section, with the atomic resonances following in the next section.

The background due to Mie scattering is visible in the spectra of all presented targets, proving the presence of nanodroplets in the vapor. All spectra showed a similar profile: a plateau below 250 nm, followed by a decay in extinction as the wavelength lengthens. This location of the onset of the decay indicates a nanodroplet size between 25 to 35 nm. The measured profiles are surprisingly similar, considering the major differences between the targets and the spatial locations probed. For example, the plateau below 250 nm is present in all the spectra. Nearly all the Mie spectra collapse to one curve when using the relative cross-section, showing invariance to space and time. The only

difference noted is in Fig. 23, which showed that the background decays steeper for target C than for target D.

The model is matched to the experimental spectra to determine a nanodroplet size and a (column) density. A nanodroplet radius of (25.6 ± 0.8) nm is determined with a column density of $(1.9 \pm 0.1) \cdot 10^{18}\,\mathrm{m}^{-2}$. With the predicted 80 µm path length, this leads to a density estimate of $(2.3 \pm 0.1) \cdot 10^{24}\,\mathrm{m}^{-3}$, which is equal to $9 \cdot 10^{17}$ nanodroplets/m^3. There is some uncertainty in the column density, as different cross-sections for different nanodroplet sizes would impact this estimate. However, the largest uncertainty is in the overall density since the path length is not accurately measured. The match between the Mie component of the model and experimental data is not yet sufficiently accurate, causing considerable uncertainty in the extracted parameters. The clearest mismatch is that the found nanodroplet size cannot reproduce the plateau in extinction below 250 nm. The following decay in extinction is also steeper in the experimental data than in the model. No size parameter can reproduce the slope seen in the experimental data, even when disregarding the visible plateau in all spectra below 250 nm. The complex refractive index can change the slope of the Mie background. Currently, the model uses data from Cisneros et al.,[60] who provide the refractive index of liquid tin at different temperatures between 310 nm and 12 µm. However, none of the refractive index values provided allow the model to match the experimentally observed slope. Further research is needed to separately benchmark the model, such as an investigation into the refractive index of the nanodroplets of tin in the deep UV (below 310 nm) to see if the current extrapolation is valid. The components of the experimental setup should also be validated to ensure that neither the imaging nor any other setup component shows any wavelength dependence. Options here are the camera's quantum efficiency, scattering or fluorescence on optics, or effects related to the moving of the imaging lens. The linearity of the camera counts also has to be quantified.

It is not understood how the slope can be steeper for one target than for the other while keeping the plateau below 250 nm as seen in Fig. 23. Changing the nanodroplet size cannot directly explain a quicker decay in the same wavelength regime. Influencing parameters of the decay rate are the

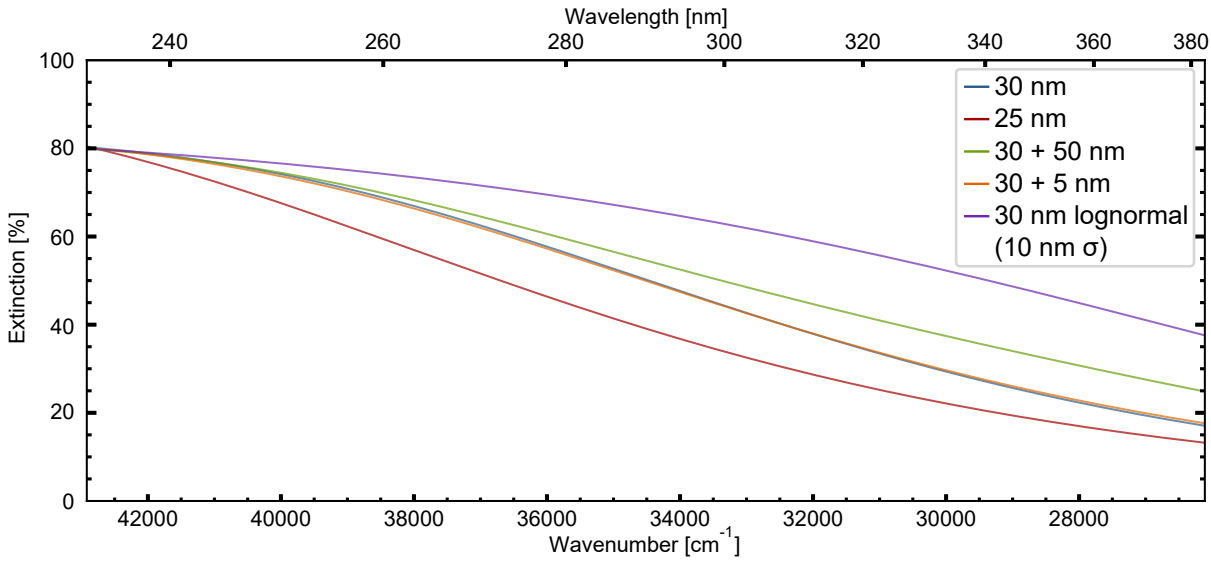

Figure 25: The extinction spectrum of five different nanodroplet distributions. Densities are tuned to ensure that all start at 80 % extinction at the shortest wavelength. The green and orange lines show 30 nm with either a smaller or larger nanodroplet added to the distribution. The purple line is a lognormal distribution with a mean of 30 nm and a standard deviation of 10 nm.

refractive index, temperature (which changes the refractive index), and surrounding density (which can also change the relative refractive index). None of these have been tested or proven in this thesis. Figure 25 shows that a superposition of nanodroplet sizes does not make the decay in the background steeper than one single nanodroplet size. Only 25 nm shows a steeper decay than 30 nm but does not show the desired plateau below 250 nm.

The physical process determining the nanodroplet size, the critical parameter in the Mie scattering component, is not yet understood. One of the hypotheses was that the sheet thickness would influence this parameter. However, even with very different sheet thicknesses, the nanodroplet size did not change as the plateau did not move. A hypothesis for the nanodroplet size is that the nanodroplets do not absorb enough energy to become smaller nanodroplets. This energy would be needed to vaporize more mass or overcome surface tension. However, Mie theory calculations show that nanodroplets still absorb the 1 µm VP laser light at these radii, so this also cannot be the cause. Thus, further research is needed to determine what physical process sets the nanodroplet size (distribution).

7.3 Discussion of results related to atomic resonances

Many atomic resonances have been measured and shown in Section 5, proving the presence of free atoms in the vapor. In general, the atomic resonances of neutral tin could be measured as expected; the atoms were present in every measured spectrum. The atomic resonances are broad and skewed, with a tail on the high wavelength side. This shape can be best seen in Fig. 19c or Fig. 22b.

Part of the broadening can be explained by optical depth broadening; the high column density causes the visible width to increase due to the exponent in the Beer-Lambert law. Figure 21 also showed that a line shift is observed at high densities in the vapor's point-of-convergence. At the same time, Fig. 22 showed that the atomic resonances are weaker for the higher density target B (when comparing the relative cross-section). This weakening and shifting in high-density areas indicate that density broadens (thus weakens) and shifts the resonances. A density-related shift can be in both directions in the spectral range. Density-related line shifts also often come with asymmetry and thus can explain (a part of) the asymmetry seen in the presented spectra.[52] As the OPO bandwidth is broad, the laser spectral profile must be known in detail to deconvolve the cross-section shape from the extinction spectrum. Since this has not been done for this thesis, it cannot be concluded in detail how significant the impact of density-related effects is on the line shape (including the observed asymmetry) of the resonances. Still, the shift and weakening observed in the experimental data prove that density-related effects are essential to the measured spectra.

The model is matched to the atomic resonances and accurately predicts their location. The match results in an atomic mass ratio of $(9 \pm 35)\,\%$, which equals a column density of $\sim 1 \cdot 10^{17}\,\mathrm{m}^{-2}$ or $1 \cdot 10^{23}\,\mathrm{m}^{-3}$ when assuming a 80 µm path length. However, the model can not reproduce the width and strength of the atomic resonances. As mentioned in Section 3, collisional broadening is not modeled as the required cross-sections are unavailable. However, it was expected, and Fig. 20 and 21 proved that collisional broadening and shifts are occurring in the vapor. An additional broadening value is fitted during the model match to compensate for the lack of collisional broadening modeling. This value is found to be $(0.1 \pm 0.5)\,\mathrm{cm}^{-1}$. This value is uncertain due to its interconnectedness with the atomic mass ratio. According to Romalis et al., a density of $\sim 4 \cdot 10^{24}\,\mathrm{m}^{-3}$ is required for $0.1\,\mathrm{cm}^{-1}$ collisional broadening[52] while Eq. (14) predicts that only $\sim 2 \cdot 10^{23}\,\mathrm{m}^{-3}$ is required (when assuming a cross-section of $1 \cdot 10^{-16}\,\mathrm{m}^{-2}$). All in all, the found density is in the correct order of magnitude to show collisional effects according to the literature. Thus, collisional broadening has to be researched in more detail to find the exact mechanism at work in the vapor. This will allow implementation into the model to match the observed width better.

Saturation broadening has also been tested experimentally to investigate whether it is a relevant component. This test measured extinction spectra at different intensities of shadowgraphy light. The shadowgraphy intensity was changed two orders of magnitude. Still, no significant difference between the spectra was observed; hence, saturation broadening is not a significant effect. More details can be found in Appendix I.

A temperature of (2140 ± 75) K was used in the model matching. This temperature results in the best match as a low temperature reduces the strength of some resonances such as the 242, 326 and 380 nm transitions. However, this temperature is below the boiling temperature of tin at ambient pressure (2875 K) and thus considered low.[53] A more detailed temperature measurement can be done to get a more accurate value for the temperature. This more detailed estimation can be done by making a Boltzmann plot, where the strengths of atomic resonances are plotted against the energy level of their ground states. From this, the temperature can be obtained. However, to do this, a more narrow-band laser would be preferred to allow one to measure the cross-section profile of the resonances. In the current setup, the spectral bandwidth of the OPO obscures the cross-section profile. Thus, temperature estimation from the extinction spectra is future work.

The observed spectra do not show the broad extinction spectra with continuously increasing extinction as the wavelength shortens characteristic to clusters of atoms,[39,40] as the plateau below 250 nm is visible. This indicates that clusters are not a dominant species in the tin vapor. Hence, the decision not to model clusters is still valid.

7.4 Future work

The discussion above already mentioned several options for future work. In this section, the possible avenues for future research will be summarized, including their reasoning and added value. This summary will be split into the experimental setup and the model.

The possible improvements to the experimental setup are listed below, including their reasoning. They are ordered with the improvements costing the most time and money coming last.

- The offset in the output wavelength of the OPO can be removed by re-calibration. This re-calibration can reduce the system's complexity by eliminating the confusing 'output' wavelength.
- The spectral bandwidth of the OPO can be investigated further using the SCT320 spectrometer. This investigation could explain part of the observed asymmetry in the atomic resonances.
- The wavelength-dependence of all the components in the UV shadowgraphy and the linearity of the pco.ultraviolet camera can be quantified. This can help in finding out why the decay of the Mie scattering component differs between targets.
- A different or shorter fiber could be used to further increase the measurable UV range to the full range of the OPO (192 to 400 nm). An extended range would be a good addition for further Mie scattering work, as it could confirm the measured plateau in extinction. The extra range would also be helpful if the nanodroplet size changes at some point, as it would increase the chances of measuring a plateau followed by a decay in extinction.
- UV shadowgraphy at 30° could be added. The OPO beam (before entering the fiber) is large enough to couple into two fibers; thus, only another imaging setup plus a camera is needed. This 30° view would allow one to study the dynamics of the vapor in more detail. It would also allow one to better estimate the path length and, thus, the density.

Two options for large-scale new diagnostics to give more information about the vapor and its dynamics are proposed. The first new diagnostic is to add a different laser as vaporization pulse.

A laser that allows for more and longer temporal profiles would allow for an investigation of the vaporization dynamics. For example, a 100 ns vaporization pulse would allow for imaging the vapor during the vaporization pulse. This information could help understand why the vapor forms the observed shape and why the measured composition is formed. The second is to add a dye laser in addition to the OPO. This laser would have reduced scanning range (depending on the precise laser and dye). However, dye lasers usually have a significantly lower spectral bandwidth, with values below $0.01\,\mathrm{cm}^{-1}$ not uncommon. Such a dye laser in a suitable range (for example, 265 to 287 nm) would allow a more detailed investigation of the atomic line shape and the determination of the temperature of the vapor.

The model can also be extended in two key ways. The first is to include collisional broadening effects into the model. The current iteration of the model allows the density of experimental data to be determined. Broad and shifted atomic resonances with some asymmetry have also been found experimentally. The found density values can be combined with the found widths, shifts, and asymmetries to better understand the exact collisional broadening mechanism. This new understanding of collisional broadening could allow for its implementation into the model. The second extension of the model relates to the decay in the background extinction. While the general shape can be reproduced, the experimental data shows a steeper decay than the model. Further research is needed to determine what is causing the steeper than predicted decay. The primary hypothesis is that it has to do with the extrapolation of refractive index data below 310 nm; thus, additional literature must be studied. Ensuring that the model can match the steep decay in the background will allow for the next step in determining the physical properties of the tin vapor.

7.5 Reflection on the research question

The research question and its four subgoals will be reflected upon to finalize this thesis. First, the subgoals of the experimental setup and the model will be evaluated for their success. The overall research question is re-examined afterward, including a critical assessment will be done on whether it has been answered.

7.5.1 Subgoals

Two of the subgoals were to implement UV shadowgraphy into the existing Dalek-II setup and to use it to measure extinction spectra. In short, both these goals have been very successful. The OPO laser has been implemented into the setup. Its temporal and spectral behavior have been quantified and calibrated. The SCT320 spectrometer has been added to the setup to validate its performance. The entire UV regime of the OPO was used in the experiments, excluding the part that is not transmitted by the fiber. The experiments have also been completed, as seen in Section 5. Thus, while improvements to the Dalek-II setup are always possible (see Section 7.4), the subgoals related to the experimental setup have been met very successfully.

Two subgoals appertained to the model; the first was to develop it, and the second was to match it to the experimental data. On the one hand, a model has been developed from scratch to predict extinction (spectra) in great detail and matches the general trends observed in the experimental spectra. However, the model does not yield a perfect match, as it cannot explain the steepness of the observed decay in the extinction of the background and the width of the atomic peaks. This mismatch leaves a considerable uncertainty in any physical properties that could be extracted from a spectrum by matching the model. In short, a model that incorporated atomic absorption and Mie scattering has been successfully developed. The model can match the general trends observed in the experimental spectra. However, it does not yet sufficiently accurately match the experimental results.

7.5.2 Research question

The first part of the research question is to find the composition of tin vapor used in the EUV light creation process. This part of the research question has been very successful. It has been found that nanodroplets and atoms are present in the vapor as their components are visible in the extinction spectra. There are still options for future work, as the model made to explain the spectra does not match the experimental data sufficiently well. The implementation of UV shadowgraphy has also led to several other new avenues for research, as discussed in Section 7.4.

The second part of the research question is to find the factors that influence the composition. To answer this, temporal and spatially resolved spectra have been made. Different targets have also been investigated. Very little difference in the extinction spectra has been observed as these parameters were varied. Thus, implementing the novel diagnostic has excluded some factors from influencing the composition. However, finding the parameters that do influence the composition is still future work.

To conclude, the work presented in this thesis has answered the research question partially. A novel methodology to measure the composition has been presented, and a model to explain the spectra has been developed. However, several unexplained factors exist, such as background decay and the width of atomic resonances. Future work, which can be built upon the robust platform created during this project, is required before a definitive answer to the research question can be given.

7.5.3 Impact on the larger fields of EUV lithography and nuclear fusion

One can also reflect upon what the conclusions of this thesis mean for the larger question posed in the introduction: "How to absorb the main pulse efficiently and generate as much EUV light as possible while extending life- and uptime?" No relation to CE was made at any point in this thesis, nor was research done on this. However, new hypotheses can be made based on the presented measurements. First, the induced vaporization may harm the life- and uptime of the EUV source. The vaporization causes the tin to go everywhere in the device, more so than with only a pre-pulse. Especially the laser side is coated with tin significantly more for a vaporization pulse experiment than for a pre-pulse only experiment. Since this laser side is the side of the collection mirror, this could negatively affect the lifetime of the mirror.

The induced vaporization will also directly influence the main pulse, specifically the absorption of the main pulse. Increasing the absorption efficiency of the main pulse will directly increase the CE, as it allows one to reduce the main pulse energy without reducing the absorbed energy. A pre-pulse target appears to the main pulse like a mirror due to its flat profile and high density in the liquid state. Contrary to this, the vaporized target has a significantly lower density. Its extended cone-like shape could also help with the absorption of the main pulse as it allows for a longer absorption path length, and its shallow angles might allow for internal reflection. Of course, significantly more work is needed to properly quantify the complex influence of the vaporization pulse on the performance of the EUV source. However, a good start has been created for future work on this topic.

UV shadowgraphy is a valuable metrology tool, as shown in this thesis. A similar implementation could also be set up for nuclear fusion research to show the composition of tin vapor in liquid-tin divertors. In this case, challenges would be obtaining an acceptable resolution (since most fusion devices are larger than the Dalek-II chamber) and filtering out the plasma light from the fusion reaction. Still, these technical challenges should be solvable, opening up options for UV shadowgraphy for nuclear fusion based upon the methods presented in this thesis.

8 Conclusion

This thesis was written to answer the research question: "What is the composition of tin vapor targets used in the EUV light creation process, and which factors influence this composition?" Four subgoals were set out and executed to answer this question. The first subgoal is a success as the existing *Dalek-II* experimental setup was improved by adding UV shadowgraphy. UV shadowgraphy ranges from ∼225 to 405 nm, allowing the creation of detailed extinction spectra. An OPO laser is used as the UV light source and is calibrated extensively. A spectrometer is set up to check the output of the OPO. The required measurements using UV shadowgraphy were automated using a self-developed Python package `OPOcontrol`. The second subgoal, to measure extinction spectra, is also completed successfully. Detailed scans have been performed using the setup in a short time, partly due to the high level of automation. These novel measurements showed the presence of atoms and nanodroplets in the vapor for the first time, proven by their distinct components in the extinction spectra. Spectra have also been presented for different targets, spatial locations, and timings. All spectra showed similar profiles with decaying background extinction due to Mie scattering and atomic resonances.

The third subgoal was to create a model to explain the measured spectra. This subgoal aligns with the last goal to match the model to the experimental data. These goals were partly successful as an extensive model was created that can predict the general trend of the spectra. However, the model cannot fully explain the measured spectra as the modeled width and strength of the atomic resonances and the decay in the background extinction level do not match the experimental data. The resonances are wider and stronger than modeled, and the decay in extinction is quicker than expected. In short, the research question has been partly answered. While novel measurements and new versatile metrology have been presented that show the details of the tin vapor for the first time, the measured spectra cannot be fully explained yet.

A perfect match between the model and experiments is left to future work. Density-related broadening is proposed as a future research topic to explain the width of the atomic resonances. Further literature research into tin's refractive index below 310 nm can help better understand the Mie scattering component. A new laser with longer pulse lengths would help gain insight into the vaporization dynamics to explain why this composition is found.

9 Acknowledgments

First, I would like to thank the entire EUV Plasma Processes group. From group leaders to Ph.D. candidates and technicians, the entire group was always very friendly and helpful. The pleasant atmosphere within the group is one of the reasons I enjoyed my thesis so much. I also want to thank Randy, Oscar, and Niek for their excellent supervision. I really enjoyed the productive, honest, and fun cooperation. Finally, I want to thank two people from my personal life. First, I want to thank Pascal, who always listened to my cathartic rants whenever I needed to have one. Last but not least, I want to thank my girlfriend, Tanya. She always supported me during the entire project, even though I would sometimes leave her behind for three weeks to shoot lasers at tin.

10 References

[1] NJ Lopes Cardozo, AGG Lange and GJ Kramer. 'Fusion: expensive and taking forever?' In: *Journal of fusion energy* 35.1 (2016), pp. 94–101.

[2] NJ Lopes Cardozo. 'Economic aspects of the deployment of fusion energy: the valley of death and the innovation cycle'. In: *Philosophical Transactions of the Royal Society A* 377.2141 (2019), p. 20170444.

[3] Gordon E Moore. 'Progress in digital integrated electronics'. In: vol. 21. Washington, DC, 1975, pp. 11–13.

[4] M Mitchell Waldrop. 'The chips are down for Moore's law'. In: *Nature News* 530 (7589 2016), p. 144.

[5] Arie J. Den Boef. 'Optical wafer metrology sensors for process-robust CD and overlay control in semiconductor device manufacturing'. In: *Surface Topography: Metrology and Properties* 4 (2 Feb. 2016), p. 023001. ISSN: 2051-672X. DOI: 10.1088/2051-672X/4/2/023001. URL: https://iopscience.iop.org/article/10.1088/2051-672X/4/2/023001%20https://iopscience.iop.org/article/10.1088/2051-672X/4/2/023001/meta.

[6] Jan van Schoot et al. 'The future of EUV lithography: continuing Moore's Law into the next decade'. In: vol. 10583. International Society for Optics and Photonics, 2018, 105830R.

[7] R Fabian Pease and Stephen Y Chou. 'Lithography and other patterning techniques for future electronics'. In: *Proceedings of the IEEE* 96 (2 2008), pp. 248–270. ISSN: 0018-9219.

[8] Wikipedia contributors. *Photolithography — Wikipedia, The Free Encyclopedia*. [Online; accessed 1-November-2021]. 2021. URL: https://en.wikipedia.org/w/index.php?title=Photolithography&oldid=1052392357.

[9] R. P. Seisyan. 'Nanolithography in microelectronics: A review'. In: *Technical Physics 2011 56:8* 56 (8 Aug. 2011), pp. 1061–1073. ISSN: 1090-6525. DOI: 10.1134/S1063784211080214. URL: https://link.springer.com/article/10.1134/S1063784211080214.

[10] Christian Wagner and Noreen Harned. 'Lithography gets extreme'. In: *Nature Photonics* 4 (1 2010), pp. 24–26. ISSN: 1749-4893.

[11] Oscar O. Versolato. 'Physics of laser-driven tin plasma sources of EUV radiation for nanolithography'. In: *Plasma Sources Science and Technology* 28 (8 Aug. 2019). ISSN: 13616595. DOI: 10.1088/1361-6595/ab3302. URL: https://iopscience.iop.org/article/10.1088/1361-6595/ab3302/meta.

[12] Duane Hudgins and Reza S. Abhari. 'Rupture time of droplets impacted by a burst of picosecond laser pulses'. In: *Physical Review E* 99 (3 Mar. 2019), p. 031102. ISSN: 24700053. DOI: 10.1103/PHYSREVE.99.031102/FIGURES/6/MEDIUM. URL: https://journals.aps.org/pre/abstract/10.1103/PhysRevE.99.031102.

[13] Sten A. Reijers, Jacco H. Snoeijer and Hanneke Gelderblom. 'Droplet deformation by short laser-induced pressure pulses'. In: *Journal of Fluid Mechanics* 828 (Oct. 2017), pp. 374–394. ISSN: 0022-1120. DOI: 10.1017/JFM.2017.518. URL: https://www.cambridge.org/core/journals/journal-of-fluid-mechanics/article/abs/droplet-deformation-by-short-laserinduced-pressure-pulses/F737817FC793C1B3B3DF3951F8BD75FD.

[14] Aneta S. Stodolna et al. 'Controlling ion kinetic energy distributions in laser produced plasma sources by means of a picosecond pulse pair'. In: *Journal of Applied Physics* 124 (5 Aug. 2018), p. 053303. ISSN: 0021-8979. DOI: 10.1063/1.5033541. URL: https://aip.scitation.org/doi/abs/10.1063/1.5033541.

[15] S. Yu Grigoryev et al. 'Expansion and Fragmentation of a Liquid-Metal Droplet by a Short Laser Pulse'. In: *Physical Review Applied* 10 (6 Dec. 2018), p. 064009. ISSN: 23317019. DOI: 10.1103/PHYSREVAPPLIED.10.064009/FIGURES/11/MEDIUM. URL: https://journals.aps.org/prapplied/abstract/10.1103/PhysRevApplied.10.064009.

[16] M. M. Basko et al. 'Fragmentation dynamics of liquid–metal droplets under ultra-short laser pulses'. In: *Laser Physics Letters* 14 (3 Jan. 2017), p. 036001. ISSN: 1612-202X. DOI: 10.1088/1612-202X/AA539B. URL: https://iopscience.iop.org/article/10.1088/1612-202X/aa539b%20https://iopscience.iop.org/article/10.1088/1612-202X/aa539b/meta.

[17] M. S. Krivokorytov et al. 'Shaping and Controlled Fragmentation of Liquid Metal Droplets through Cavitation'. In: *Scientific Reports 2018 8:1* 8 (1 Jan. 2018), pp. 1–6. ISSN: 2045-2322. DOI: 10.1038/s41598-017-19140-w. URL: https://www.nature.com/articles/s41598-017-19140-w.

[18] Dmitry Kurilovich et al. 'Power-law scaling of plasma pressure on laser-ablated tin micro-droplets'. In: *Physics of Plasmas* 25 (1 Jan. 2018).
, p. 012709. ISSN: 1070-664X. DOI: 10.1063/1.5010899. URL: https://aip.scitation.org/doi/abs/10.1063/1.5010899.

[19] M. S. Krivokorytov et al. 'Cavitation and spallation in liquid metal droplets produced by subpicosecond pulsed laser radiation'. In: *Physical Review E* 95 (3 Mar. 2017), p. 031101. ISSN: 24700053. DOI: 10.1103/PHYSREVE.95.031101/FIGURES/5/MEDIUM. URL: https://journals.aps.org/pre/abstract/10.1103/PhysRevE.95.031101.

[20] Alexander L. Klein et al. 'Drop Shaping by Laser-Pulse Impact'. In: *Physical Review Applied* 3 (4 Apr. 2015), p. 044018. ISSN: 23317019. DOI: 10.1103/PHYSREVAPPLIED.3.044018/FIGURES/6/MEDIUM. URL: https://journals.aps.org/prapplied/abstract/10.1103/PhysRevApplied.3.044018.

[21] Hanneke Gelderblom et al. 'Drop deformation by laser-pulse impact'. In: *Journal of Fluid Mechanics* 794 (May 2016), pp. 676–699. ISSN: 0022-1120. DOI: 10.1017/JFM.2016.182. URL: https://www.cambridge.org/core/journals/journal-of-fluid-mechanics/article/abs/drop-deformation-by-laserpulse-impact/A45F30CA4E410A5194AE3CE40D346F78.

[22] Dmitry Kurilovich et al. 'Plasma Propulsion of a Metallic Microdroplet and its Deformation upon Laser Impact'. In: *Physical Review Applied* 6 (1 July 2016). ISSN: 23317019. DOI: 10.1103/PhysRevApplied.6.014018. URL: https://journals.aps.org/prapplied/abstract/10.1103/PhysRevApplied.6.014018.

[23] Alexander L. Klein et al. 'Drop fragmentation by laser-pulse impact'. In: *Journal of Fluid Mechanics* 893 (2020), p. 7. ISSN: 0022-1120. DOI: 10.1017/JFM.2020.197. URL: https://www.cambridge.org/core/journals/journal-of-fluid-mechanics/article/drop-fragmentation-by-laserpulse-impact/6A949C1372BBD20809731AEE377C42F6.

[24] Javier Hernandez-Rueda et al. 'Early-time hydrodynamic response of a tin droplet driven by laser-produced plasma'. In: *Physical Review Research* 4 (1 Mar. 2022), p. 013142. ISSN: 26431564. DOI: 10.1103/PHYSREVRESEARCH.4.013142/FIGURES/9/MEDIUM. URL: https://journals.aps.org/prresearch/abstract/10.1103/PhysRevResearch.4.013142.

[25] Bo Liu et al. 'Mass Loss from a Stretching Semitransparent Sheet of Liquid Tin'. In: *Physical Review Applied* 13 (2 Feb. 2020). ISSN: 23317019. DOI: 10.1103/PhysRevApplied.13.024035. URL: https://journals.aps.org/prapplied/abstract/10.1103/PhysRevApplied.13.024035.

[26] Bo Liu et al. 'Laser-induced vaporization of a stretching sheet of liquid tin'. In: *Journal of Applied Physics* 129 (5 Feb. 2021). ISSN: 10897550. DOI: 10.1063/5.0036352. URL: https://aip.scitation.org/doi/full/10.1063/5.0036352.

[27] Igor Fomenkov - ASML. *EUV Source for High Volume Manufacturing: Performance at 250 W and Key Technologies for Power Scaling*. https://www.euvlitho.com/2017/S1.pdf. [Online; accessed 12-January-2022]. Nov. 2017.

[28] Wikipedia contributors. *Fusion power — Wikipedia, The Free Encyclopedia*. [Online; accessed 1-November-2021]. 2021. URL: https://en.wikipedia.org/w/index.php?title=Fusion_power&oldid=1052812878.

[29] N.J. Lopes Cardozo. *3MF100: Lectures Notes*. Eindhoven University of Technology, 2019.

[30] Jochen Linke et al. 'Challenges for plasma-facing components in nuclear fusion'. In: *Matter and Radiation at Extremes* 4 (5 Aug. 2019), p. 056201. ISSN: 2468-2047. DOI: 10.1063/1.5090100. URL: https://aip.scitation.org/doi/abs/10.1063/1.5090100.

[31] C S Pitcher and P C Stangeby. 'Experimental divertor physics'. In: *Plasma Physics and Controlled Fusion* 39 (6 June 1997), p. 779. ISSN: 0741-3335. DOI: 10.1088/0741-3335/39/6/001. URL: https://iopscience.iop.org/article/10.1088/0741-3335/39/6/001%20https://iopscience.iop.org/article/10.1088/0741-3335/39/6/001/meta.

[32] A. W. Leonard. 'Edge-localized-modes in tokamaks'. In: *Physics of Plasmas* 21 (9 Sept. 2014), p. 090501. ISSN: 1070-664X. DOI: 10.1063/1.4894742. URL: https://aip.scitation.org/doi/abs/10.1063/1.4894742.

[33] S. Roccella et al. 'CPS Based Liquid Metal Divertor Target for EU-DEMO'. In: *Journal of Fusion Energy 2020 39:6* 39 (6 Oct. 2020), pp. 462–468. ISSN: 1572-9591. DOI: 10.1007/S10894-020-00263-4. URL: https://link.springer.com/article/10.1007/s10894-020-00263-4.

[34] T W Morgan et al. 'Liquid metals as a divertor plasma-facing material explored using the Pilot-PSI and Magnum-PSI linear devices'. In: *Plasma Physics and Controlled Fusion* 60 (1 Oct. 2017), p. 014025. ISSN: 0741-3335. DOI: 10.1088/1361-6587/AA86CD. URL: https://iopscience.iop.org/article/10.1088/1361-6587/aa86cd%20https://iopscience.iop.org/article/10.1088/1361-6587/aa86cd/meta.

[35] P. Rindt et al. 'Conceptual design of a liquid-metal divertor for the European DEMO'. In: *Fusion Engineering and Design* 173 (Dec. 2021), p. 112812. ISSN: 0920-3796. DOI: 10.1016/J.FUSENGDES.2021.112812.

[36] B. A. Collings et al. 'Optical absorption spectra of Au7, Au9, Au11, and Au13, and their cations: Gold clusters with 6, 7, 8, 9, 10, 11, 12, and 13 s-electrons'. In: *The Journal of Chemical Physics* 101 (5 Aug. 1998), p. 3506. ISSN: 0021-9606. DOI: 10.1063/1.467535. URL: https://aip.scitation.org/doi/abs/10.1063/1.467535.

[37] Vlasta Bonačić-Koutecký et al. 'An accurate relativistic effective core potential for excited states of Ag atom: An application for studying the absorption spectra of Agn and Agn+ clusters'. In: *The Journal of Chemical Physics* 110 (8 Feb. 1999), p. 3876. ISSN: 0021-9606. DOI: 10.1063/1.478242. URL: https://aip.scitation.org/doi/abs/10.1063/1.478242.

[38] Vlasta Bonačić-Koutecky, Vincent Veyret and Roland Mitrić. 'Ab initio study of the absorption spectra of Agn (n=5–8) clusters'. In: *The Journal of Chemical Physics* 115 (22 Nov. 2001), p. 10450. ISSN: 0021-9606. DOI: 10.1063/1.1415077. URL: https://aip.scitation.org/doi/abs/10.1063/1.1415077.

[39] Andreas Lehr, Marc Jäger and Rolf Schäfer. 'Optical Properties of Si n+(n = 6-100) Clusters: The Approach to Bulk Behavior'. In: *Journal of Physical Chemistry C* 124 (1 Jan. 2020), pp. 1070–1076. ISSN: 19327455. DOI: 10.1021/ACS.JPCC.9B08927/ASSET/IMAGES/LARGE/JP9B08927_0003.JPEG. URL: https://pubs.acs.org/doi/full/10.1021/acs.jpcc.9b08927.

[40] Andreas Lehr et al. 'Optical absorption and shape transition in neutral Sn N clusters with N <= 40: a photodissociation spectroscopy and electric beam deflection study'. In: *Physical Chemistry Chemical Physics* 24 (19 May 2022), pp. 11616–11635. ISSN: 1463-9076. DOI: 10.1039/D2CP01171A. URL: https://pubs.rsc.org/en/content/articlehtml/2022/cp/d2cp01171a%20https://pubs.rsc.org/en/content/articlelanding/2022/cp/d2cp01171a.

[41] Pierre Bouguer. *Essai d'optique sur la gradation de la lumière*. Claude Jombert, 1729, pp. 16–22. URL: https://archive.org/details/UFIE003101_TO0324_PNI-2703_000000.

[42] J.H. Lambert. *Photometria sive de mensura et gradibus luminis, colorum et umbrae*. Eberhardt Klett, 1760. URL: https://archive.org/details/TO0E039861_TO0324_PNI-2733_000000.

[43] Beer. 'Bestimmung der Absorption des rothen Lichts in farbigen Flüssigkeiten'. In: *Annalen der Physik und Chemie* 162 (5 1852), pp. 78–88. DOI: 10.1002/andp.18521620505. URL: https://books.google.com/books?id=PNmXAAAAIAAJ&pg=PA78.

[44] Robert C. Hilborn. 'Einstein coefficients, cross sections, f-values, dipole moments, and all that'. In: *American Journal of Physics* 50 (11 Nov. 1982), pp. 982–986. ISSN: 0002-9505. DOI: 10.1119/1.12937. URL: http://aapt.scitation.org/doi/10.1119/1.12937.

[45] Ove Axner et al. 'Line strengths, A-factors and absorption cross-sections for fine structure lines in multiplets and hyperfine structure components in lines in atomic spectrometry—a user's guide'. In: *Spectrochimica Acta Part B: Atomic Spectroscopy* 59 (1 Jan. 2004), pp. 1–39. ISSN: 0584-8547. DOI: 10.1016/J.SAB.2003.10.002.

[46] Wolfgang Demtröder. *Laser spectroscopy 1: Basic principles*. Vol. 9783642538599. Springer-Verlag Berlin Heidelberg, Nov. 2014, pp. 1–496. ISBN: 9783642538599. DOI: 10.1007/978-3-642-53859-9.

[47] C. J. Foot. 'Atomic physics'. In: (2005), p. 331.

[48] Wikipedia contributors. *Voigt profile — Wikipedia, The Free Encyclopedia*. [Online; accessed 20-October-2021]. 2021. URL: https://en.wikipedia.org/w/index.php?title=Voigt_profile&oldid=1045866835.

[49] R. M. Drake and J. E. Gordon. 'Mie scattering'. In: *American Journal of Physics* 53 (10 Oct. 1985), pp. 955–962. ISSN: 0002-9505. DOI: 10.1119/1.14011. URL: http://aapt.scitation.org/doi/10.1119/1.14011.

[50] Craig F. Bohren and Donald R. Huffman. *Absorption and scattering of light by small particles*. Wiley, 1983, p. 530. ISBN: 0471293407.

[51] A. Alonso-Medina and C. Colon. 'Measured Stark Widths of Several Sn i and Sn ii Spectral Lines in a Laser-induced Plasma'. In: *The Astrophysical Journal* 672 (2 2008). ISSN: 0004-637X. DOI: 10.1086/523844.

[52] M. V. Romalis, E. Miron and G. D. Cates. 'Pressure broadening of Rb D1 and D2 lines by 3He, 4He, N2, and Xe: Line cores and near wings'. In: *Physical Review A* 56 (6 Dec. 1997), p. 4569. ISSN: 10941622. DOI: 10.1103/PhysRevA.56.4569. URL: https://journals.aps.org/pra/abstract/10.1103/PhysRevA.56.4569.

[53] Wikipedia contributors. *Tin — Wikipedia, The Free Encyclopedia*. [Online; accessed 4-January-2022]. 2021. URL: https://en.wikipedia.org/w/index.php?title=Tin&oldid=1062557950.

[54] M Brieger and P Zimmermann. *Level-Crossing-Untersuchung der Hyperfeinstruktur von Sn117 und Sn119 im (5p6s) 3P1°-Term des Sn I-Spektrums*. 1967. URL: https://www.osti.gov/biblio/4553077.

[55] J.D. Silver and D.N. Stacey. 'Isotope shift and hyperfine structure in the atomic spectrum of tin'. In: *Proceedings of the Royal Society of London. A. Mathematical and Physical Sciences* 332 (1588 Feb. 1973), pp. 129–138. ISSN: 0080-4630. DOI: 10.1098/RSPA.1973.0016. URL: https://royalsocietypublishing.org/doi/abs/10.1098/rspa.1973.0016.

[56] W.R. Hindmarsch and H. Kuhn. 'Isotope Shifts and Hyperfine Structure in the Atomic Spectrum of Tin'. In: *Proceedings of the Physical Society. Section A* 68 (5 May 1955), p. 433. ISSN: 0370-1298. DOI: 10.1088/0370-1298/68/5/311. URL: https://iopscience.iop.org/article/10.1088/0370-1298/68/5/311%20https://iopscience.iop.org/article/10.1088/0370-1298/68/5/311/meta.

[57] Wikipedia contributors. *Isotopes of tin — Wikipedia, The Free Encyclopedia*. https://en.wikipedia.org/w/index.php?title=Isotopes_of_tin&oldid=1069510076. [Online; accessed 27-April-2022]. 2022.

[58] Scott Prahl. *miepython*. https://miepython.readthedocs.io/en/latest/. [Online; accessed 27-April-2022].

[59] Benjamin Sumlin. *PyMieScatt*. https://pymiescatt.readthedocs.io/en/latest/. [Online; accessed 27-April-2022].

[60] Gerardo Cisneros, J. S. Helman and C. N. J. Wagner. 'Dielectric function of liquid tin between 250 and 1100°C'. In: *Physical Review B* 25 (6 Mar. 1982), p. 4248. DOI: 10.1103/PhysRevB.25.4248. URL: https://journals.aps.org/prb/abstract/10.1103/PhysRevB.25.4248.

[61] Benjamin J. Sumlin et al. 'UV–Vis–IR spectral complex refractive indices and optical properties of brown carbon aerosol from biomass burning'. In: *Journal of Quantitative Spectroscopy and Radiative Transfer* 206 (Feb. 2018), pp. 392–398. ISSN: 0022-4073. DOI: 10.1016/J.JQSRT.2017.12.009.

[62] Benjamin J. Sumlin et al. 'Atmospheric Photooxidation Diminishes Light Absorption by Primary Brown Carbon Aerosol from Biomass Burning'. In: *Environmental Science and Technology Letters* 4 (12 Dec. 2017), pp. 540–545. ISSN: 23288930. DOI: 10.1021/ACS.ESTLETT.7B00393/SUPPL_FILE/EZ7B00393_SI_001.PDF. URL: https://pubs.acs.org/doi/abs/10.1021/acs.estlett.7b00393.

[63] Benjamin J. Sumlin, William R. Heinson and Rajan K. Chakrabarty. 'Retrieving the aerosol complex refractive index using PyMieScatt: A Mie computational package with visualization capabilities'. In: *Journal of Quantitative Spectroscopy and Radiative Transfer* 205 (Jan. 2018), pp. 127–134. ISSN: 0022-4073. DOI: 10.1016/J.JQSRT.2017.10.012.

[64] A. Kramida et al. *NIST Atomic Spectra Database*. 2020. DOI: https://dx.doi.org/10.18434/T4W30F. URL: https://www.nist.gov/pml/atomic-spectra-database.

[65] D Kurilovich. 'Laser-induced dynamics of liquid tin microdroplets'. 2019. URL: https://www.researchgate.net/profile/Dmitry-Kurilovich/publication/332934961_Laser-induced_dynamics_of_liquid_tin_microdroplets/links/5cd4316f299bf14d958374f5/Laser-induced-dynamics-of-liquid-tin-microdroplets.pdf.

[66] R. Meijer. 'Tailored Laser-Droplet Interaction for target formation in extreme ultraviolet sources'. 2021.

Appendices

A Tin atomic transitions in the UV

The main text mentions that only atomic transitions with a defined Einstein coefficient according to NIST ASD[64] are investigated. All lines between 190 to 600 nm are modeled. This appendix gives some more information about the atomic resonances. Table 1 shows more information about most atomic resonances in the UV (190 to 400 nm). This information includes their Einstein coefficient and the configurations of the lower and upper states.

Table 1: An overview of atomic transitions for tin-I between 225 to 400 nm. Only resonances with a defined Einstein coefficient above $5 \cdot 10^6\,\mathrm{s}^{-1}$ according to NIST ASD[64] are shown.

Vacuum wavelength (nm)	Einstein coefficient (s^{-1})	Lower state	Upper state	Transition
226.96	$1.20 \cdot 10^8$	$5s^25p^2\ ^3P_2$	$5s^25p5d\ ^3D_3$	$5p^2\ ^3P_2 - 5p5d\ ^3D_3$
228.74	$3.10 \cdot 10^7$	$5s^25p^2\ ^3P_2$	$5s^25p5d\ ^1D_2$	$5p^2\ ^3P_2 - 5p5d\ ^1D_2$
231.79	$2.00 \cdot 10^8$	$5s^25p^2\ ^1D_2$	$5s^25p6d\ ^3F_3$	$5p^2\ ^1D_2 - 5p6d\ ^3F_3$
233.55	$6.60 \cdot 10^7$	$5s^25p^2\ ^3P_1$	$5s^25p5d\ ^3D_1$	$5p^2\ ^3P_1 - 5p5d\ ^3D_1$
235.56	$1.70 \cdot 10^8$	$5s^25p^2\ ^3P_1$	$5s^25p5d\ ^3D_2$	$5p^2\ ^3P_1 - 5p5d\ ^3D_2$
240.89	$1.80 \cdot 10^7$	$5s^25p^2\ ^1D_2$	$5s^25p5d\ ^1P_1$	$5p^2\ ^1D_2 - 5p5d\ ^1P_1$
242.24	$2.50 \cdot 10^8$	$5s^25p^2\ ^1D_2$	$5s^25p5d\ ^1F_3$	$5p^2\ ^1D_2 - 5p5d\ ^1F_3$
243.02	$1.50 \cdot 10^8$	$5s^25p^2\ ^3P_2$	$5s^25p5d\ ^3F_3$	$5p^2\ ^3P_2 - 5p5d\ ^3F_3$
248.42	$2.10 \cdot 10^7$	$5s^25p^2\ ^3P_2$	$5s^25p5d\ ^3F_2$	$5p^2\ ^3P_2 - 5p5d\ ^3F_2$
249.25	$1.70 \cdot 10^7$	$5s^25p^2\ ^1S_0$	$5s^25p8s\ ^3P_1$	$5p^2\ ^1S_0 - 5p8s\ ^3P_1$
249.65	$6.20 \cdot 10^7$	$5s^25p^2\ ^1D_2$	$5s^25p5d\ ^3P_2$	$5p^2\ ^1D_2 - 5p5d\ ^3P_2$
252.47	$7.40 \cdot 10^6$	$5s^25p^2\ ^1D_2$	$5s^25p7s\ ^3P_1$	$5p^2\ ^1D_2 - 5p7s\ ^3P_1$
254.73	$2.10 \cdot 10^7$	$5s^25p^2\ ^3P_0$	$5s^25p6s\ ^1P_1$	$5p^2\ ^3P_0 - 5p6s\ ^1P_1$
255.89	$3.40 \cdot 10^7$	$5s^25p^2\ ^1S_0$	$5s^25p8d\ ^3D_1$	$5p^2\ ^1S_0 - 5p8d\ ^3D_1$
257.24	$4.50 \cdot 10^7$	$5s^25p^2\ ^1D_2$	$5s^25p5d\ ^3D_3$	$5p^2\ ^1D_2 - 5p5d\ ^3D_3$
259.52	$3.00 \cdot 10^7$	$5s^25p^2\ ^1D_2$	$5s^25p5d\ ^1D_2$	$5p^2\ ^1D_2 - 5p5d\ ^1D_2$
263.78	$1.10 \cdot 10^7$	$5s^25p^2\ ^1S_0$	$5s^25p7d\ ^3D_1$	$5p^2\ ^1S_0 - 5p7d\ ^3D_1$
266.20	$1.10 \cdot 10^7$	$5s^25p^2\ ^3P_1$	$5s^25p6s\ ^1P_1$	$5p^2\ ^3P_1 - 5p6s\ ^1P_1$
270.73	$6.60 \cdot 10^7$	$5s^25p^2\ ^3P_1$	$5s^25p6s\ ^3P_2$	$5p^2\ ^3P_1 - 5p6s\ ^3P_2$
278.06	$1.80 \cdot 10^7$	$5s^25p^2\ ^1D_2$	$5s^25p5d\ ^3F_3$	$5p^2\ ^1D_2 - 5p5d\ ^3F_3$
278.58	$1.40 \cdot 10^7$	$5s^25p^2\ ^1D_2$	$5s^25p5d\ ^3D_1$	$5p^2\ ^1D_2 - 5p5d\ ^3D_1$
278.87	$1.40 \cdot 10^7$	$5s^25p^2\ ^1S_0$	$5s^25p8s\ ^3P_1$	$5p^2\ ^1S_0 - 5p8s\ ^3P_1$
281.34	$2.30 \cdot 10^7$	$5s^25p^2\ ^1S_0$	$5s^25p7s\ ^1P_1$	$5p^2\ ^1S_0 - 5p7s\ ^1P_1$
281.44	$1.20 \cdot 10^7$	$5s^25p^2\ ^1D_2$	$5s^25p5d\ ^3D_2$	$5p^2\ ^1D_2 - 5p5d\ ^3D_2$
284.08	$1.70 \cdot 10^8$	$5s^25p^2\ ^3P_2$	$5s^25p6s\ ^3P_2$	$5p^2\ ^3P_2 - 5p6s\ ^3P_2$
285.15	$3.30 \cdot 10^7$	$5s^25p^2\ ^1D_2$	$5s^25p5d\ ^3F_2$	$5p^2\ ^1D_2 - 5p5d\ ^3F_2$
286.42	$5.40 \cdot 10^7$	$5s^25p^2\ ^3P_0$	$5s^25p6s\ ^3P_1$	$5p^2\ ^3P_0 - 5p6s\ ^3P_1$
291.44	$8.30 \cdot 10^7$	$5s^25p^2\ ^1S_0$	$5s^25p6d\ ^3D_1$	$5p^2\ ^1S_0 - 5p6d\ ^3D_1$
301.00	$3.80 \cdot 10^7$	$5s^25p^2\ ^3P_1$	$5s^25p6s\ ^3P_1$	$5p^2\ ^3P_1 - 5p6s\ ^3P_1$
303.37	$6.20 \cdot 10^7$	$5s^25p^2\ ^1S_0$	$5s^25p5d\ ^1P_1$	$5p^2\ ^1S_0 - 5p5d\ ^1P_1$
303.50	$2.00 \cdot 10^8$	$5s^25p^2\ ^3P_1$	$5s^25p6s\ ^3P_0$	$5p^2\ ^3P_1 - 5p6s\ ^3P_0$
314.27	$1.90 \cdot 10^7$	$5s^25p^2\ ^1S_0$	$5s^25p5d\ ^3P_1$	$5p^2\ ^1S_0 - 5p5d\ ^3P_1$
317.60	$1.00 \cdot 10^8$	$5s^25p^2\ ^3P_2$	$5s^25p6s\ ^3P_1$	$5p^2\ ^3P_2 - 5p6s\ ^3P_1$
326.33	$2.70 \cdot 10^8$	$5s^25p^2\ ^1D_2$	$5s^25p6s\ ^1P_1$	$5p^2\ ^1D_2 - 5p6s\ ^1P_1$
333.16	$2.00 \cdot 10^7$	$5s^25p^2\ ^1D_2$	$5s^25p6s\ ^3P_2$	$5p^2\ ^1D_2 - 5p6s\ ^3P_2$
380.21	$2.80 \cdot 10^7$	$5s^25p^2\ ^1D_2$	$5s^25p6s\ ^3P_1$	$5p^2\ ^1D_2 - 5p6s\ ^3P_1$

A Grotian diagram can be made to visualize the transitions within the atom. Figure 26 shows such a diagram of the transitions between 234 to 292 nm.

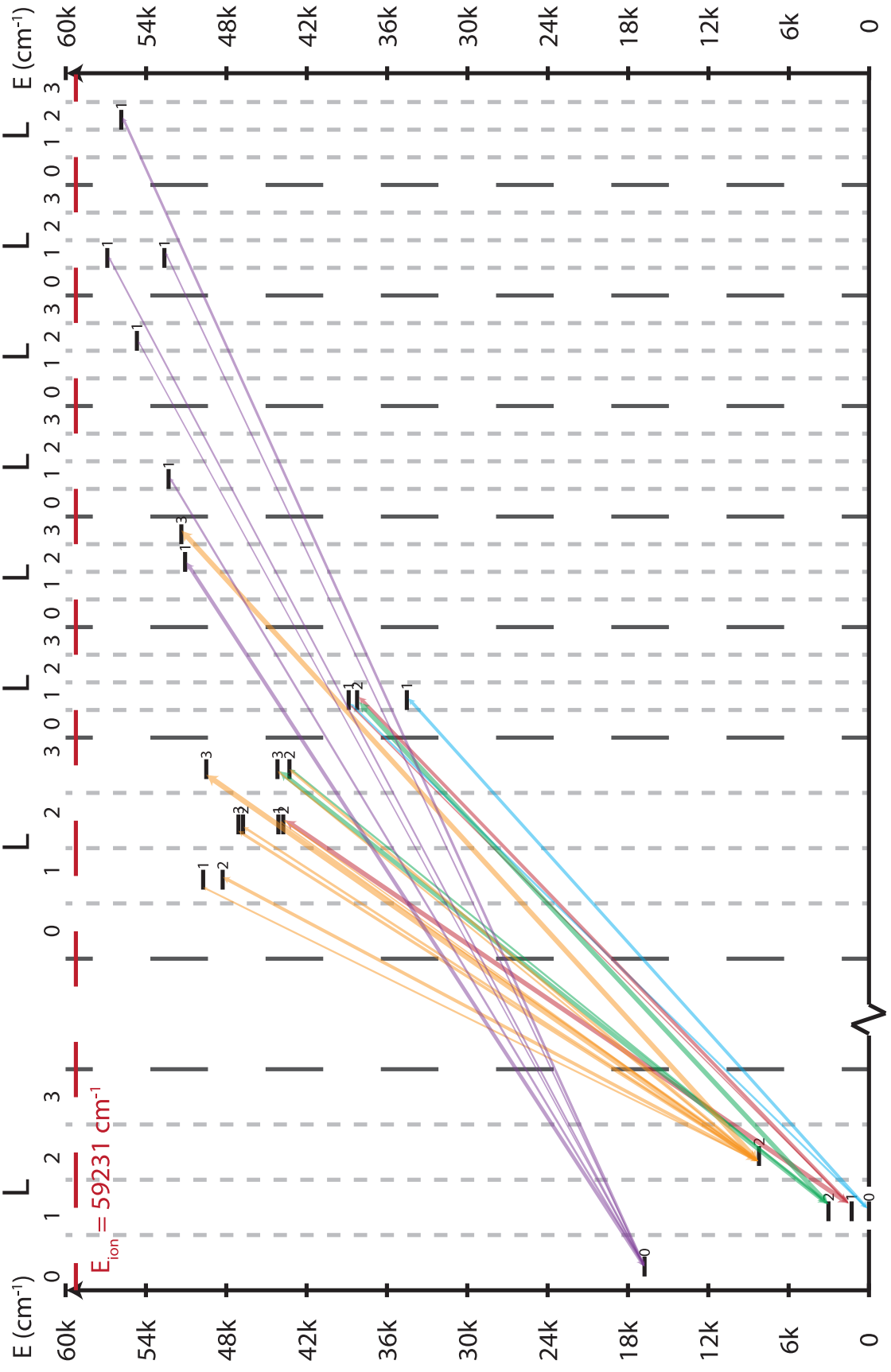

Figure 26: A Grotian diagram of all transitions of tin-I (with a defined Einstein coefficient) between 234 to 292 nm. At the bottom, the configuration is noted, while the top shows the possible L-values for that configuration. The top also shows the ionization energy. The flat lines indicate possible energy levels and which configuration and L-value they have. The number beside an energy level indicates the j-quantum number of that level. The lines indicate atomic transitions. The color indicates their ground state. Their thickness is scaled to their Einstein coefficient, so thicker lines are stronger transitions.

B Model details

The Python package that models absorption spectra of tin vapor is called `SnAS`. The general concept of the model is explained in Section 3. In this section, the code setup will be discussed in more detail.

The model is built upon `numpy`, a Python package for *numerical python*, shortened to `numpy`. This means that all the code is written using arrays for fast calculations. The usage of arrays relies on discretized versions of the equations presented in the main text.

When a user initializes a `AbsorptionSpectrum`, the model calculates the base information of all atomic resonances in the given range. This information is stored. A similar initialization is done for Mie scattering information by preparing the refractive index. During this step, the user can also easily switch off either atomic absorption or Mie scattering.

Finally, the user can request single wavelength absorption information or a spectrum. At that moment, the model calculates the extinction cross-section over the relevant range. This is done by individually calculating the cross-section of each atomic resonance. These cross-sections are summed, and the Mie scattering cross-section is added to get a complete cross-section for each frequency (discretized). This resulting cross-section is to solve Beer-Lambert and is multiplied with the incoming light spectral shape. This spectrally resolved absorption is the end for the single wavelength case, as this information is plotted. The spectrally resolved fixed-wavelength result is summed for a sweep to get one total extinction per center wavelength of the incoming light. Combining the cross-section with different laser spectral shapes is repeated until the entire scan range is complete.

The code block below shows how easy it is to create an absorption spectrum using the model.

```
import SnAS

# Define peaks measured [nm]
peaks = np.asarray([235.56, 242.24, 243.02, 254.73, 257.24,
                    266.20, 270.73, 284.08, 286.42,
                    303.37, 303.50, 317.60, 326.33, 380.21])
# Vapor
density = 2.4e24  # m-3
path_length = 80e-6  # m
atomic_ratio = 0.10
vapor = SnAS.Column(density, path_length, atomic_ratio,
                    nanodroplet_distribution='single',
                    droplet_size_mean=30e-9)
# Laser
line_width = 5  # cm-1
opo = SnAS.Laser("OPO", line_width)

# Environment
temperature = 1700  # K
pressure = 3e-7  # mbar
dalek2 = SnAS.Environment(temperature, pressure)

# Make spectrum
absorption = SnAS.AbsorptionSpectrum(vapor, dalek2, [190, 410],
                                     atomic=True, mie=True, peak_filters=peaks)
absorption.scan_wavelengths(opo, 308, 75, save=True)
```

C Spectrometer calibration

The spectrometer calibration is split into fixed grating positions as a single position limits the visible range to ∼59 nm. Thus, five grating angles are chosen to span the 220 to 410 nm range desired. Each position is calibrated separately using a Princeton Instruments USB-Hg-NeAr HeNe + Hg calibration lamp. The found peaks are fit using a Gaussian, and their center is found with sub-pixel resolution. This can be seen on the first row Fig. 27. These found centers are matched to NIST ASD[64] data for their real wavelength value. Vacuum wavelengths are used everywhere. For each grating position, a polynomial is fitted to link the pixel position to a wavelength. This is visible on the second row of Fig. 27. This procedure results in a maximum 0.01 nm error between the atomic resonances data from NIST ASD and the calibration. The RMSE is also measured to be below 0.01 nm for all positions. The residual is visible on the third row of Fig. 27. In total, the precision of this method is estimated to be around 0.01 - 0.02 nm.

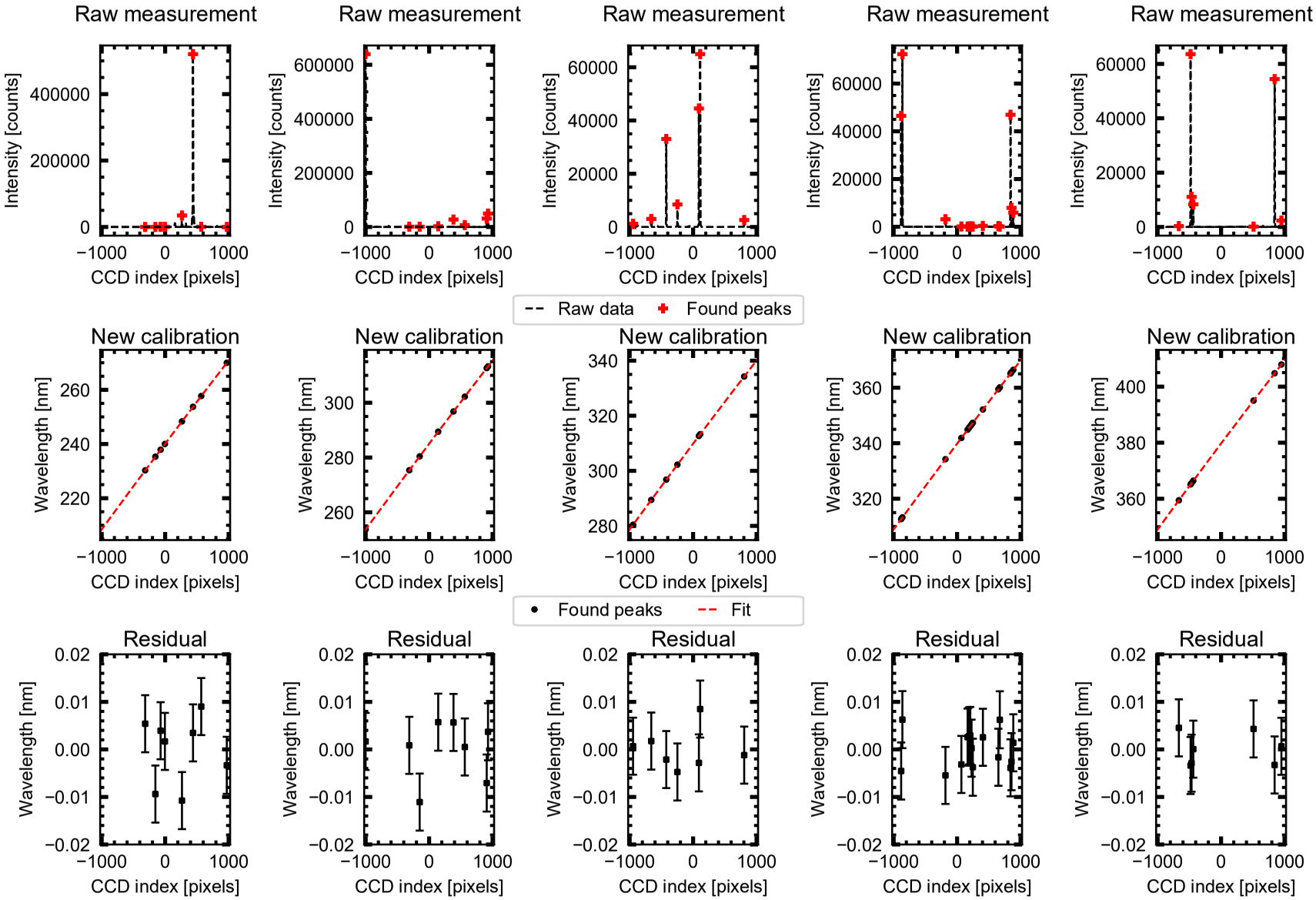

Figure 27: An example of the spectrometer calibration. This measurement is done with the 1200 l/mm grating. Five grating positions are used. These are defined by their center wavelength. From left to right, these center wavelengths are 240, 285, 310, 340, and 380 nm. For each, the procedure as described in the main text is followed to get a calibration with an root-mean-square-error (RMSE) of less than 0.01 nm. The image shows the raw data and the peaks on the top row. The middle row shows the third-order polynomial fit while the last row shows the residual of that fit.

D OPO output wavelength calibration

The Continuum Horizon II OPO comes with control software that can be used to set the desired wavelength. However, this desired wavelength is not the produced wavelength due to offsets in the calibration of the crystals. Because of these offsets, the wavelength set in the software is called the *input wavelength*. The *output* wavelength is calibrated to compensate for this offset. This calibration procedure is part of the `OPOcontrol` package and is used during the automated scans.

A calibrated spectrometer is needed to perform this calibration. The spectrometer calibration can be seen in the main text in Section 4 and above. The wavelength calibration consists of two steps. First, `OPOcontrol` is used to scan many wavelengths several times while the output wavelength is measured by the spectrometer each time. Second, the output wavelength for each input wavelength is determined using the spectrometer calibration and saved in a calibration file for later use.

An overview of the method can be seen in Fig. 28. Panel a) shows the offset measured between the input and output wavelengths. A positive offset means a longer wavelength output than input. For each input wavelength, ten samples are taken. The red dashed line is the spline drawn through all the data points and is used as the definitive conversion from input to output wavelengths. Some of the regime changes of the OPO, where internals have to be changed, are visible, such as the 292 nm change. Panel b) shows the standard deviation of the output wavelength per input wavelength. This figure shows that the output wavelength of the OPO is very repeatable with a standard deviation below the input resolution (which is 0.01 nm) for most of the UV range. In this graph, every color represents a different regime of the OPO. To conclude, the top graph of Fig. 28 can be inverted to find the needed input wavelength for that output wavelength. This inversion is done every time a user using `OPOcontrol` requests a wavelength. `OPOcontrol` then sets the OPO control software to that input wavelength to get the desired wavelength out of the OPO.

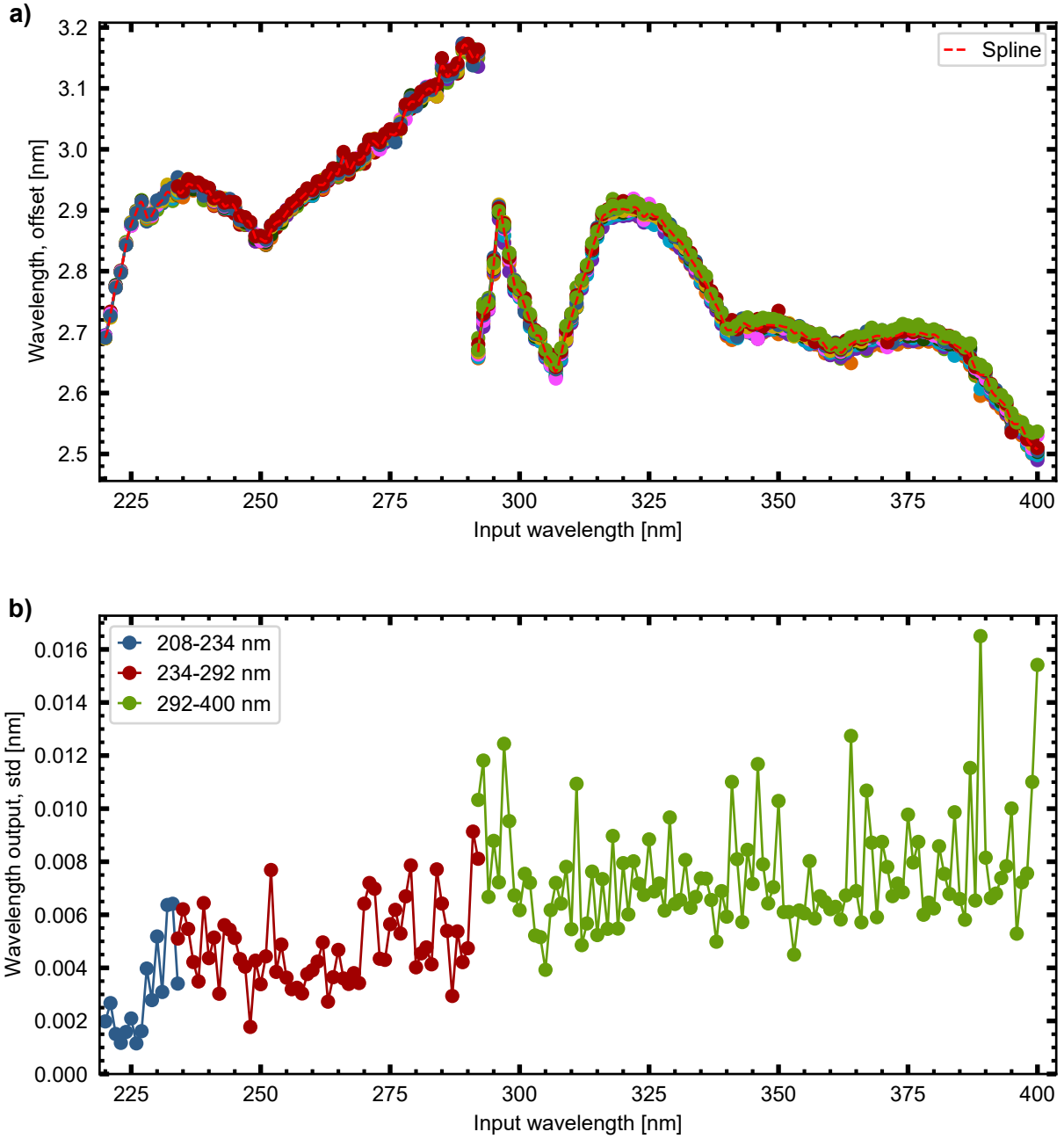

Figure 28: An overview of the wavelength calibration results. Panel a) shows the found offset for each input wavelength, where positive offset means a longer output wavelength than input wavelength. A spline through the ten individual data points is also shown. Panel b) shows the standard deviation of the ten samples of the output wavelength. It shows that the OPO is a very reproducible output wavelength, below the input resolution (which is 0.01 nm) for most of the UV range.

E OPO bandwidth

The spectral bandwidth of the OPO was determined using the SCP320 spectrometer. The 3600 l/mm grating is used to get the highest resolution possible. Using the 3600 l/mm grating does mean that the previously performed calibration is no longer valid and that the grating angle will have to change often.

The first step of the procedure is to use the Princeton Instruments USB-Hg-NeAr HeNe + Hg calibration lamp to find the instrumental broadening of the spectrometer. The individual peaks are fitted with a Gaussian to get a relation between instrumental broadening FWHM and wavelength. The grating equation is also fitted to the individual peaks to get a conversion from pixels to nm for each grating position. The grating equation is used as this is simpler than a full calibration for each grating angle. This full calibration would require many different angles for the desired range and the small range of the 3600 l/mm grating. The grating equation also has an acceptable accuracy as the only desired value is a conversion from pixels to nm, not a precise absolute wavelength calibration.

The second step is to measure the spectral FWHM of the OPO for many wavelengths. Finally, the actual Gaussian FWHM of the OPO is determined by calculating the quadratic difference between the measured FWHM and the instrumental broadening. In this step, it is assumed that the measured FWHM of the OPO is simply the combination of two Gaussians, its real FWHM and the instrumental broadening. The result of this procedure gives a spectral FWHM over wavelength, which can be seen in Fig. 29.

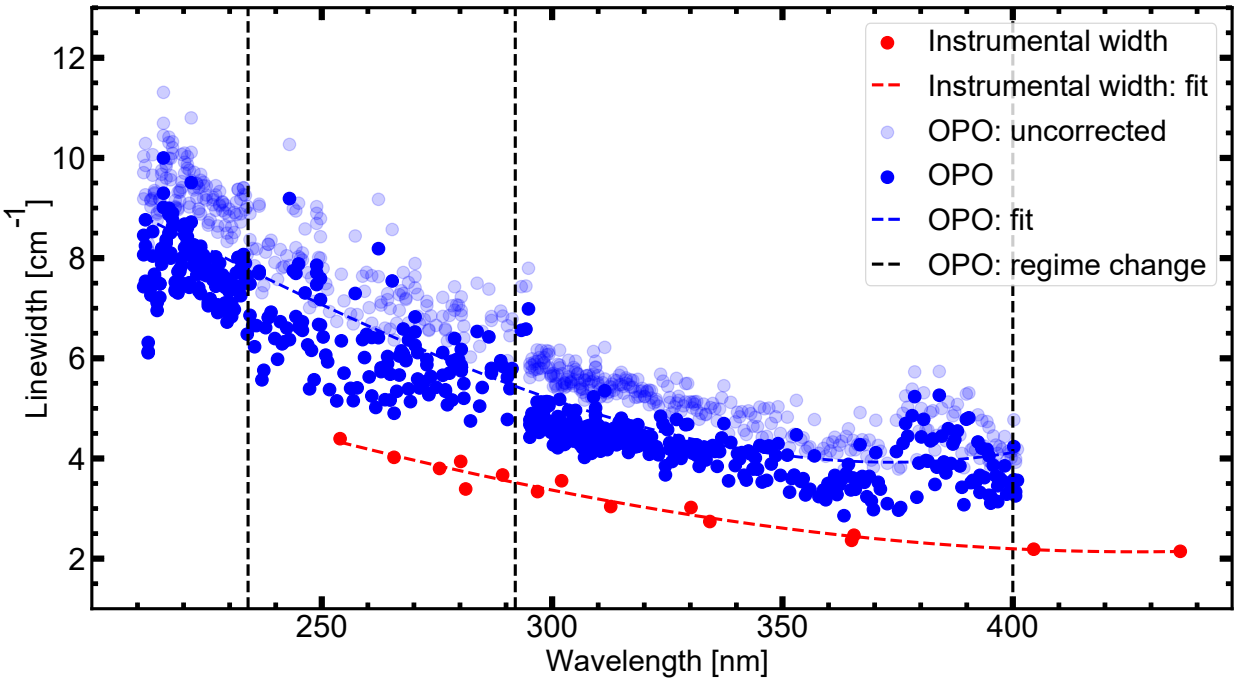

Figure 29: An overview of the bandwidth calibration. The instrumental width is shown in red, and a third-order spline through the points. The translucent blue dots show the raw measured bandwidth of the OPO, while the solid blue dots are the corrected values. A third-order fit is shown again. The OPO regime changes are also plotted.

F OPOcontrol details

The `OPOcontrol` package was already discussed in Section 4. In this section, the parts of `OPOcontrol` will be discussed in more detail. This section is more intended as a summary of all the features in the package for a future user. `OPOcontrol` was built with an object-oriented *class*-based structure. Hence, the features of `OPOcontrol` will be explained by summarizing the classes in the code.

The first part of `OPOcontrol` relates to the spectrometer calibration. As mentioned, this part is needed to find the output wavelength calibration of the OPO. The spectrometer calibration part of `OPOcontrol` consists of the following parts. These parts can be found in `SpectrometerReader.py`.

- `SpectrumLoader` can load a single output .csv from either the Mightex (other spectrometer that was initially used) or the SCT320 spectrometer. It loads the data and has features to convert the pixels to wavelength or fit peaks.
- `SpectrometerCalibration` is the base class for any spectrometer calibration. It incorporates all needed steps as discussed in Appendix C. This class is not intended to be used directly. It uses the `SpectrumLoader` to load the raw data.
- `SpectrometerCalibrationMightex` extends the `SpectrometerCalibration` class with all the final features needed to calibrate the Mightex spectrometer.
- `SpectrometerCalibrationPIBase` extends the `SpectrometerCalibration` class with additional features needed to calibrate the SCT320 spectrometer. This class is not intended to be used directly. It only exists to be inherited by other classes, such as the one needed to calibrate the bandwidth of the OPO.
- `SpectrometerCalibrationPI` extends the `SpectrometerCalibrationPIBase` and is used to calibrate the SCT320 spectrometer.

`SpectrometerLinewidthFinder` extends the `SpectrometerCalibrationPIBase` as well and includes the code to determine the bandwidth of the OPO. For further info, see Appendix E.

The next part of `OPOcontrol` relates to the output wavelength calibration of the OPO. A valid spectrometer calibration is needed to use this part. The following parts can be found in `Wavelength Controller.py`.

- `SweepAnalyzer` analyzes the output wavelength when sweeping the input wavelength of the OPO. It uses the `SpectrumLoader` class to load the raw data. It results in a table that relates input wavelength to output wavelength for each time it was measured. This result can be saved as .csv.
- `WavelengthController` takes the .csv of `SweepAnalyzer` and fits it with any spline/curve desired. Its main purpose is to give the input wavelength needed for the desired output wavelength or the other way around. This class is used a lot in automated `OPOcontrol` runs as it is the class that gets the input wavelength for the desired output.

As mentioned in the main text, the SCT320 spectrometer control was also automated. This code can be found in `SpectrometerController.py` and consists of the following parts.

- `GratingController` is the code used to automate the moving of the grating to a new angle. This is done via COM.
- `PICamController` is the code used to automate reading out the camera of the spectrometer when desired.

- `SpectrometerController` combines `GratingController` and `PICamController` to allow for one class that both ensures that the grating is in the right position and reads out the camera when needed.

The control of the imaging lens on the automated stage can be found in `LensController.py`. The control of the lens consists of the following parts.

- `Lens` is a simple class to model the behavior of a lens as the wavelength of the light passing through it is changed.
- `StageMotorController` is the class that controls the Newport stage, ensuring that it is in the right place.
- `LensController` combines the two classes above to ensure that the lens is always in the right place. The class allows calibrating the stage position versus wavelength, which can be saved to .csv. This calibration, together with the modeled evolution in the `Lens` clas, allows the code to know where the lens should be for each wavelength. The class then uses the `StageMotorController` to move the lens to the right place.

The code to control devices such as the OPO and the Delay Generators can be found in `other_devices.py`. The actual control of the OPO software is done via SSD, which was implemented during this project as a shared effort of the AMOLF/ARCNL software department and the author. It was chosen to put the OPO control in SSD as the OPO is considered a long-term addition to the setup. Thus, this would be a more future-proof implementation.

The scripts that perform the loops, as shown in Fig. 13, are found in the `scripts` folder and utilize the classes described above.

G Detailed target specifications

Table 2 below shows the details of the targets presented in this thesis. Target A1 to A3 are named as these are the same target with only minor differences. They are designed to be the same target, only created at a different moment in the experimental campaign. Thus, the exact values differ slightly, while the resulting target is nearly identical. Target A2 is target A1 but with the line VP instead of the full VP. These are also made on the same day during the experimental campaign, hence the identical PP energy value.

Table 2: A detailed overview of all the targets shown in this thesis.

Target name	**Droplet size** (µm)	**PP energy** (mJ)	**PP-VP delay** (µs)	**VP energy** (mJ)	**VP type (full/delayline/line)**	**Used figures**
Target A1	27	28.8	3.1	8.4	full	19, 21
Target A2	27	28.8	3.1	0.5	line	19, 22, 24
Target A3	27	28.0	3.1	7.2	full	20
Target B	27	28.0	2.25	0.7	line	22
Target C	17	22.4	1.2	0.15	line	23
Target D1	36	41.8	2	0.96	line	23
Target D2	36	41.8	2	2.24	line + delay line	23

H Atomic resonances in spatial sweep

The next page shows the atomic resonances of Fig. 21 in more detail including term symbols.

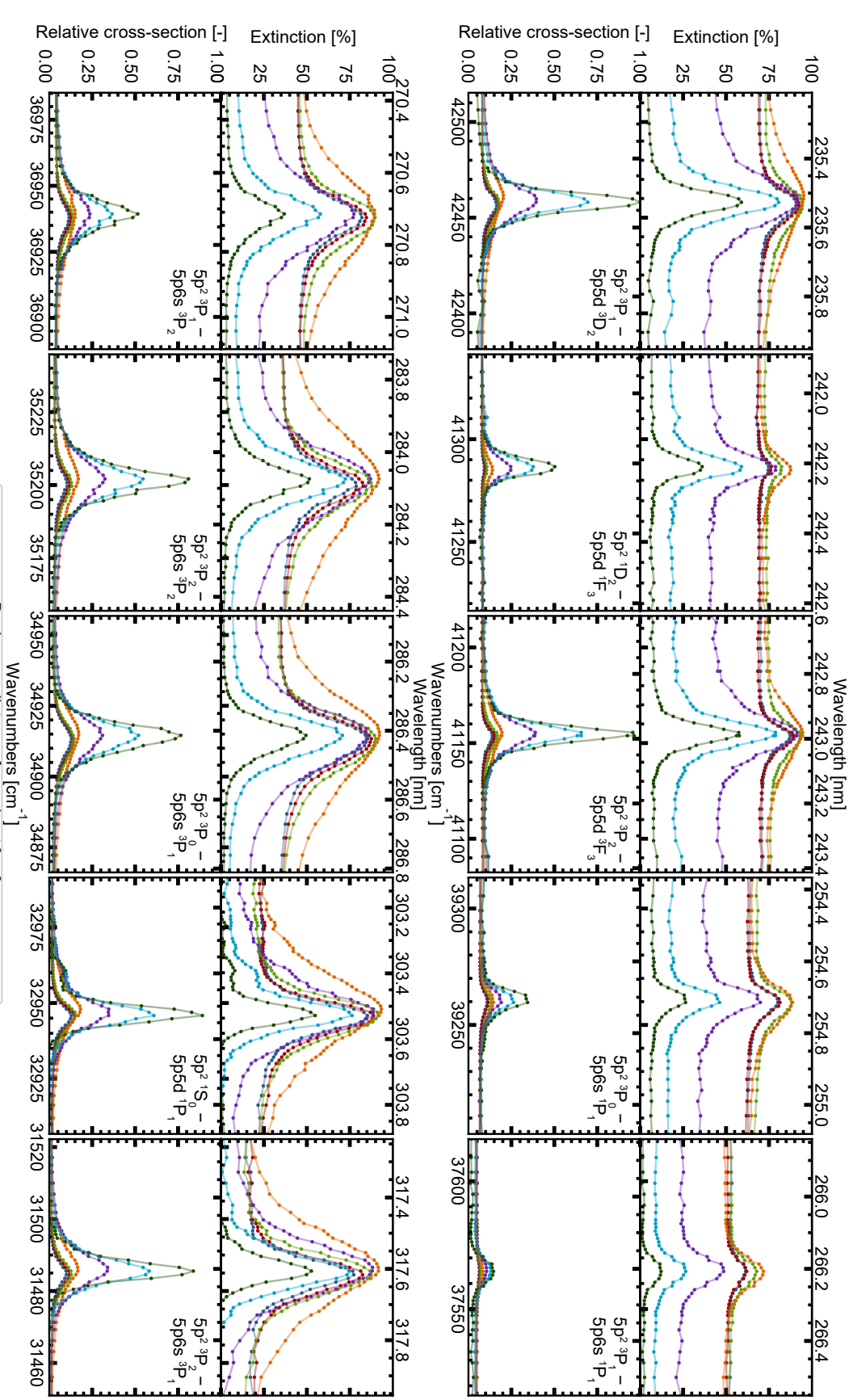

Figure 30: A larger figure showing the atomic resonances as shown in Fig. 21 in more detail. The term symbols for each resonance are given as well.

I Saturation broadening test

The result of the saturation broadening test can be seen in Fig. 31.

Figure 31 shows two atomic resonances that were scanned twice. Both were scanned once in the *normal* case. For this *normal* case, the UV light energy is tuned via a filter to get the desired number of counts (∼10 000) on the pco.ultraviolet. Both were also scanned in extreme cases; the 284.08 nm resonance was scanned with extra filters after the chamber. The 286.42 nm resonance was scanned with the minimal counts to work (∼1200). Very little difference can be seen between the *normal* case and the extreme cases. The two orders of magnitude difference in energy should show a tenfold change in cross-section. This change is not visible; hence, saturation broadening is not a significant effect.

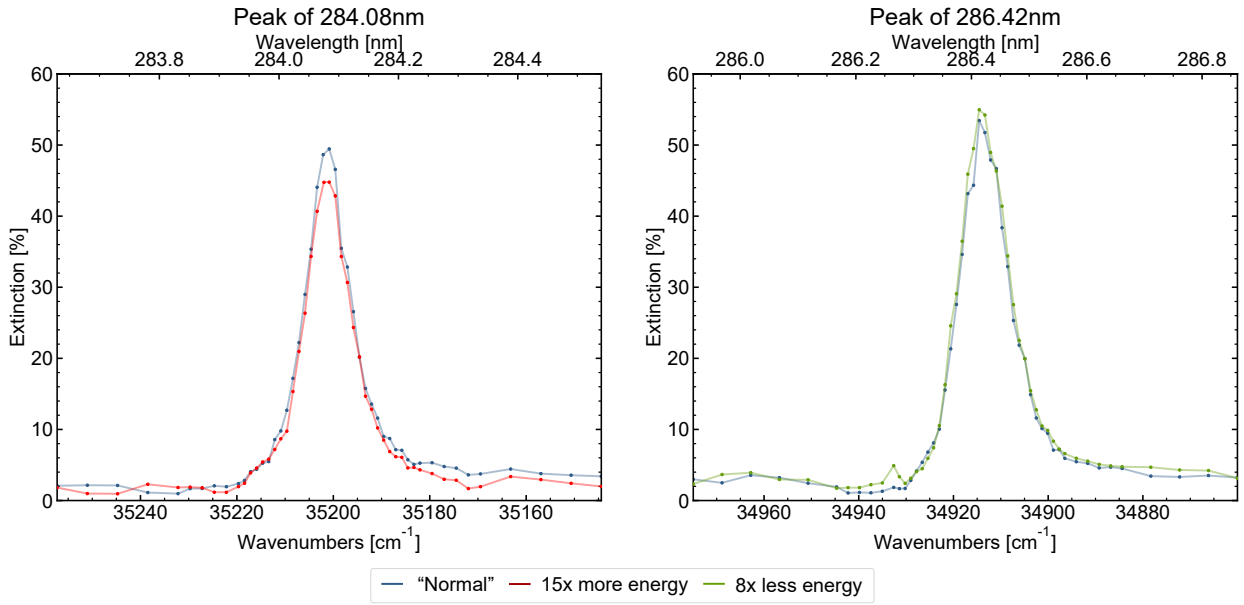

Figure 31: Two atomic resonances, the 284.06 and 286.42 nm resonances, have been measured twice. The *normal* setup is the case used for nearly all measurements in this thesis; no additional filter after the vessel and around 10000 counts on the camera. The 284.08 nm peak was measured again with additional filters after the chamber. The 286.42 nm resonance was measured with only 1200 counts on the camera.